STRENGTH AND DURABILITY OF NEAR-SURFACE MOUNTED CFRP BARS FOR SHEAR STRENGTHENING REINFORCED CONCRETE BRIDGE GIRDERS

Final Report

SPR 712

Oregon Department of Transportation

STRENGTH AND DURABILITY OF NEAR-SURFACE MOUNTED CFRP BARS FOR SHEAR STRENGTHENING REINFORCED CONCRETE BRIDGE GIRDERS

Final Report

SPR 712

by

Jake H. Goebel
Brandon A. Johnson
and
Christopher Higgins, Ph.D., P.E.

for

Oregon Department of Transportation
Research Section
200 Hawthorne Ave. SE, Suite B-240
Salem OR 97301-5192

and

Federal Highway Administration
400 Seventh Street, SW
Washington, DC 20590-0003

March 2012

Technical Report Documentation Page

1. Report No.	2. Government Accession No.	3. Recipient's Catalog No.
FHWA-OR-RD-12-12		

4. Title and Subtitle	5. Report Date
Strength And Durability Of Near-Surface Mounted CFRP Bars For Shear Strengthening Reinforced Concrete Bridge Girders	March2012
	6. Performing Organization Code

7. Author(s)	8. Performing Organization Report No.
Jake H. Goebel, Brandon A. Johnson, and Christopher Higgins, Ph.D., P.E. Oregon State University School of Civil and Construction Engineering 101 Kearney Hall Corvallis, OR 97331	SPR 712

9. Performing Organization Name and Address	10. Work Unit No. (TRAIS)
Oregon Department of Transportation Research Section 200 Hawthorne Ave. SE, Suite B-240 Salem, OR 97301-5192	11. Contract or Grant No.

12. Sponsoring Agency Name and Address		13. Type of Report and Period Covered
Oregon Department of Transportation Research Section 200 Hawthorne Ave. SE, Suite B-240 Salem, OR 97301-5192	and Federal Highway Administration 400 Seventh Street, SW Washington, DC 20590-0003	Final Report
		14. Sponsoring Agency Code

15. Supplementary Notes

16. Abstract

During the interstate expansion of the 1950s, many conventionally reinforced concrete deck girder bridges were built throughout the country. These aging bridges commonly exhibit diagonal cracking and rate inadequately for shear, thus they are candidates for shear strengthening to extend their useful life. Carbon fiber reinforced polymers (CFRP) are emerging as effective materials for strengthening and rehabilitating such bridges. Near surface mounting (NSM) is a newer technique for application of CFRP for retrofitting bridge members that provides advantages over other strengthening techniques. The technique is still new and uncertainties remain regarding strength, long-term durability, and design including the influence of member proportions, flexural reinforcing steel, and CFRP spacing. Bridge girders retrofitted with NSM-CFRP may be exposed to millions of load cycles and environmental conditions and the influence of these exposures on performance are not established. To address these issues, laboratory tests were performed on ten full-size reinforced concrete girders, representative of in-situ bridge members, to determine the performance of NSM-CFRP retrofitting for shear strengthening. One of the specimens was exposed to fatigue loading, two were subjected to environmental exposures, and one was subjected to combined environmental exposure and fatigue loading. Results indicated that NSM-CFRP retrofitting provided significant shear capacity increases, and the high-cycle fatigue and environmental exposures considered did not adversely affect the strength or behavior of the girders. Environmental exposures of some of the adhesives considered did show somewhat reduced performance; therefore, careful selection of materials is important to ensure performance over the expected lifetime. Recommendations for shear strength design with NSM-CFRP are made.

17. Key Words	18. Distribution Statement
CARBON FIBER REINFORCED, NEAR SURFACE MOUNT, REINFORCED CONCRETE, GIRDERS, BEAMS, SHEAR STRENGTH, FATIGUE, FREEZE-THAW	Copies available from NTIS, and online at http://www.oregon.gov/ODOT/TD/TP_RES/

19. Security Classification (of this report)	20. Security Classification (of this page)	21. No. of Pages	22. Price
Unclassified	Unclassified	123	

SI* (MODERN METRIC) CONVERSION FACTORS

APPROXIMATE CONVERSIONS TO SI UNITS

Symbol	When You Know	Multiply By	To Find	Symbol
		LENGTH		
in	inches	25.4	millimeters	mm
ft	feet	0.305	meters	m
yd	yards	0.914	meters	m
mi	miles	1.61	kilometers	km
		AREA		
in^2	square inches	645.2	millimeters squared	mm^2
ft^2	square feet	0.093	meters squared	m^2
yd^2	square yards	0.836	meters squared	m^2
ac	acres	0.405	hectares	ha
mi^2	square miles	2.59	kilometers squared	km^2
		VOLUME		
fl oz	fluid ounces	29.57	milliliters	ml
gal	gallons	3.785	liters	L
ft^3	cubic feet	0.028	meters cubed	m^3
yd^3	cubic yards	0.765	meters cubed	m^3
NOTE: Volumes greater than 1000 L shall be shown in m^3.				
		MASS		
oz	ounces	28.35	grams	g
lb	pounds	0.454	kilograms	kg
T	short tons (2000 lb)	0.907	megagrams	Mg
		TEMPERATURE (exact)		
°F	Fahrenheit	(F-32)/1.8	Celsius	°C

APPROXIMATE CONVERSIONS FROM SI UNITS

Symbol	When You Know	Multiply By	To Find	Symbol
		LENGTH		
mm	millimeters	0.039	inches	in
m	meters	3.28	feet	ft
m	meters	1.09	yards	yd
km	kilometers	0.621	miles	mi
		AREA		
mm^2	millimeters squared	0.0016	square inches	in^2
m^2	meters squared	10.764	square feet	ft^2
m^2	meters squared	1.196	square yards	yd^2
ha	hectares	2.47	acres	ac
km^2	kilometers squared	0.386	square miles	mi^2
		VOLUME		
ml	milliliters	0.034	fluid ounces	fl oz
L	liters	0.264	gallons	gal
m^3	meters cubed	35.315	cubic feet	ft^3
m^3	meters cubed	1.308	cubic yards	yd^3
		MASS		
g	grams	0.035	ounces	oz
kg	kilograms	2.205	pounds	lb
Mg	megagrams	1.102	short tons (2000 lb)	T
		TEMPERATURE (exact)		
°C	Celsius	1.8C+32	Fahrenheit	°F

*SI is the symbol for the International System of Measurement

ACKNOWLEDGEMENTS

The authors would like to acknowledge the interest and contributions of the Technical Advisory Committee whose members included Messrs. Matthew Stucker, Jon Rooper, and Craig Shike from ODOT and Mr. Timothy Rogers from FHWA. We would also like to thank Mr. Steven Soltesz, ODOT, for his support and coordination of this research.

DISCLAIMER

TABLE OF CONTENTS

LIST OF TABLES

LIST OF FIGURES

1.0 INTRODUCTION

Many reinforced concrete deck girder (RCDG) bridges were constructed in the 1950's and 1960's during expansion of the highway infrastructure in the United States. The specifications used in design are now considered deficient as they overestimated the concrete contribution to shear strength and thus prescribed relatively light shear reinforcement. Since these bridges were built, the magnitude and frequency of traffic loading has increased and many are reaching the end of their intended design life. Recently, the Oregon Department of Transportation (ODOT) inspected approximately 1,800 of these vintage RCDG bridges and identified over 500 with varying levels of diagonal cracking (*Williams and Higgins 2008*). Replacement of all existing vintage RCDG bridges exeeds the available resources. Rehabilitation is an economical alternative that can extend the useful life of these bridges.

Carbon fiber reinforced polymers (CFRP) have emerged as a new material for retrofitting existing structures. CFRP can be advantageous as it exhibits high strength-to-weight ratio as well as corrosion resistance. Previous work has identified the near-surface mounted (NSM) technique to be an effective method for installation of CFRP in retrofitting applications. While some research has been performed on NSM-CFRP, the current state of knowledge on strength, environmental durability, and fatigue effects as well as the efficacy of NSM-CFRP retrofitting on full-scale bridge girder performance is lacking. In order to use NSM-CFRP in a long-term bridge management strategy, the long-term durability (both environmental and high-cycle fatigue) needs to be established. In addition, design guidance is needed.

2.0 BACKGROUND

Recent structural rehabilitation techniques for reinforced concrete bridges involve applying carbon fiber reinforced polymers as externally bonded reinforcement (EBR). This technique typically involves cutting CFRP sheets or woven fabric and bonding them to the surface of the structural members in a wet layup construction method. While research has found this method provides strength increases, the reinforcing material is exposed at the surface and is therefore subject to environmental deterioration and possible vandalism. Research has identified debonding as a primary failure mode in the EBR technique before the CFRP is ruptured. This debonding predominately constitutes peeling of the CFRP away from the concrete substrate at failure.

An emerging technique uses CFRP as a near-surface mounted reinforcement. This technique involves inserting epoxy and CFRP strips into saw-cut grooves on the surface of the beam. The original idea of embedding reinforcing bars into the concrete surface was implemented on a bridge in Sweden that was retrofitted with steel rods (*De Lorenzis et al. 2001*). The NSM later evolved to use CFRP and technique alleviates some problems that were experienced using the EBR approach. The CFRP strips of the NSM technique are not directly exposed to the environment, and therefore it is anticipated that environmental conditions will have less impact on durability. Also, because the NSM-CFRP strips are bonded on two sides (within the groove), failure by debonding should be less likely. Finally, the NSM technique does not require as much surface preparation or adhesive to install compared with the EBR technique.

A review of the literature on the efficacy and long-term durability of NSM-CFRP as well as the available design guides was performed. From this review, deficiencies in the current state of knowledge were identified. These are described in the subsequent section.

To aid the reader in understanding the terminologies used by the authors' in this report, the definitions for many of the descriptors of NSM-CFRP reinforcing are contained in Appendix A.

3.0 LITERATURE REVIEW

As the technique is fairly new, few studies have been performed using CFRP as NSM reinforcement on full-scale specimens, particularly when considering shear strengthening, which was the focus of the present research. The following is a review of the current state of the archival literature.

3.1 SHEAR STRENGTHENING

Several research programs have been conducted to investigate the strength of NSM-CFRP for shear. De Lorenzis et al. (*2001*) performed the first experiments using CFRP bars as NSM reinforcement in shear. A total of eight specimens were tested. Specimens were 3 m (10 ft.) long, 406 mm (16 in.) tall, had a flange width of 381 mm (15 in.), a flange thickness of 102 mm (4 in.), and a web thickness of 152 mm (6 in.). Flexural reinforcement of all specimens consisted of two #29 (#9) bars. De Lorenzis *et al.* used deformed #10 (#3) CFRP rods inserted into square 19 mm (0.75 in.) grooves and bonded with epoxy. The epoxy used was Master Builder's Concresive paste having a tensile strength of 13.8 MPa (2000 psi). Beams were tested under four-point bending. The shear span was 1007 mm (42 in.). The first six specimens tested had no internal steel stirrups. Of the six beams, one was a control specimen and five were reinforced in shear with the NSM-CFRP rods. Variables of the five retrofitted specimens included CFRP rod spacing of 127 mm (5 in.) and 178 mm (7 in.), inclination angles of 45˚ and 90˚, and anchorage of rods. It was found that the specimens retrofitted with NSM-CFRP experienced large increases in shear capacity compared with the control specimen. The specimen with CFRP rods at 45˚ exhibited the largest strength increase. Two additional specimens contained internal #10 (#3) steel stirrups spaced at 356 mm (14 in.). Of these two additional specimens, one was left unstrengthened and used as a control while the other was reinforced with NSM-CFRP at 178 mm (7 in.) on center. While the specimen containing internal steel stirrup and CFRP retrofitting showed an increase in shear strength over its control specimen; the increase was not as large when compared to the specimens with no internal steel stirrups.

Nanni et al. (*2004*) performed tests on full-scale prestressed concrete bridge girders strengthened with CFRP. Two damaged in-situ double-T girders were taken from a bridge in Kansas and cut longitudinally to produce four T beam specimens. Specimens were 12.2 m (40 ft.) long and 584 mm (23 in.) deep. The flange was 125 mm (5 in.) thick and 914 mm (36 in.) wide. The web had a thickness of 115 mm (4.5 in.). One specimen was left unstrengthened and used as a control specimen. Two specimens were strengthened with EBR-CFRP in flexure, while the remaining specimen was strengthened in flexure with EBR-CFRP and in shear with NSM-CFRP strips. The NSM-CFRP in this experiment was Hughes Brothers Aslan 500 tape with dimensions of 2 mm (0.08 in.) by 16 mm (0.63 in.). When used in shear strengthening, the strips were installed into 6 mm (0.24 in.) by 19 mm (0.75 in.) grooves at a 60˚ inclination angle every 203 mm (8 in.) on center. The specimen strengthened in both shear and flexure failed in flexure. As a result, a

shear capacity could not be obtained. However, it was concluded that this specimen had a substantially larger ultimate capacity than the specimens strengthened only in flexure.

Barros and Dias conducted several experiments on NSM-CFRP retrofitting beginning in 2006. Barros et al. (*2006*) tested rectangular specimens with cross-sections of 1500 mm x 3000 mm (5.91 in. x 11.8 in.) and 1500 mm x1500 mm (5.91 in. x 5.91 in.) and span lengths of 1500 mm (59.0 in.) and 900 mm (35.4 in.) respectively. Both the EBR and NSM retrofitting techniques were investigated. Four types of specimens were tested: no shear reinforcing, internal steel stirrups of 6 mm (0.236 in.) diameter, U-shaped EBR-CFRP sheets, and NSM-CFRP strips at 45° and 90° angles relative to the beam axis. The CFRP used for all of the testing done by Dias and Barros was S&P laminate CFK 150/2000 strips. These strips had a width of 10 mm (0.394 in.) and a thickness of 1.4 mm (0.551 in.). Groove dimensions for the strips were 5 mm x 12 mm (0.20 in. x 0.47 in.). It was found that the NSM retrofitting technique yielded the greatest increase in shear capacity with laminates applied at 45° being the most effective. While the relationship between the quantity of flexural reinforcing steel and shear strength was not specifically investigated, it was noted that increasing the flexural steel reinforcing ratio resulted in an increase in the shear strength of the specimen.

Dias et al. (*2007*) performed experiments on low strength concrete T beams reinforced in shear with NSM-CFRP strips. Specimens had an overall depth of 356 mm (14.0 in.), a flange width of 450 mm (17.7 in.), flange thickness of 100 mm (3.94 in.), a web width of 180 mm (7.09 in.), and a total span of 2450 mm (96.5 in.). The specimens had 28-day and test-day concrete compressive strengths of 15.9 MPa (2.31 ksi) and 18.6 MPa (2.70 ksi) respectively. Control specimens without CFRP reinforcement were tested and compared with specimens that had various quantities of CFRP strips at 90°, 60°, and 45°. Specimens had an internal steel stirrup spacing of either 300 mm (11.8 in.) or 180 mm (7.09 in.). It was determined that the effectiveness of the NSM reinforcing was negatively affected by the presence of internal steel stirrups based on the percentage of strength capacity increase of the specimens. By reducing the internal stirrup spacing from 300 mm (11.8 in.) to 180 mm (7.09 in.), the average shear strength increase changed from 27.4% to 16.2%. It was determined that increasing the amount of internal steel stirrups proportionally reduces the contribution of the CFRP strips to the specimen's shear strength. It was also noted that reducing the concrete strength resulted in an increase in the likeliness of epoxy around the CFRP strips detaching. Consequently, as the concrete strength decreased, added shear strength from the NSM reinforcing did as well.

Testing on T beams reinforced with NSM-CFRP in shear continued with Dias et al. (*2008*). The dimensions, CFRP, and groove size of the specimens matched those reported in Dias et al. (*2007*). Specimens included 1) no internal shear reinforcing, 2) 6 mm (0.236 in.) diameter internal steel stirrups spaced at 130 mm (5.12 in.) and 3) 6 mm (0.236 in.) diameter internal steel stirrups spaced at 300 mm (11.8 in.) on center. Similarly to Dias et al. (*2007*), inclination angles of 90°, 60°, and 45° were investigated. For each inclination angle, three quantities of NSM-CFRP were applied. Specimens were subjected to service loads based on a deflection of L/400 and maximum loads. From the results of the experiment, it was determined that the CFRP strips with an inclination angle of 60° were the most effective with the strips at 45° being more effective than those at 90°. Specimens without internal steel stirrups that were retrofitted and those with steel stirrups spaced at 130 mm (5.12 in.) that were retrofitted were able to reach

nearly the same maximum load. It was also noted that after diagonal cracks had formed, the NSM-CFRP reinforcing contributed significantly to the stiffness of the specimen.

Rizzo et al. (*2009a*) investigated the effects of epoxy type, CFRP spacing, CFRP inclination angle, and CFRP type (round versus rectangular) on conventionally reinforced concrete specimens reinforced in shear with NSM-CFRP. The nine rectangular specimens were 2 m (6.6 ft.) long with a 200 mm (7.9 in.) by 210 mm (8.3 in.) cross-section. The specimens were simply supported and were tested under four-point loading. The shear span was 519 mm (20.4 in.). Half of the specimens were retrofitted with NSM-CFRP while the other half of the specimens were over-reinforced in shear with 10 mm (0.4 in.) steel stirrups spaced at 50 mm (2 in.) on center to insure a shear failure in the half of the specimen with the CFRP reinforcing. The retrofitted side of the specimens had 6 mm (0.24 in.) steel stirrups spaced at 160 mm (6.3 in.) on center. The nine specimens consisted of one control specimen, one specimen retrofitted with externally bonded CFRP, and seven retrofitted with NSM-CFRP. Results of the experiment indicated that all specimens strengthened with NSM-CFRP failed through separation of the concrete cover containing the CFRP retrofitting from the core of the specimen containing the steel reinforcing. It was found that the NSM-CFRP reinforced specimens provided more shear strength than the specimens strengthened with EBR-CFRP. Of the two epoxies investigated in this study, the epoxy that had a lower tensile strength and elastic modulus provided significantly higher strength gains. This was attributed to the stiffer epoxy accelerating the formation of cracks in the concrete. Higher increases in strength were also obtained with tighter CFRP spacing from 73 mm (2.9 in.) to 45 mm (1.8 in.) and an inclination angle of 45˚ from 90˚. Five specimens were strengthened with round 8 mm (0.3 in.) diameter rods set in square 12 mm (0.47 in.) saw-cut grooves while two specimens had 2 mm x 16 mm (0.08 in. x 0.63 in.) CFRP laminate strips. The surface of the CFRP strips were roughened and then inserted into 5 x 18 mm (0.2 x 0.7 in.) saw cut grooves filled with epoxy. It was found that the specimens retrofitted with CFRP strips exhibited a slightly lower strength increase than those retrofitted with the CFRP bars due to an increased stiffness in the CFRP strips

The effects of NSM-CFRP retrofitting on full size reinforced concrete specimens were investigated by Howell (*2009*). Specimens were initially loaded to produce diagonal cracking in the specimens to make them representative of in-situ conditions before being strengthened and tested to failure. The CFRP and epoxy used in the experiment were Hughes Brother's Aslan 500 and 3M DP460NS respectively. The inverted-T beam specimen had an overall height of 1219 mm (48 in.), a flange width of 914 mm (36 in.), a web width of 356 mm (14 in.), and a flange thickness of 152 mm (6 in.). The total length of the specimen was 7925 mm (312 in.) and it had a shear span of 2997 mm (115 in.). Internal #13 (#4) steel stirrups had a spacing of 457 mm (18 in.). Three NSM-CFRP strips were placed within the shear span on each side of the specimen at a spacing of 749 mm (29.5 in.). Groove dimensions were 6.4 mm x 19 mm (0.25 in. x 0.75 in.). Because of the large spacing between CFRP strips, virtually no increase in shear strength was observed. No definitive conclusions or design recommendations could be ascertained from this single test.

Islam (*2009*) performed tests on four specimens: one control and three retrofitted with NSM-CFRP oriented vertically. One of the retrofitted specimens did not have internal shear reinforcement. CFRP spacing was 152 mm (6 in.) for the specimen without internal shear

reinforcing and varied from 305 mm (12 in.) to 152 mm (6 in.) for internal stirrup spacing of 305 mm (12 in.) and 610 mm (24 in.), respectively. The specimens of rectangular cross-section had a height of 305 mm (12 in.), a width of 254 mm (10 in.), and an overall length of 2134 mm (84 in.). Specimens were tested in four-point bending with a shear span of 610 mm (24 in.). It was found that NSM-CFRP retrofitting resulted in more than a 20% increases in specimen capacity with no delaminating, debonding, or fracturing of the CFRP material. This experiment was not found until after a majority of the work in this research was completed and as a result was not used in predicting CFRP contributions.

Continuing previous research, Dias et al. (*2010*) tested T beams strengthened with NSM-CFRP in shear. The dimensions of the specimen and CFRP type used were the same as those in Dias et al. (*2007*). Similarly to previous work, testing variables included NSM-CFRP quantity and inclination angle (90°, 60°, and 45°). In addition to NSM reinforcing, this test included specimens strengthened in shear with EBR-CFRP. It was found that specimens strengthened using the NSM technique provided larger strength gains than those strengthened with the EBR technique.

3.2 ANALYTICAL MODELS

Much work has been performed to determine NSM-CFRP contributions in shear strengthening. De Lorenzis et al. (*2001*) were the first to begin developing analytical models. Two controlling failure modes were identified as debonding of the NSM-FRP and tensile failure in the concrete. Concrete tensile failure was accounted for by limiting the maximum strain in the FRP to 0.004. Equations were developed to calculate the NSM-FRP shear strength for each of these failure modes with an assumed shear crack angle of 45°, and the minimum value was used.

Nanni et al. (*2004*) further developed the design methods created by De Lorenzis et al. (*2001*). The same two failure modes were recognized. However instead of using the minimum of two shear contributions, tensile failures in the concrete were taken into account by limiting the bond length of each FRP bar. This method was recommended by the manufacturer of the CFRP used in the present research and will be discussed in more depth subsequently.

Rizzo et al. (*2009b*) also expanded on the work done by De Lorenzis et al. (*2001*). A generalized model was developed to allow for a variable crack angle. The crack location relative to the CFRP reinforcing was also considered. Instead of limiting the FRP strain to account for a maximum FRP contribution, a reduced bond stress was found through a calculated maximum embedment length. A second model accounting for local bond-slip behavior was also developed. This model allowed the peak shear forces of the internal steel stirrups and the FRP retrofitting to be reached at different times.

Bianco et al. (*2009*) focused on the debonding of NSM-CFRP through a semiconical failure in the concrete substrate. These semi-cones of concrete act perpendicular to the critical diagonal crack (CDC). Therefore, it was easiest to model the behavior of the NSM-CFRP when the bars were installed perpendicular to the CDC and when there was no interaction between CFRP bars. The authors indicated that for general cases in which there was interaction between CFRP bars and the bars were oriented vertically, the semiconical fracture surface became increasingly difficult to model and the tensile fracture capacity of the concrete was more complex to

determine. Equations were developed for the bond stresses of finite and infinite bond lengths. Four bond phases were identified, each with its own analytical procedure: elastic, softening, softening friction, and slipping.

Barros et al. (*2009*) built on the work performed by Bianco et al. (*2009*) and developed an analytical model that incorporated three failure modes: debonding, tensile rupture of the FRP strip, and concrete tensile fracture. The concrete tensile fracture was modeled using overlapping semiconical sections of concrete. The size of the semi-cone was dependent on the amount of shear stress experienced by the CFRP bar and could penetrate through more than half of the beam width. It did not appear that the authors included the effects of internal shear reinforcement on the behavior of the semi-cones.

3.3 BOND OF NSM-CFRP

In order to fully assess NSM-CFRP strength, bond performance must be well characterized. Bond is responsible for the transfer of stress from the concrete substrate into the CFRP reinforcement. Furthermore, failure in the bond at the CFRP/epoxy and epoxy/concrete interfaces is a primary failure mode for NSM-CFRP.

De Lorenzis et al. (*2002*) investigated the bond between NSM-CFRP rods and concrete substrate. Pull-out tests were performed on T beams with a length of 1200 mm (48 in.), an overall height of 254 mm (10 in.), a flange width of 254 mm (10 in.), a flange thickness of 102 mm (4 in.), and a web thickness of 152 mm (6 in.). The tension face of the specimens was retrofitted with NSM-CFRP rods. Specimens were simply supported with a load applied at midspan. The concrete compressive strength was reported as 27.6 MPa (4000 psi). Variables included bond lengths of 6, 12, 18, and 24 bar diameters. Results showed that the ultimate strength increased with an increased bond length. In addition to bond length, surface conditions of the CFRP rods were investigated. Sandblasted CFRP rods were compared with deformed CFRP rods. It was found that the deformed CFRP rods provided greater bond strength. Finally, the importance of groove width was investigated. Groove widths of 16 mm (0.625 in.), 19 mm (0.75 in.), and 25.4 mm (1 in.) were tested. Results indicated a correlation between larger groove widths and higher strength increases.

Hassan et al. (*2003*) performed tests to evaluate the bond strength of NSM-CFRP strips in a similar manner to De Lorenzis et al. (*2002*). Nine T beam specimens with a length of 2500 mm (98.4 in.), a total height of 300 mm (11.8 in.), and a web thickness of 150 mm (5.9 in.) were tested. Specimens were simply supported and a load was applied at midspan until failure. A single NSM-CFRP strip was installed on the tension face of the specimens. The CFRP strips used were S&P CFK 150/2000 with dimensions of 1.2 mm (0.05 in.) by 25 mm (1 in.). The groove size was 5 mm (0.2 in.) by 25 mm (1 in.). Eight embedment lengths were tested ranging from 150 mm (5.9 in.) to 1200 mm (47 in.). Results indicated that the long embedment lengths of 850 mm (33.5 in.) to 1200 mm (47 in.) failed by rupturing of the CFRP strips. The specimens with the six shorter embedment lengths failed through debonding.

Shield et al. (*2005*) investigated the effects of adhesive type on the bond strength of NSM-CFRP retrofitting through pull-out testing. Seven adhesive types were tested on small-scale specimens with dimensions of 152 mm (6 in.) by 152 mm (6 in.) by 203 mm (8 in.). The CFRP chosen for

the experiment was Hughes Brothers Aslan 500 tape with a cross sectional area of 32 mm^2 (0.05 in^2). The groove size for all specimens was 6.4 by 19 mm (.25 x .75 in.). It was noted that for all adhesives tested, no correlation was found between the manufacturers' provided properties and experimental results. The highest ultimate strength was achieved using the 3M DP460NS adhesive. Based on the results of the small scale testing, larger scale tests were performed using two of the adhesives. 3M DP460NS was chosen due to its superior bond strength while Sika Anchorfix-3 was chosen as it was the most commonly used adhesive that was tested. The larger specimens consisted of two 610 mm (24 in.) by 305 mm (12 in.) by 305 mm (12 in.) blocks connected with four NSM-CFRP strips (one on each face). The two blocks were then pulled apart until failure. It was found that the 3M DP460NS adhesive again provided superior bond strength. It was also noted that this adhesive appeared to be more ductile. These results supported the notion that stiffer adhesives cause early failure through excessive cracking in the concrete. The effect of vibration during the curing of epoxy was also investigated. This was done by applying a cyclical load to the specimens during the curing of the epoxy. Results showed no significant loss in strength due to the vibration loading.

Additional research into the bond strength of NSM-CFRP strips was performed by Bianco et al. (*2009*). A model was created that described and predicted bond failure. Findings indicated that changes in the elastic modulus of the CFRP reinforcement and concrete generated only marginal changes in the ultimate load of the bond. More significant changes resulted from changes in the CFRP cross section and the depth of the CFRP in the specimen as more depth provided additional confinement.

3.4 ENVIRONMENTAL EFFECTS

No literature was found regarding the effects of freeze-thaw exposure on beams retrofitted with NSM-CFRP in shear. The studies discussed below investigated environmental effects on externally bonded CFRP.

Soudki et al. (*1997*) performed tests on CFRP confined concrete cylinders. The 150 mm x 300 mm (6 in. x 12 in.) cylinders were wrapped with one or two layers of 0.16 mm (0.0063 in.) thick CFRP sheets. Nine cylinders were subjected to 50 freeze-thaw cycles while four were left at room temperature for control specimens. It was reported that the specimens subjected to freeze-thaw cycles were kept in a cold room at a temperature of -18° C (0°F) for 16 hours, then thawed in a water bath at 18° C (64°F) for 8 hours. After instrumenting the cylinders to measure axial and radial strain, the specimens were loaded axially to failure. It was noted that using one layer of the CFRP wrap increased the axial strength of the specimens by 57% while two layers increased the axial strength by 87%. It was determined that there was around a 16% loss in axial strength for specimens with one layer of CFRP wrap when subjected to freeze-thaw conditions compared with the same specimens kept at room temperature.

Karbhari et al. (*2002*) also tested concrete cylinders confined with externally bonded CFRP sheets. Specimens were 154.2 mm x 304.8 mm (6 in. x 12 in.) and were subjected to 0, 150, 300, and 450 cycles of freeze-thaw to determine environmental durability. To install the CFRP sheets, the concrete face was first lightly sandblasted to expose the aggregate. The specimens were then cleaned and dried before a primer was applied. Three layers of CFRP fabric were

applied using a wet layup technique with fibers oriented transversely around the cylinders. Specimens were then either subjected to dry freezing, saturated freezing, or saturated freeze-thaw. Saturated specimens were submerged in deionized water at 23°C (73°F) for 25 days to ensure saturation. Dry and saturated specimens were then frozen at 0°C (-18°F) for 150, 300, or 450 days. Specimens subjected to freeze-thaw were subjected to extreme temperatures ranging from -18°C (0°F) to 20°C (68°F) with each complete cycle lasting 24 hours. Resin and FRP composite coupon strengths were tested at each increment. When compared with unexposed specimens, the strength of the resin exposed to dry freeze after 450 days increased by 8.8% while the resin exposed to saturated freeze and freeze-thaw decreased by 14% and 22% respectively. The CFRP composite strength for dry freeze, saturated freeze, and freeze-thaw decreased by 22%, 38%, and 43% respectively, showing that the effects of freeze-thaw were detrimental to the durability of the retrofitting components.

The CFRP confined specimens exhibited deterioration as well. After 450 cycles of freeze-thaw, the compressive strength of these specimens was shown to be 20% less than the unexposed confined specimens. This was more significant than specimens that were only subjected to freezing: 9.7% and 14% for dry freeze and saturated freeze respectively. It was noted that the specimens exposed to freeze-thaw conditions exhibited significant circumferential cracking which indicated fiber debonding and local delamination. These signs were not present in the dry or saturated freeze specimens. This was in part attributed to the increased moisture gains that take place during freeze-thaw conditions.

Malvar et al. (*2003*) investigated the effects of temperature and moisture on epoxy adhesion. Pull-off tests were performed at two climate conditions. Climate conditions consisted of an ambient condition of 23°C (76°F) with a relative humidity of 50% and a tropical condition of 35°C (95°F) with a relative humidity of 95%. The tests consisted of bonding small aluminum dollies to concrete blocks, exposing them to an environmental condition, and pulling the dollies in direct tension until detachment. Results indicated that specimens tested under higher temperatures and humidity produced significant decreases in bond strength.

Green et al. (*2003*) tested the effects of freeze-thaw on reinforced concrete beams retrofitted with CFRP in flexure. Rectangular specimens with dimensions of 152 mm x 102 mm x 1220 mm (6 in. x 4 in. x 48 in.) were subjected to 0, 50, and 200 cycles of freeze-thaw. It was noted that the concrete mixture design included 6% air entrainment. Specimens were over designed in shear using steel reinforcement and CFRP wraps to ensure a flexural failure. FRP retrofitting was installed on the tension face of the specimens. The beam soffits were sandblasted and a primer was applied before installing the CFRP. Some specimens were then exposed to cycles of freeze-thaw with freezing occurring at -18°C (0°F) for 16 hours and thawing in water at 15°C (59°F) for 8 hours. Each cycle lasted 24 hours. Control specimens were stored at an ambient room temperature.

After environmental conditioning, the specimens were tested to failure in four-point bending. All specimens began to experience cracking around the same load. From testing, it was concluded that the CFRP retrofitting was not affected by freeze-thaw conditions. It was noted that specimens failed by peeling of the CFRP sheets away from the concrete substrate before concrete crushing occurred in the compression zone. The importance of detailing in an effort to

prevent peeling failures was emphasized. Peeling failures were considered to be a premature failure mode as additional strength would have been gained if the CFRP material were to rupture instead of peel from the substrate. With adequate detailing, it was concluded that there were no adverse effects from 200 cycles of freeze-thaw on reinforced concrete beams externally retrofitted with CFRP sheets.

Grace (*2004*) conducted tests of concrete beams strengthened for flexure with externally bonded CFRP sheets and plates subjected to freeze-thaw cycles. The experiment consisted of 2500 mm (98.4 in.) long rectangular concrete beams with a width of 152 mm (6 in.) and a height of 254 mm (10 in.). The specimens were exposed to either 350 or 700 freeze-thaw cycles in an environmental chamber. Air temperatures used to freeze the specimens were -17°C (1°F) while thawing occurred in water at 4°C (39°F). Each freeze-thaw cycle took four hours. Specimens were then loaded under four-point bending to failure. It was found that strength was reduced by 3.3% and 9.5% for 305 and 700 cycles of freeze-thaw respectively. Strength reduction factors, Ψ, were then developed for freeze-thaw conditions. The Ψ for CFRP plate and fabric were reported as 0.90 and 0.85 respectively. These reduction factors were formulated based on the percentage of decreased strength of the specimens subjected to freeze-thaw conditions relative to their respective control specimens.

Myers et al. (*2005*) investigated the effects of environmental exposure including surface moisture, relative humidity, and temperature on the bond strength of EBR-CFRP sheets to concrete. The specimens tested were 152 mm x 152 mm x 610 mm (6 in. x 6 in. x 24 in.). The U-wrap CFRP fabric sheets had dimensions of 584 mm x 140 mm (23 in. x 5.5 in.) and covered 88% of the concrete surface. After the specimens were pre-cracked at 28 days to induce a flexural crack at mid-span, CFRP was installed at -12°C (10°F), -17°C (20°F), and -1°C (30°F). Pull-off tests were performed by attaching small adhesive fixtures to the CFRP. The adhesive fixture was attached to the testing apparatus and direct tension was applied perpendicular to the concrete face at 0.67 kN/sec (150 lb/sec). Three possible failure modes were identified: concrete failure in tension, failure in the epoxy, and delamination of the CFRP sheets from the specimen. Control specimens experienced a tension failure in the concrete while the specimen with CFRP installed at -12°C (10°F) exhibited a failure through debonding of the CFRP sheets from the concrete substrate. This showed that while full bonding was achieved in the control specimens, the same was not true of specimen in which CFRP was installed at a low temperature. Test results also showed that the measured CFRP strain in the low temperature installation specimen was 3-5 times higher than the control specimen. As a result, it was concluded that externally bonded CFRP should not be installed in low temperature or frost conditions. A minimum installation temperature of 40°F (4°C) was recommended.

Research on full-scale reinforced concrete girders strengthened with EBR-CFRP has been performed at Oregon State University. Higgins et al. (*2008*) tested reinforced concrete specimens in shear that were exposed to accelerated environmental conditions including freeze-thaw, freeze-thaw combined with high-cycle fatigue, and water immersion. Specimens consisted of T and IT shaped girders. All specimen dimensions matched those of Howell (*2009*). The concrete and steel properties of the experiment were representative of 1950's vintage conventionally reinforced concrete deck-girder bridges. A total of ten specimens were tested: two control specimens, five specimens subjected to freeze-thaw, two subjected to moisture

infiltration, and one subjected to combined freeze-thaw exposure and fatigue loading. No significant strength reduction was found in IT specimens while a 14% reduction in strength for T specimens was observed. Freeze-thaw conditions combined with fatigue loading had little effect on the shear strength of the specimen if water infiltration was minimized. Fatigue loading generated minor debonding that was not significant enough to affect the shear capacity of the specimen.

3.5 FATIGUE STRENGTH

No research was identified on fatigue performance of RC beams strengthened with NSM-CFRP reinforcement in shear. However, data were available regarding the fatigue performance of flexurally strengthened and shear strengthened beams using the EBR technique.

Shahawy et al. (*1999*) tested RC T beams with externally bonded CFRP sheets for flexural strengthening. Both static and fatigue loading conditions were considered. The beams had an overall height of 445 mm (17.5 in.), a flange thickness of 59 mm (2.32 in.), a flange width of 584 mm (23.0 in.), and a tapered web thickness of 150 mm (5.91 in.) at the flange and 91 mm (3.58 in.) at its base. The length of the specimen was 5790 mm (228 in.). Sixteen specimens were tested: ten under static loading conditions and six with fatigue loading. Specimens included partially and fully wrapped, as well as one, two, three, and four layers of CFRP sheets. Fatigue testing was performed using fully wrapped specimens. The fatigue loading was sinusoidal and ranged from 25% to 50% of the capacity of the control specimen. The loading rate was 1 Hz. Unreinforced specimens were tested to 150,000 cycles of loading during which severe cracking occurred. The beams were then reinforced with two or three layers of CFRP sheets and tested to 2,000,000 cycles of loading before failing via rupture of the CFRP fabric. For the specimens with two layers of CFRP sheets, a large change in deflection occurred between 1,200,000 and 1,800,000 cycles. However, the stiffness remained approximately constant and the fatigue life was approximately 1,800,000 cycles. The specimens with three layers of CFRP exhibited fatigue failure at 3,000,000 cycles. It was noted that the control specimen failed at 295,000 cycles.

Brena et al. (*2005*) conducted flexural fatigue testing of RC beams with externally bonded CFRP sheets. Two configurations of CFRP sheets were used. Rectangular test specimens were 203 mm (8.0 in.) wide and either 356 mm (14.0 in.) or 406 mm (16.0 in.) deep. The lengths of the specimens were either 2.9 m (9.51 ft.) or 3.2 m (10.5 ft.). Test results indicated two primary failure modes: debonding of the CFRP and yielding of the shear reinforcement. Specimens were tested under different fatigue load amplitudes. Some specimens were loaded from 35% to 57% of flexural yield. These specimens did not exhibit additional cracking after 100 cycles of load and did not experience a significant increase in strain as the number of load repetitions increased. Other specimens exposed to extreme load amplitudes (90% and 100% of yield load) had cracks that grew in length and width for the first few thousand cycles of loading. Also, strain in the reinforcing bars increased with number of applied load cycles. It was noted that the rates of strain increase were different in the steel, concrete, and composite laminates. CFRP strain increased linearly, steel reinforcement strains increased depending on loading, and concrete compressive strain showed little change. It was noted that ACI Committee 215 suggests limiting the allowable concrete stress to 40% of the compressive strength for fatigue design of non-

prestressed members. ACI Committee 440 recommends a limitation of 55% of the composite's rupture stress from the combined stresses from cyclic and sustained loading. This is so that the composite does not experience a fatigue failure.

Quattlebaum et al. (*2005*) compared three flexural retrofit systems for monotonic and fatigue loading. Specimens were rectangular in cross section with a height of 254 mm (10.0 in.), a width of 152 mm (6.0 in.), and a length of 4750 mm (15.6 ft.). The retrofit systems used were EBR, NSM, and a supplemental anchorage of EBR with powder actuated fasteners. CFRP strips, as well as glass/carbon hybrid strips were used for the powder actuated fastener method. The NSM-CFRP strips were Tyfo 2000. Specimens were fatigue loaded at a frequency of approximately 1.3 Hz. The fatigue specimens were divided into low-stress and high-stress categories. The low-stress specimens experienced a reinforcing steel stress of 180 MPa (26.1 ksi) before the CFRP strips were applied while the high-stress specimens experienced a reinforcing steel stress of 250 MPa (36.3 ksi) before retrofitting. The NSM method performed the best in the low-stress specimens and second best in the high-stress specimens. The powder actuated fastener system performed the best in high-stress testing; however, the authors noted that it had not yet been accepted as a permanent retrofit method due to the shearing of the fasteners shortly after initial failure as well as the additional environmental protection requirements to ensure the durability of the fasteners.

Higgins et al. (*2007*) tested nine reinforced concrete bridge girders with dimensions equal to those of Howell et al. (*2009*) under high cycle fatigue loading. Specimens were exposed to an equivalent stress range equal to 50 years of service life. An equivalent stress range of 98 MPa (13.8 ksi) was determined using field instrumentation. Results indicated an increase in diagonal-crack motions with insignificant changes in stirrup strain ranges during fatigue loading. The ultimate capacities of the specimens tested were not significantly affected by fatigue loading.

Williams et al. (*2008*) performed field and laboratory tests of FRP-repaired RC deck girders to evaluate high-cycle fatigue behavior. An in-service 1950s vintage RC deck-girder bridge repaired with externally bonded carbon fiber laminates for shear strengthening was inspected and instrumented. FRP strain data were collected under ambient traffic conditions. In addition, three full-size girder specimens repaired with bonded carbon fiber laminate for shear strengthening were tested in the laboratory under fatigue loads and compared with two control specimens. Specimen dimensions and material properties matched Howell (*2009*). Results indicated relatively small in-situ FRP strains, while laboratory fatigue loading produced localized debonding along the FRP termination locations at the stem-deck interface. It was determined that the fatigue loading did not significantly alter the ultimate shear capacity of the specimens.

While some research has been done on CFRP material retrofitting systems, little research has been performed using the NSM technique. Most of the research performed on the fatigue life of CFRP material retrofitting has focused on the flexural strengthening of RC members strengthened with the EBR technique. Also, no research has been performed on full-size bridge specimens. Additional research investigating the fatigue effects of NSM-CFRP strips in shear on full-size bridge member is needed.

3.6 DESIGN GUIDES

The current United States design methods for NSM-CFRP retrofitting systems are found in ACI 440.2R-08: Guide for the Design and Construction of Externally Bonded FRP Systems for Strengthening Concrete Structures (*American Concrete Institute 2008a*). The ACI guide for design is based on limit-states design principles and uses the archival research findings described in the above literature review. Minimum groove dimensions, epoxy cover, and development lengths are specified. A recommended NSM-CFRP effective tensile stress between 3.45 MPa (500 psi) 20.7 MPa (3000 psi) is provided based on a wide range of possible stresses found in experiments. ACI 440 provides a method for shear design of EBR-CFRP but does not explicitly prescribe design procedures for NSM-CFRP contribution to shear strength.

ACI 440 recognizes that environmental conditions can adversely affect FRP systems. Possible environmental impacts are listed as alkalinity, salt water, high humidity, high temperature, and freezing-and-thawing cycles. The current approach accounts for environmental degradation by using a reduction factor based on the exposure condition and type of FRP material as shown in Table 3.1. These modification factors are applied to the design ultimate tensile strength and the design rupture strain of the FRP. They are the only means ACI 440 uses to account for environmental exposure. The reduction factors are believed to be conservative estimates based on the relative durability of the fiber type, but no research is referenced for the bases of these factors. They do not consider different adhesives or any bond strength reductions. These reductions do not take into consideration if the FRP system is EBR or NSM.

Table 3.1: ACI 440 environmental reduction factors

Exposure conditions	Fiber type	Environmental reduction factor CE
Interior exposure	Carbon	0.95
	Glass	0.75
	Aramid	0.85
Exterior exposure (bridges, piers, and unenclosed parking garages)	Carbon	0.85

ACI 440 section 9.3.1 also accounts for the response of FRP and concrete to thermal conditions. It states that strains are induced due to the different thermal expansion coefficients of concrete and FRP. It determines that based on research, for small ranges of temperature change, ±50°F (±28°C), the thermal induced strains do not affect bond.

ASTM D 3039 designates the testing procedures for determining the tensile strength of FRP. The test method prescribes that a strip of FRP is mounted in grips and pulled in direct tension until failure is achieved. Provisions on the testing apparatus, samples, calibration, and testing conditions are given. Testing procedures including loading rate, testing environment, data collection, and possible failure modes are specified.

4.0 RESEARCH SIGNIFICANCE

The present state of knowledge regarding shear strengthening using NSM-CFRP is lacking in several areas. To date, the majority of specimens tested have been relatively small in size as illustrated in Figure 4.1 which shows the cross-sections and flexural reinforcing ratios of specimens identified in the literature review for visual comparison of scale. It is not clear whether the behavior of NSM-CFRP retrofitting on small-scale specimens can be applied to larger full-size bridge girder specimens. The present research uses large-size specimens that have similar dimensions and flexural reinforcing ratio as that used by Howell (*2009*). Also, many of the specimens that have been tested do not contain internal steel stirrups. Data from these tests exhibit unrealistic strength gains as specimens with even small amounts of shear reinforcement will produce disproportionately large strength increases for specimens with no shear reinforcement. These specimens are also not representative of in-situ reinforced concrete members in bridges.

Specimens have also been over-reinforced in flexure in an attempt to induce shear failures to the point that they no longer represent in-situ member proportions. As will be described subsequently, flexural reinforcing steel contributes to shear strength and influences shear performance. As a result, these flexurally over-reinforced specimens with NSM-CFRP may not perform in a way that is representative of those in service with conventional detailing and proportions. Tests of specimens with realistic flexural reinforcement are needed to characterize the likely performance of NSM-CFRP for shear strengthening.

To date, there has been no testing of environmental durability or fatigue effects on realistically reinforced NSM-CFRP reinforced beam or girder specimens for shear. As a result, full-scale testing of specimens with common reinforcement details and proportions are needed to quantify shear performance and establish or validate design methods for shear strengthening with NSM-CFRP reinforcement. Environmental and fatigue tests must be conducted on similar full-scale specimens to quantify performance, long-term durability, and identify issues that may affect long-term durability.

The research reported here helps to fill many of the knowledge gaps presently existing for application of NSM-CFRP for shear strengthening bridge girders.

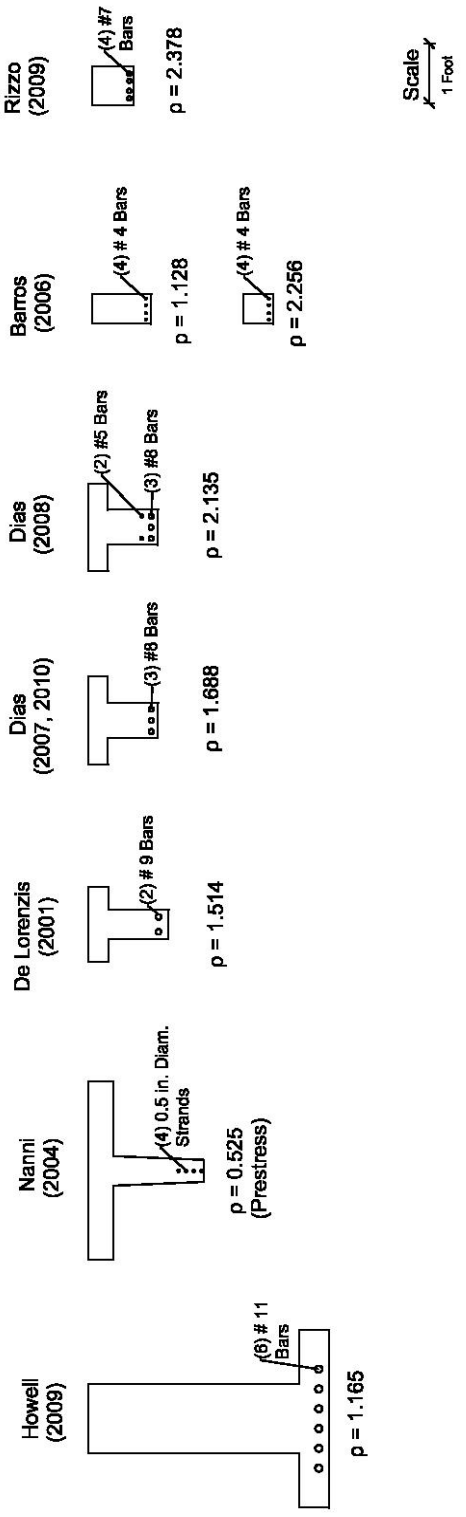

Figure 4.1: Scaled cross-sections and flexural reinforcing ratios for literature specimens

5.0 EXPERIMENTAL PROGRAM

In order to address the gaps identified above, an experimental program was developed. This program consisted of material selection, specimen design, determination and application of precrack loading, NSM-CFRP installation, development and implementation of fatigue and environmental exposure programs, and tests of specimens to failure. The experimental program consisted of full-size girder and individual bond specimens, which will be described in subsequent sections.

5.1 FULL-SIZE GIRDER SPECIMENS

Ten full-size girder specimens were constructed to investigate the performance of NSM-CFRP on the shear strength of conventionally reinforced concrete girders. This research considered the salient variables associated with NSM-CFRP strengthening of RCDG bridges for shear. Two specimens were T-beams, which represented shear in the positive moment region where the deck is in flexural compression. These two specimens had different NSM-CFRP strip spacing and were tested to establish shear strength. The other six specimens were IT-beams, which represented shear in the negative moment region of a continuous bridge where the deck is in flexural tension. Four of the IT specimens were tested to establish shear strength and had various amounts of flexural steel, internal steel stirrups, and CFRP strip spacing. Of the remaining IT specimens, one was used to investigate the effects of long-term moisture exposure, one was used to investigate freeze-thaw exposure, one was used to investigate high-cycle fatigue, and the last one was used to investigate the combined effects of high-cycle fatigue and freeze-thaw exposure. Larger numbers of IT specimens were used because most RCDG bridges are continuous and the negative moment region combine high shear with high moment in situ. Figure 5.1 illustrates the naming convention used to identify the specimens, and Table 5.1 shows the test matrix for the specimens. The design method used to determine the stirrup and CFRP strip spacing is described subsequently.

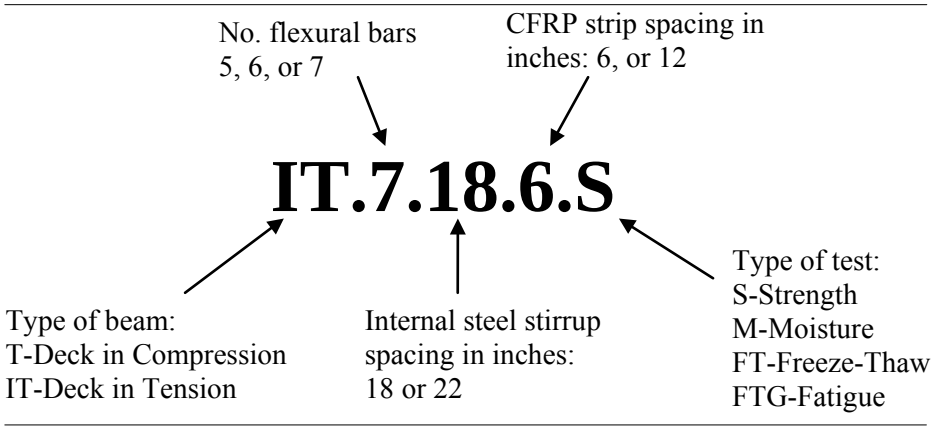

Figure 5.1: Full-scale girder specimen identification

Table 5.1: Full-scale girder test matrix

Specimen	Specimen Type	No. of Flexural Bars	Stirrup Spacing (mm) [in.]	CFRP Spacing (mm) [in.]	Test Type
T.6.18.6.S	T	6	357 [18]	152 [6]	Strength
T.6.18.12.S	T	6	357 [18]	304 [12]	Strength
IT.7.18.6.S	IT	7	357 [18]	152 [6]	Strength
IT.7.18.12.S	IT	7	357 [18]	304 [12]	Strength
IT. 7.22.6.S	IT	7	559 [22]	152 [6]	Strength
IT.5.22.12.S	IT	5	559 [22]	152 [12]	Strength
IT.7.18.6.M	IT	7	357 [18]	152 [6]	Moisture Exposure
IT.7.22.6.FT	IT	7	559 [22]	152 [6]	Freeze-thaw
IT.7.22.6.FTG	IT	7	559 [22]	152 [6]	Fatigue Effects
IT.7.22.6.FT/FTG	IT	7	559 [22]	152 [6]	Freeze-thaw and Fatigue

5.2 DESIGN METHOD

Before constructing the full-scale girder specimens for this investigation, a prediction of the NSM-CFRP strengthened shear capacity was needed. Due to the lack of available full-scale NSM-CFRP test data, the NSM-CFRP contribution to shear strength was uncertain. The approach used in this research was to predict the strengthened shear capacities by finding the base shear capacity of relevant archival test specimens (the strength without NSM-CFRP) and then estimating the additional capacity provided by the NSM-CFRP strips based on the experimentally reported specimen strengths.

The shear strength of the base specimens without NSM-CFRP was calculated using the program Response 2000 (R2k). This computer program was developed at the University of Toronto by Bentz, (*2000*) for analyzing reinforced concrete sections. R2k performs sectional analysis to determine the member strength based on Modified Compression Field Theory (MCFT). Previous research on 44 similarly full-scale reinforced concrete girders tested at Oregon State University demonstrated the efficacy of R2k in predicting the strength of bridge girders of the proportions and materials considered typical of vintage RC deck-girder bridges (*Higgins et al. 2005*). The reported prediction of the method to the experimental capacity of these members was 0.98 with a coefficient of variation less than 8%. Use of R2k to establish the base capacity of the underlying unstrengthened RC girders with this accuracy eliminated the need for additional control specimens. Using this past calibration, the predicted base shear capacity, $V_{R2k\text{-}base}$, was multiplied by a 0.98 bias and used throughout this report to adjust the nominal R2k strength to the expected strength when full-scale specimens were modeled.

The next step calculated the additional shear capacity attributed to NSM-CFRP strips. From the archival research, the full tensile strength of the CFRP strips was not reached when specimens failed because the observed failure modes generally consisted of concrete cracking around the strip instead of rupture of the CFRP. For that reason, an estimated effective stress for the NSM-CFRP strips was needed to estimate capacity gains of the hypothetical specimens. The estimated NSM-CFRP stress was found by review of experiments in previous research and extracting the average NSM-CFRP stresses from these archival specimens. A list of the archival experimental data is shown in Table 5.2. Because the specimens in the present research and actual bridge girders have internal transverse steel reinforcing, only experimental specimens containing internal steel stirrups and a control specimen with internal steel stirrups were considered.

Table 5.2 : Archival experimental specimens used for prediction of NSM-CFRP contribution to shear strength for design of present test specimens.

Researcher and Year	Control Specimen ID	Strengthened Specimen ID
De Lorenzis 2001	BSV	BS90-7A
Dias 2007	2S-R	2S-7LV
	4S-R	4S-7LV
Dias 2008	2S-R	2S-3LV
		2S-5LV
		2S-8LV
Rizzo 2009	C	NB90-73-a
		NB90-73-b
		NB90-45-b
		NS90-73-a
Howell 2009	Control	B.IT.NC.NS
Dias 2010	2S-R	2S-4LV
		2S-7LV
		2S-10LV

Using the reported specimen data, the base strength of each archival specimen was computed using R2k. The predicted shear strength from R2k, the average ultimate shear stress, f_v, in the section was calculated as:

$$f_v = \frac{V}{bd_v} \qquad [5\text{-}1]$$

where V = shear strength determined by R2k, b = width of the specimen, and d_v = the effective depth of the section (taken as the distance between the flexural tension and compression resultants).

The relationship between the average ultimate shear stress with increasing transverse reinforcing steel was developed with the abscissa taken as the average transverse reinforcing pressure of the member calculated as:

$$p_{trans} = \frac{A_v f_y}{bs} \qquad [5\text{-}2]$$

where A_v = area of shear reinforcing, f_y = yield strength of the shear reinforcing, and s = spacing of the shear reinforcing. The calculated base member strength (without NSM-CFRP) was plotted as a point on the graph while the experimentally measured average ultimate shear stress for the NSM-CFRP strengthened specimen was plotted as a horizontal line. The additional shear strength attributed to the NSM-CFRP, $(V_{FRP})_{R2k}$, was determined as the vertical distance between the base member failure point and the retrofitted failure point. Vertical lines were then generated at the control point and where the retrofitted failure line intersected the curve. The horizontal distance between these lines was taken as the increase in transverse pressure, p_{trans}, that allowed the specimen to achieve the experimentally measured shear strength. The effective NSM-CFRP stress, $f_{fe\text{-}R2k,}$ could then be calculated as a function of the cross section of the NSM-CFRP (A_{frp}), spacing (s_{frp}), and the width of the specimen (b) as:

$$f_{fe-R2k} = \frac{p_{trans} b s_{frp}}{A_{frp}} \qquad [5\text{-}3]$$

To include the analysis uncertainty, a 90% probability threshold was generated using the previously described R2k bias (0.98) and COV (8%) for analysis prediction of the specimens. An example of this analysis is shown in Figure 5.2. This process was repeated for each of the relevant experiments in the literature and the results are shown in Table 5.3. An effective NSM-CFRP stress was not able to be obtained for two specimens (*Rizzo 2009 NB90-73-a and Rizzo 2009 NS90-73-a*) as the ultimate shear stresses of these specimens were reportedly very high and did not intersect the mean R2k curve. The mean NSM-CFRP stress was found to be 441 MPa (64.0 ksi). This value was used to predict the additional NSM-CFRP strength for design of the large-size specimens in this resesarch. The scale effects of NSM-CFRP strengthening were not known, and only one specimen in the literature was full-scale and with very widely spaced NSM-CFRP bars (Howell 2009). Therefore, an average of all available specimens strengthened with NSM-CFRP was used. The effective NSM-CFRP stress appeared to be normally distributed as seen in Figure 5.3 and the COV was 53.1%, which indicated large variability for the NSM-CFRP effective stress in the archival literature. In this figure, the Hazen plotting position is the rank order of the experimental results for NSM-CFRP stress from largest to smallest taken as (2r-1)/2n, where r is the r^{th} rank and n is the sample size.

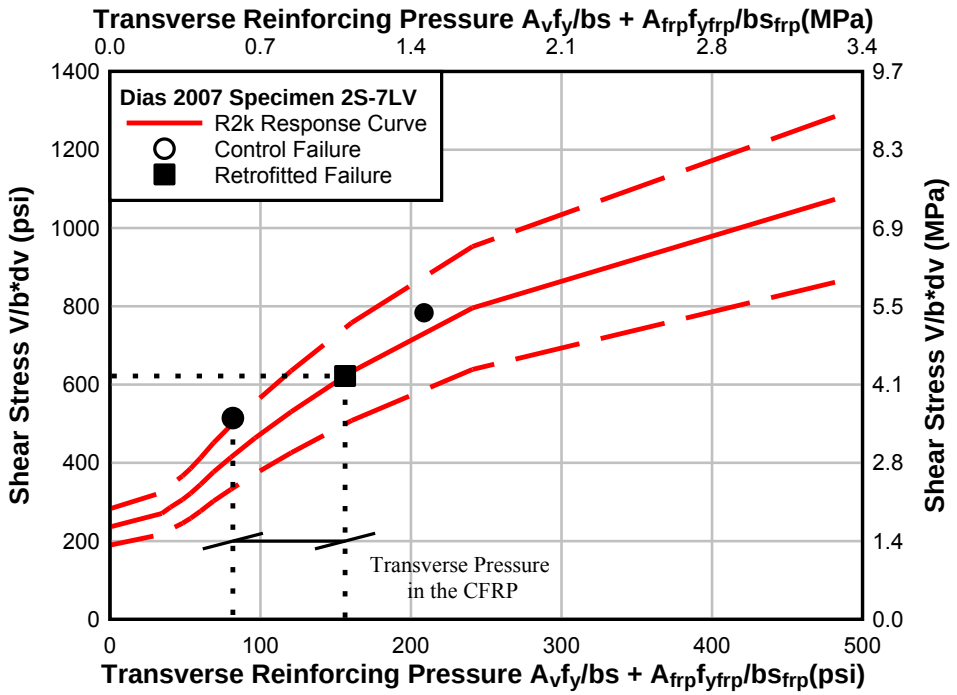

Figure 5.2: Example of interaction between shear strength and amount of transverse reinforcing steel for archival experimental specimens that was used to estimate the NSM-CFRP contribution to the member capacity

Table 5.3: Effective CFRP stresses from literature review

Specimen ID	VEXP (kN) [kips]	VR2k_B (kN) [kips]	VEXP - VR2k_B (kN) [kips]	ffe-R2k (MPa) [ksi]
De Lorenzis 2001 (BS90-7A)	207 [46.5]	157.6 [35.4]	49.4 [11.1]	596 [86.5]
Dias 2007 (2S-7LV)	164 [36.9]	115.5 [26.0]	48.7 [10.9]	378 [54.9]
Dias 2007 (4S-7LV)	189 [42.5]	158.0 [35.5]	31.1 [7.0]	333 [48.3]
Dias 2008 (2S-3LV)	189 [42.6]	135.5 [30.5]	53.5 [12.1]	804 [117]
Dias 2008 (2S-5LV)	214 [48.2]	135.5 [30.5]	78.7 [17.7]	719 [104]
Dias 2008 (2S-8LV)	238 [53.4]	135.5 [30.5]	102.1 [22.9]	595 [86.2]
Rizzo 2009 (NB90-73-a)	176 [39.6]	105.2 [23.7]	70.8 [16.0]	N/A N/A
Rizzo 2009 (NB90-73-b)	149 [33.5]	105.2 [23.7]	43.8 [9.9]	228 [33.1]
Rizzo 2009 (NB90-45-b)	151 [33.9]	105.2 [23.7]	45.8 [10.3]	151 [21.8]
Rizzo 2009 (NS90-73-a)	173 [38.9]	105.2 [23.7]	67.8 [15.3]	N/A N/A
Howell 2009 (B.IT.NC.NS)	740 [166]	734.0 [165.0]	6.0 [1.0]	13 [1.9]
Dias 2010 (2S-4LV)	202 [45.5]	141.4 [31.8]	61.0 [13.7]	558 [81.0]
Dias 2010 (2S-7LV)	225 [50.5]	141.4 [31.8]	83.1 [18.7]	500 [72.5]
Dias 2010 (2S-10LV)	239 [53.6]	141.4 [31.8]	97.1 [21.8]	417 [60.5]
Mean				441 [64.0]
COV (%)				53.1

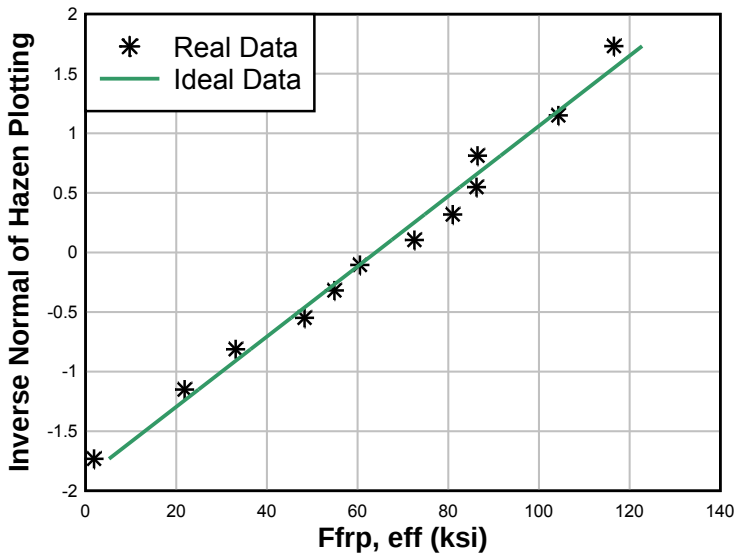

Figure 5.3: Distribution of predicted $f_{fe\text{-}R2k}$ in archival data

Using the average $f_{fe\text{-}R2k}$, the additional shear capacity of the present specimens was predicted. The transverse pressure of the NSM-CFRP retrofitted specimens was calculated as:

$$p_{trans} = \frac{A_v f_y}{bs} + \frac{A_{frp} f_{fe-R2k}}{bs_{frp}} \qquad [5\text{-}4]$$

Graphs were created for each specimen to estimate the retrofitted shear capacity of the specimens. For design, these graphs were based on an estimated concrete compressive strength of 27.6 MPa (4000 psi) and manufacturer reported reinforcing steel strengths of 467 MPa (68 ksi) for the flexural steel and 352 MPa (51 ksi) for stirrups. R2k shear stress-average transverse pressure curves and 90% confidence intervals were created for each specimen. Pre-strengthened and post-strengthened transverse pressures with 90% confidence intervals were calculated and plotted as vertical lines on the graph. Shear stresses were found at the points where the vertical lines intersected the R2k curve. The additional shear stress was determined as the change in shear stress between the two intersections. Shear capacities were then calculated from the shear stresses determined from the graphs. The shear estimated at flexural failure (V_{mn}) was also plotted at the corresponding shear stress at flexural failure as an upper limit for the section indicating that values that fell below this were predicted to fail in shear. A typical graph is shown in Figure 5.4. As shown in Figure 5.4, there was significant uncertainty in the NSM-CFRP effective stress.

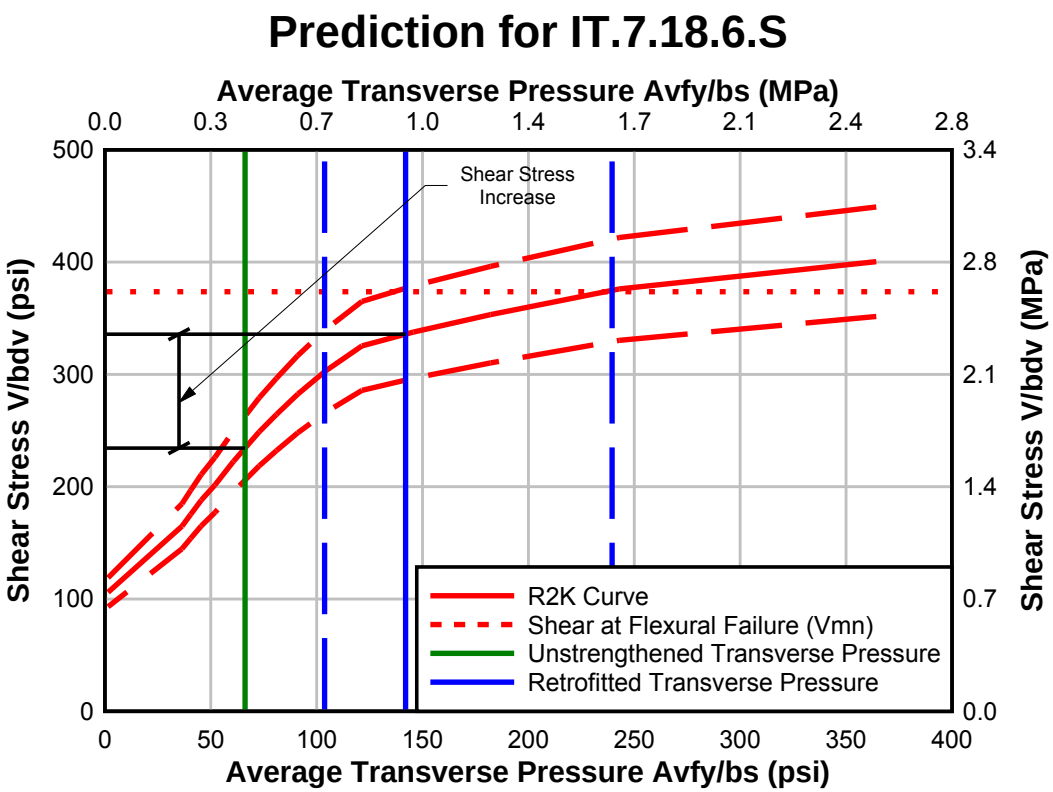

Figure 5.4: Expected shear strength-shear reinforcement relationship for test specimen (the solid vertical blue line is the average transverse reinforcing pressure given the increase in shear stress at ultimate and the dashed blue lines are the upper and lower 90% probability average transverse reinforcing pressures for the given increase in average shear stress at ultimate)

It should be noted that different IT sections were considered for test specimens with five (5) 36 mm (#11) flexural reinforcing bars and for seven (7) 36 mm (# 11) flexural reinforcing bars as seen in Figure 5.5. The curves in Figure 5.5 were different because they were based on MCFT, which accounts for the effect of flexural reinforcing on shear strength. A notable feature of these curves was that they did not represent a linear increase in shear stress with increasing transverse reinforcing over the range of values, as would be predicted using the ACI approach as described later in this report. It can be seen in Figure 5.5 that the IT with more flexural bars retained the steeper slope over a wider range of transverse reinforcing values. Therefore, by adding the same amount of transverse reinforcing to both cross-sections, the shear capacity of the specimen with seven flexural bars should exhibit a larger increase in shear strength than the specimen with five flexural bars. This interaction is an important practical consideration to ensure that a design can actually achieve the desired strength, especially for girders with low flexural reinforcing ratios. It is also important because in nearly all of the previous research on NSM-CFRP strengthened specimens, heavy flexural reinforcing was used to insure shear failure. Due to this over-reinforcement, the shear strength gains attributed to the NSM-CFRP reinforcing reported in the research are likely larger than what would be observed in realistic field installations. To consider this interaction, specimens were constructed with both five and seven flexural reinforcing bars and the same amount of transverse reinforcing.

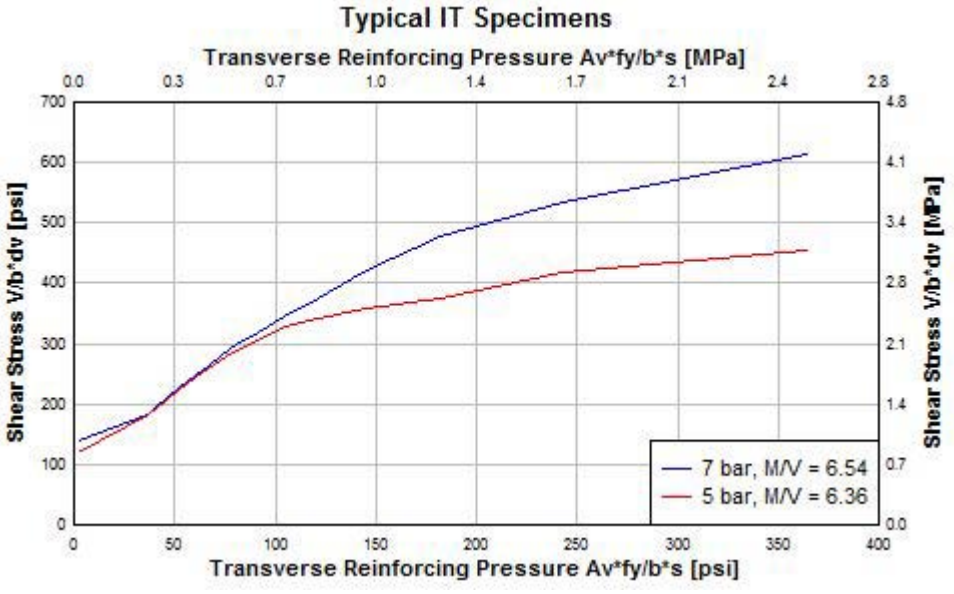

Figure 5.5: Shear-transverse reinforcing pressure interaction for IT specimens with different amounts of flexural reinforcing steel

Two different NSM-CFRP strip spacings of 152 mm (6 in.) and 305 mm (12 in.) were considered. These spacings were chosen because they provided substantial strength gains above the control and were thought to keep the estimated strength below the flexural capacity of the beams. Originally, the research plan was to study two T specimens, two IT specimens with five flexural bars, and two IT specimens with seven flexural bars for strength evaluation. The four durability IT specimens were to be constructed with seven flexural bars and 152 mm (6 in.) NSM-CFRP spacing. This provided the largest difference in shear capacity between the specimen and the non-retrofit control so any degradation due to environmental exposure would be easier to distinguish.

All of the specimens were to be constructed with 457 mm (18 in.) internal steel stirrup spacing to correspond with previous tests done at Oregon State University and represent a realistic amount of internal steel stirrups near the minimum prescribed by design specifications. The first specimen constructed and tested was an IT with seven 36 mm (#11) bars. This specimen turned out to be stronger than predicted and was at the limits of the hydraulic testing capacity in the laboratory. Therefore, one of the IT specimens with five bars was not constructed; instead an IT with seven flexural bars, 559 mm (22 in.) stirrups, and 152 mm (6 in.) NSM-CFRP spacing was constructed to use as a control in order to lower the final failure load of the remaining unconstructed specimens. The one IT specimen constructed with five bars was also constructed with 559 mm (22 in.) stirrups and strengthened with 152 mm (6 in.) CFRP strip spacing, but this specimen started to fail in flexure. To achieve a shear dominated failure, half the NSM-CFRP was removed by saw-cutting it out of the specimen. This will be discussed further in the results section, but this resulted in the specimen having 305 mm (12 in.) CFRP strip spacing. With all these factors taken into account, the specimens constructed are shown on the curves in Figure 5.6. The baseline points represent the cross-sectional strength without any NSM-CFRP retrofit. The predicted shear strengths of the specimens based on these curves as well as the expected shear at flexural failure are listed in Table 5.4.

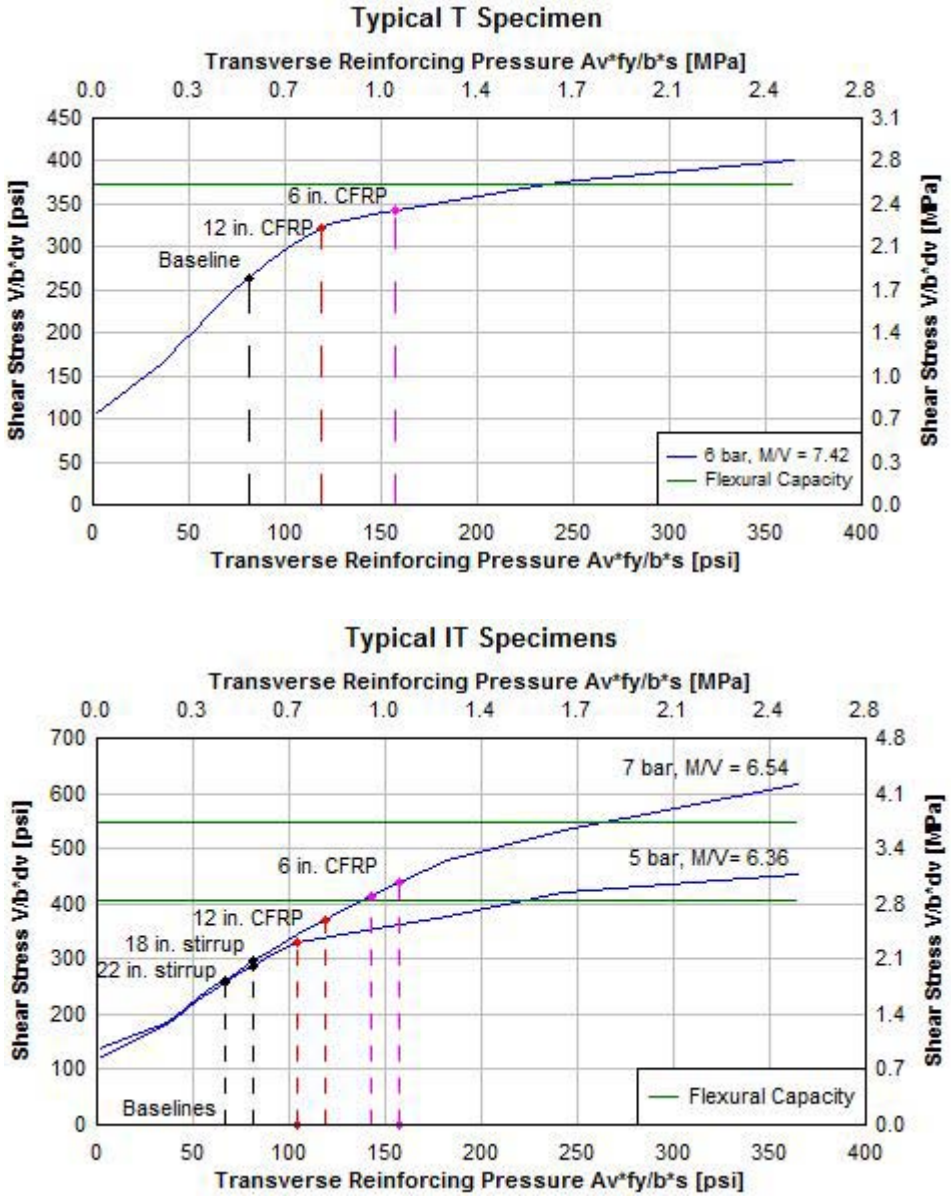

Figure 5.6: Shear stress vs. transverse reinforcing pressure interactions for specimen designs

Table 5.4: Initially predicted shear strengths for specimens.

Specimen ID (order of testing)	Predicted Shear Strength		Predicted Shear at Flexural Failure	
	(kN)	(kip)	(kN)	(kip)
T.6.18.6-S (3)	876	197	952	214
T.6.18.12-S (4)	823	185	952	214
IT.7.18.6-S (1)	1023	230	1281	288
IT.7.18.12-S (6)	867	195	1281	288
IT. 7.22.6-S (7)	965	217	1281	288
IT.5.22.12-S (5)	814	183	1010	227
IT.7.22.6-FT/FTG (9)	965	217	1281	288
IT.7.22.6-FTG (10)	965	217	1281	288
IT.7.18.6-M (2)	1023	230	1281	288
IT.7.22.6-FT (8)	965	217	1281	288

5.3 TEST SPECIMENS

Specimens were designed to represent in-situ vintage reinforced concrete bridge deck girders of the 1950s. T and IT specimens were used to model the shear with positive moment and negative moment as commonly encountered in these bridges. Half of each specimen was retrofitted with NSM-CFRP while the other half was over-reinforced in shear to induce failure in the retrofitted side as shown in Figure 5.7. The specimens had a total height of 1219 mm (48 in.), a flange width of 914 mm (36 in.), a flange thickness of 152 mm (6 in.), and a web thickness of 364 mm (14 in.). The shear span of IT specimens was 2997 mm (118 in.) while T specimens had a shear span of 3353 mm (132 in.) Transverse and longitudinal steel consisted of #13 (#4) open stirrups and #36 (#11) bars respectively. Cross-sections of the specimens are shown in Figures 5.8 - 5.10.

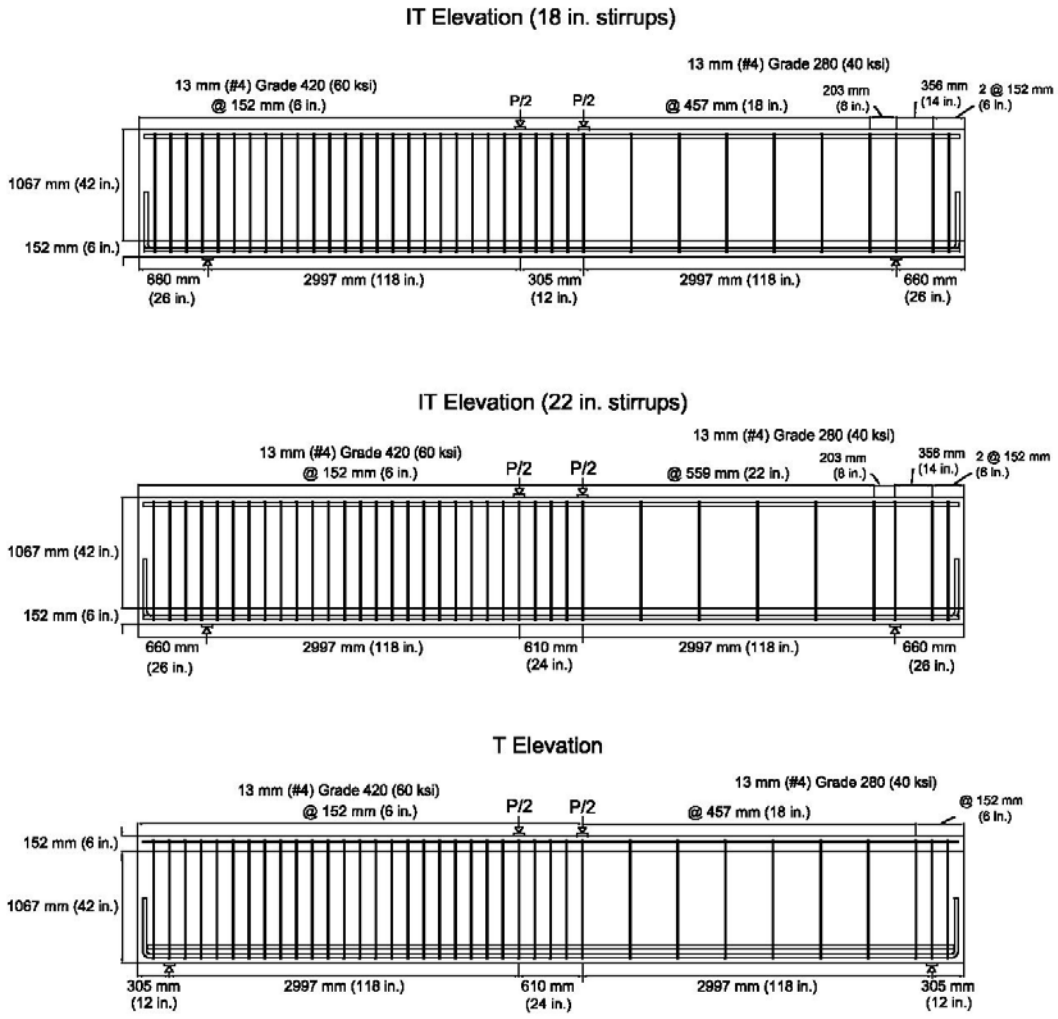

Figure 5.7: Specimen elevation view with internal steel reinforcing

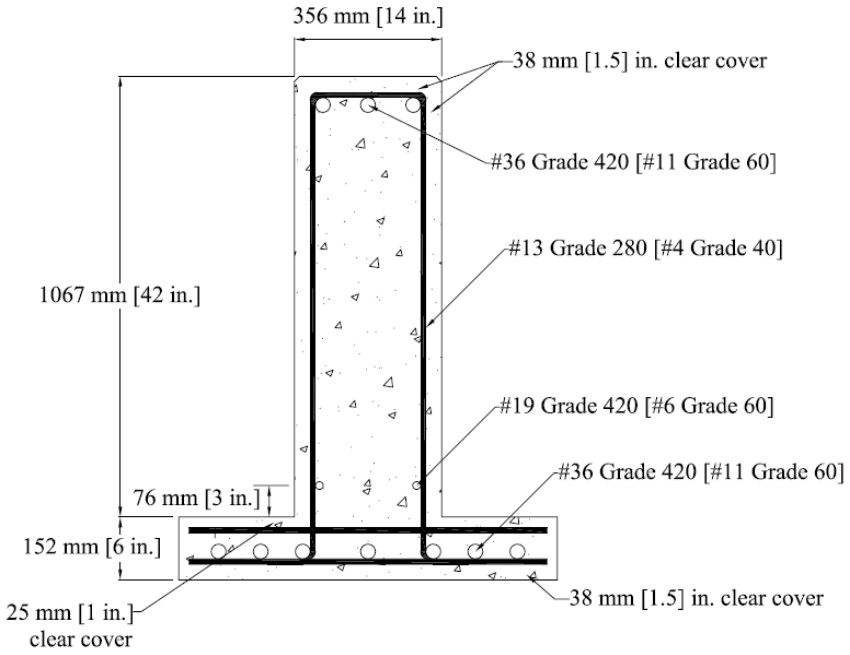

Figure 5.8: Typical T cross-section with 7 flexural reinforcing bars

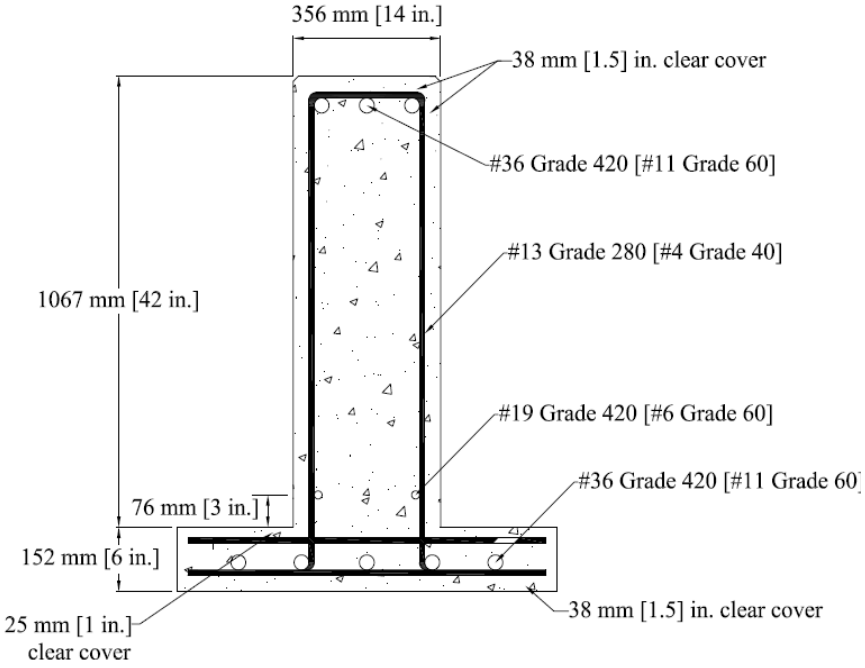

Figure 5.9: Typical cross-section with 5 flexural reinforcing bars

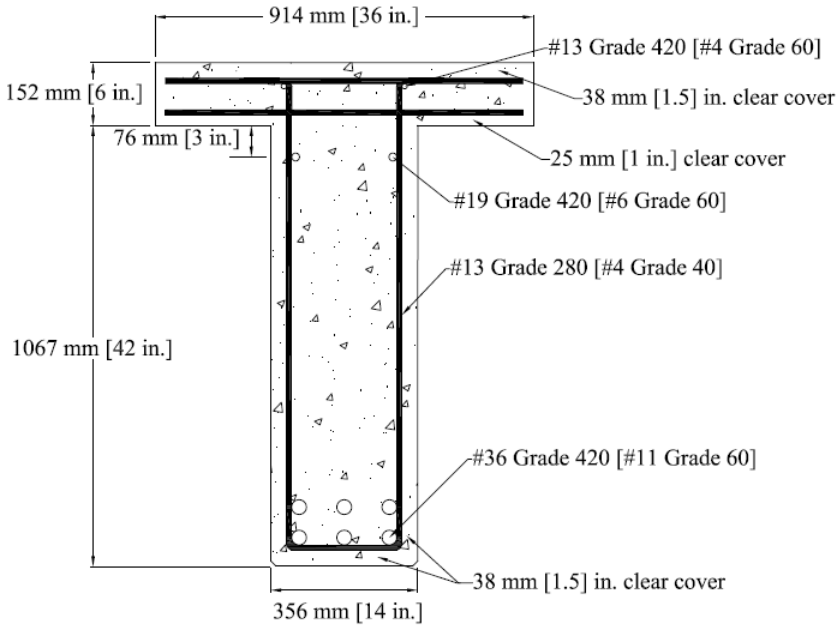

Figure 5.10: Typical T cross-section

5.4 MATERIALS

Materials were chosen to best represent those of in-situ bridge deck girders constructed in the middle of the last century. This entailed using steel and concrete with properties typical of vintage bridges. NSM-CFRP retrofitting materials were chosen by considering several factors that will be discussed in this section.

5.4.1 Concrete

The concrete mixture used was representative of vintage concrete bridges and the design was based on 1950's AASHTO "Class A" concrete that has been used in previous research at Oregon State University (*Higgins et al. 2005*). Concrete was supplied by a local ready-mix supplier. Willamette River bed deposits made up the coarse aggregate. The supplier reported the aggregate composition for the mix as follows: 97% passing the 19 mm sieve (3/4 in.), 82% passing 16 mm (5/8 in.), 57% passing 12.5 mm (1/2 in.), 33% passing 9.5 mm (3/8 in.), 21% passing 8 mm (5/16 in.), 9.3% passing 6.3 mm (1/4 in.), 3.0% passing 4.75 mm (#4), 0.6% passing 2.36 mm (#8), and 0.3% passing the 0.075 mm (#200) sieve. The supplier reported the sand composition of the mix to be 99.7% passing the 6.3 mm sieve (1/4 in.), 96.8% passing 2.36 mm (#8), 59.4% passing 1.18 mm (#16), 44.9% passing 0.600 mm (#30), 17.9% passing 0.300 mm (#50), 3.7% passing 0.150 mm (#100), and 1.7% passing the 0.075 mm (#200) sieve. Concrete admixtures consisted of 58 mL/m^3 (1.5 oz/yd^3) of Daravair and 735 mL/m^3 (19 oz/yd^3) of WRDA-64. These were principally used for workability during placement. Before casting, a standard slump test was performed using the concrete. Water was added on site until an approximate slump of 127 mm (5 in.) was achieved. The specified compressive strength for the mix was 21 MPa (3000 psi). This strength is comparable to the specified design strength of vintage 1950's bridges. The actual compressive strength of the concrete was determined from 152 x 305 mm (6 in. x 12 in.)

cylinders in accordance with ASTM C39M/C 39M-09a and ASTM C617-09a. The cylinders were cured under ambient air conditions in the laboratory. Average precrack and test day compressive strengths are shown in Table 5.5. While a minimum concrete strength of 20.7 MPa (3000 psi) was specified for all specimens, this table shows the variability in concrete strength as well as the concrete strength gained over time. In all subsequent analyses of the specimens the actual day-of-test concrete strengths are used.

Table 5.5: Average precrack and day-of-test concrete compressive strengths

Specimen	Concrete Age At Precrack (days)	f'c at Precrack (Mpa) [psi]	Concrete Age At Failure (days)	f'c at Failure (Mpa) [psi]
T.6.18.6.S	28	24.9 [3604]	65	25.71 [3729]
T6.18.12.S	29	28.2 [4095]	76	29.21 [4236]
IT.7.18.6.S	34	31.2 [4529]	56	31.07 [4506]
IT.7.18.12.S	28	27.0 [3920]	98	30.85 [4475]
IT.5.18.12*.S	28	27.0 [3920]	59	30.03 [4355]
IT.7.22.6.S	27	24.4 [3536]	56	27.21 [3946]
IT.7.22.6.FTG	72	29.2 [4237]	169	32.05 [4649]
IT.7.22.6.FT/FTG	21	30.4 [4402]	181	37.01 [5368]
IT.7.18.6.M	28	26.5 [3838]	267	26.8 [3889]
IT.7.22.6.FT	28	29.0 [4201]	189	30.1 [4361]

5.4.2 Reinforcing Steel

The # 13 Grade 300 (# 4 Grade 40) transverse reinforcing steel used in this experiment was representative of vintage 1950s bridge girders that used Intermediate Grade steel (nominal 40 ksi yield). Other reinforcing steel was ASTM A615 Grade 60. Material tests were performed on the stirrups located in the retrofitted portion of the specimens and on the flexural reinforcing bars. The actual tensile properties of the steel were tested based on ASTM E8/E8M-09a. The coupons for the flexural 36mm (#11) bars were machined down to 13 mm (0.5 in.) diameter samples to be tested. Results from coupon tests are shown in Table 5.6. It is of interest to note that the deformation patterns used in modern reinforcing bars have not changed since they were

introduced in the late 1940's, and thus bond and anchorage between modern and vintage round deformed bars are expected to be similar.

Table 5.6: Reinforcing steel properties

Description	Bar Size	Grade (Mpa) [ksi]	fy (Mpa) [ksi]	fu (Mpa) [ksi]
Stirrups	# 13 [# 4]	300 [40]	350 [50.7]	556 [80.7]
Flexural Reinforcing	# 36 [# 11]	420 [60]	478 [69.3]	712 [103.3]

5.4.3 NSM-CFRP Materials

When selecting the NSM-CFRP material it was decided that rectangular strips of CFRP would be better suited for the present NSM application than round bars. The narrow rectangular strips fit into a thinner saw-cut groove than a round bar, which means reduced saw cutting and less exposure to environment. A rectangular strip also provides more surface area for bonding with the epoxy. One of the only commercially available rectangular CFRP strips used previously for NSM strengthening and the most popular one in the United States is made by Hughes Brothers, of Seward, Nebraska. Hughes Brothers carbon fiber has been used in previous research for NSM applications, and the carbon fiber strips have a unique roughened surface. Hughes Brothers Aslan 500 rectangular carbon fiber tape was chosen as the principal CFRP material for this study.

Several alternative carbon fiber materials and epoxies were also investigated during the material selection process. Availability, economic efficiency, and structural properties were taken into consideration. Two alternative carbon fiber materials and three different epoxies were chosen in addition to the Hughes Brothers material for bond testing. Only one combination of materials, (carbon fiber material and epoxy) was chosen for full-scale girder testing.

Effort was made to select carbon fiber materials that had similar tensile strength. This was done by balancing the material strength and cross-sectional area of the strips. The three carbon fiber materials chosen were Hughes Brothers Aslan 500 (C1), S&P Laminates CFK 150/2000 (C2), and a generic carbon fiber material (C3). Coupon tests were performed according to ASTM D 3039 to determine the actual material properties. In an effort to prevent damage to the CFRP coupons in the grips during testing, the CFRP strips were indirectly gripped by bonding fiberglass computer board in the grip region. Coupons often failed prematurely due to unbalanced gripping or misalignment. Only coupons that failed by rupturing / brooming of the CFRP fibers were used to establish the CFRP composite tensile strength shown in Table 5.7. An example of brooming is shown in Figure 5.11. The elastic modulus for specimen C1 was taken from previous testing performed by Howell (*2009*). The elastic modulus for C2 and C3 are those reported by the manufacturer. The elastic modulus could not be established directly due to instrumentation slip during tests.

Table 5.7: CFRP composite properties

CFRP Type	Tensile Stress at Failure (Mpa) (ksi)	Elastic Modulus (Mpa) (ksi)
C1	118 [17.2]	138,458 [20081]
C2	53 [7.7]	165,004 [23931]
C3	92 [13.3]	134,004 [19435]

Figure 5.11: Brooming failure of CFRP coupon

The epoxy chosen for the girder tests was BASF Concresive 1420 (called E1 in this report). This epoxy is one recommended by Hughes Brothers to be used with their CFRP and was investigated in a previous experiment (*Shield et al. 2005*). Other epoxies investigated in Shield et al. (*2005*) were either no longer available or not cost effective. The material properties of the epoxy as reported by the manufacturer are shown in Table 5.8.

Table 5.8: Epoxy properties as reported by manufacturer

Epoxy Name Designation	Tensile Strength MPa [psi]	Compressive Strength MPa [psi]	Compressive Modulus MPa [psi]	Bond Strength MPa [psi]	Recommended Curing Time
E1	34.5 [5030]	67.6 [9800]	2900 [4.2 x 105]	20.7 [3000]	7 Days

5.5 SPECIMEN CONSTRUCTION AND INSTRUMENTATION

Specimens were constructed at the Oregon State University Structural Engineering Research Laboratory within the Hinsdale Building. Formwork from previous research with similarly sized members was reused in this program. Prior to casting the concrete, selected reinforcing bars were instrumented with strain gages. CEA-06-125UN-120 general purpose strain gages were applied to the stirrups on the under-reinforced half of the specimens at mid-height as well as the flexural bars at midspan. Flexural reinforcing steel strain gages were numbered as shown in Figure 5.12. Steel stirrup strain gages were numbered beginning with the stirrup closest to midspan. Rebar cages were constructed and tied with standard rebar ties. Cages were constructed individually using supports to hold the steel until placement into the forms as seen in Figure 5.13. Two specimens were constructed at a time. Tamms Formlock 250 was used as a release agent on the formwork. Slab bolsters and side cover spacers were used to ensure adequate clear cover of 38 mm (1.5 in.). After the reinforcing steel cages were placed into the forms, concrete was placed using multiple lifts and consolidated with a concrete vibrator. For each beam, a concrete truck containing approximately 4.78 m^3 (6.25 yd^3) of concrete was used. The concrete truck for specimen T.6.18.12.S contained 6.31 m^3 (8.25 yd^3). This extra concrete was used to construct the bond specimens from a single batch of concrete. Once the concrete was placed, it was screeded and troweled to obtain a level and smooth surface. After the specimens reached an initial set, they were covered with burlap and plastic. Specimens were kept moist in the forms for a minimum of seven days.

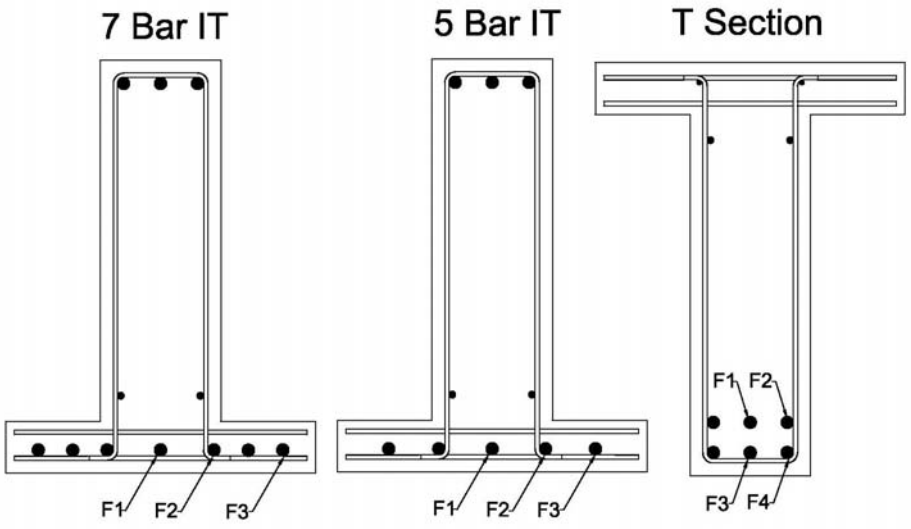

Figure 5.12: Flexural reinforcing strain gage locations

Figure 5.13: Example of reinforcing cage (T specimen shown)

After curing, the specimens were removed from the formwork and placed in the testing apparatus. During this time, additional instrumentation was applied. Six 12.7 mm (0.5 in.) string potentiometers were used to measure the diagonal displacements across regions of the specimen. The sensors were arranged in pairs. When a diagonal crack formed or widened, one of the sensors elongated while the other contracted. Sensors were located on the retrofitted half of the specimens and their arrangement is shown in Figure 5.14.

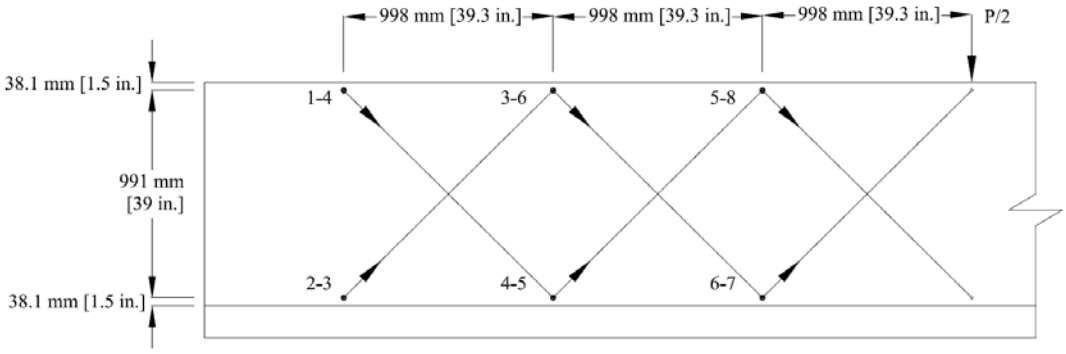

Figure 5.14: Typical diagonal displacement sensor layout

Midspan displacements were obtained using 127 mm (5 in.) string potentiometers placed at the east and west faces of the specimen relative to the strong floor. Support displacements were measured using 13 mm (0.5 in.) range displacement sensors as seen in Figure 5.15. These displacement sensors were also measured relative to the strong floor. This setup allowed for the support displacements to be removed from the center line displacement measurements to eliminate rigid body motions (such as nonconservative contact surfaces between the specimen on bearing plates and rollers). Support displacements were averaged and then subtracted from the average of the east and west midspan displacements to remove the rigid body motion of the specimens. A 2224 kN (500 kip) nominal capacity load cell was attached to the actuator to measure the load applied to the specimen. The measurements from these instruments were

recorded by a commercially available high-speed, multi-channel 16-bit data acquisition system controlled by commercially available acquisition and control software.

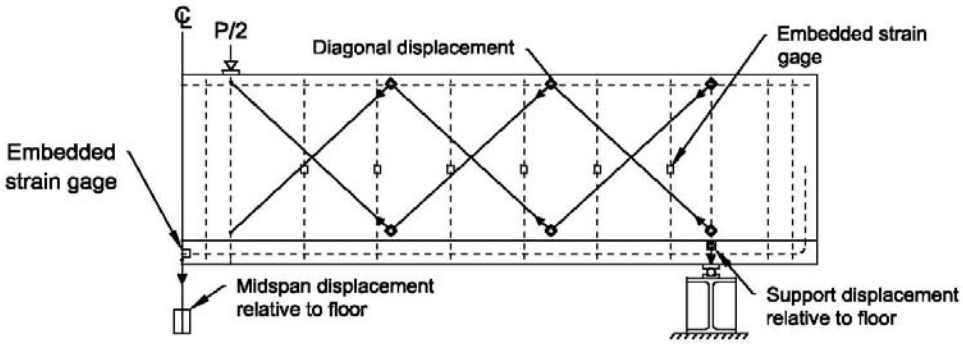

Figure 5.15: Schematic of specimen instrumentation

5.6 RETROFITTING METHODOLOGY

While previous research included specimens with NSM-CFRP bars oriented vertically and at angles perpendicular to diagonal cracks, this experimental program was performed with NSM-CFRP bars oriented vertically only. This was done as a practical measure so that during concrete cutting to produce grooves, no accidental damage would occur to the underlying steel stirrups. In bridges of this era, the reinforcing cages are often not symmetrically located in the cross section. Thus the cover is not equal on opposite sides and a diagonal cut has a much higher potential to nick or cut through existing stirrups.

Specimens were retrofitted in a multistep process. Vertical grooves were cut into the concrete surface of the specimens using a hydraulic powered concrete wall saw fixed to the specimen. Diamond saw blades were stacked to enable the groove width (discussed below) to be made in a single pass. Near the flange of the specimens, a hand saw was used so that the large diameter blade of the wall saw would not damage the flanges of the specimens on overcuts. The hand held grinder also ensured the groove depth in the stem ran all the way to the deck soffit. The groove dimensions were determined to meet ACI 440.2R-08 section 13.3 which states the groove width must be at least three times the CFRP width and the groove depth must be at least 1.5 times the CFRP depth. Based on the Aslan 500 dimensions of 16 mm (0.63 in.) by 2 mm (0.079 in.) the following requirements must be met:

$$\text{Groove depth} > 1.5 * 0.63 \text{ in.} = 0.945 \text{ in.} \qquad [5\text{-}5]$$

$$\text{Groove width} > 3.0 * 0.079 \text{ in.} = 0.237 \text{ in.} \qquad [5\text{-}6]$$

The grooves cut in the specimens had a depth of 25 mm (1.0 in.) and a width of 8 mm (0.31 in.) to meet the requirements. An image of groove cutting and the final groove layout for a specimen is shown in Figure 5.16.

After cutting, the grooves were cleaned using a 20.7 MPa (3000 psi) pressure washer. CFRP strips were cleaned with acetone and air dried. At crack locations observed during precrack

testing, CEA-06-125UN-120 general purpose strain gages were applied to the CFRP strips. It was anticipated that these locations would experience the highest strains. Once the grooves and CFRP strips were dried, the grooves were filled approximately half way with epoxy as shown in Figure 5.17, and the CFRP strips were inserted into the epoxy-filled groove. The CFRP strips were placed in the center of the groove. No centering devices were used. Additional epoxy was then applied to ensure full coverage of the CFRP, and excess epoxy was removed using a trowel.

Figure 5.16: Typical vertical groove cutting technique and finished grooves

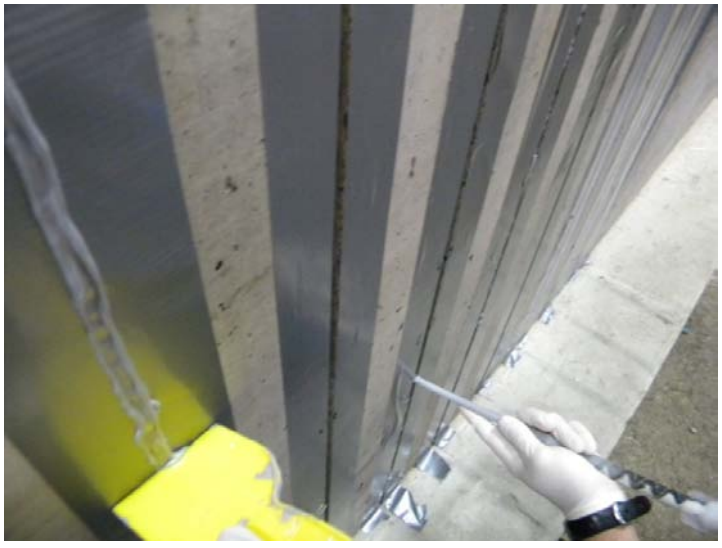

Figure 5.17: Epoxy placement over CFRP in saw cut grooves

The curing time and temperature for epoxy material E1, as provided by the manufacturer, was 7 days at 25°C (77°F) to achieve the reported structural properties. Average curing temperatures and relative humidities are shown in Table 5.9. The epoxy was conditioned between 16 and 27°C (60 and 80°F), and the concrete specimens were above 4°C (40°F) when applied. The

epoxy was allowed to cure for at least seven days to ensure a full cure. On colder days during the winter, a tarp was erected over the specimens with a heater placed inside to maintain curing temperatures within the manufacturer specified limits.

Table 5.9: Average curing temperature and relative humidity

Specimen	Avg. Cure Temp. (°C) [°F]	Avg. Cure RH (%)
T.6.18.6.S	21.7 [71]	58
T.6.18.12.S	21.7 [71]	58
IT.7.18.6.S	21.7 [71]	58
IT.7.18.12.S	17.8 [64]	64
IT.5.22.12*.S	18.3 [65]	65
IT.7.22.6.S	13.3 [56]	72
IT.7.22.6.FTG	17.8 [64]	46
IT.7.22.6.FT/FTG	17.2 [63]	63
IT.7.22.6.M	21.7 [71]	58
IT.7.22.6.FT	19.4 [67]	61

5.7 STRUCTURAL TESTING METHODOLOGY

Specimens were tested in the Structural Engineering Research Laboratory at Oregon State University. All specimens were tested in four-point bending using a 2224 kN (500 kip) rated hydraulic actuator. For the T specimens, lateral bracing was placed at the support locations to ensure stability. The test setup is shown schematically in Figure 5.18. Specimens were supported on 102 mm (4 in.) wide bearing plates that rested on 51 mm (2 in.) diameter cold-rolled steel rollers. Load was applied through a spreader beam attached to the actuator. The spreader beam was centered at the midspan of the specimens and applied load through 51 mm (2 in.) diameter rollers that rested on 102 mm (4 in.) wide bearing plates. The span of the spreader beam was 610 mm (24 in.).

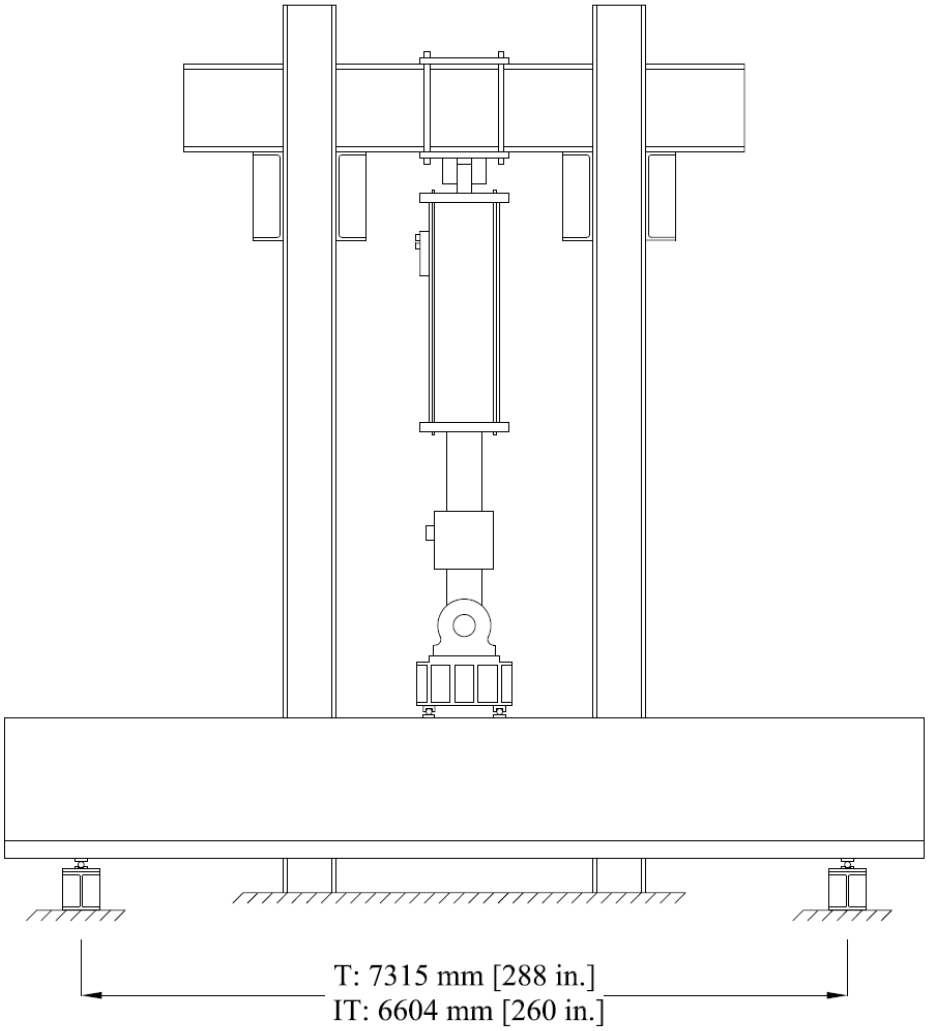

Figure 5.18: Schematic of test setup for girder tests

Before retrofitting, specimens were first precracked to a load of 890 kN (200 kip) to produce diagonal cracking conditions similar to those observed in existing bridges (*Higgins et al. 2005*). The magnitude of the precrack load was based on previous testing performed by Howell (*2009*), who found that a precrack load of 1112 kN (250 kip) resulted in some losses of internal strain gages. Therefore, the precrack load was reduced to 890 kN (200 kip). Table 5.10 shows the precrack load in terms of the shear capacity of the girder without NSM-CFRP as determined using R2k using the actual material properties.

Table 5.10: Load applied to produce initial diagonal cracking of girders

Specimen	Calculated Unstrengthened Shear Capacity Using R2k (kN) [kips]	% of Shear Capacity at Precrack %
T.6.18.6.S	719 [162]	62
T.6.18.12.S	754 [169]	59
IT.7.18.6.S	798 [179]	56
IT.7.18.12.S	793 [178]	56
IT.5.22.12*.S	680 [153]	65
IT.7.22.6.S	676 [152]	66
IT.7.22.6.FTG	641 [144]	69
IT.7.22.6.FT/FTG	671 [151]	66
IT.7.22.6.M	749 [168]	60
IT.7.22.6.FT	700 [157]	64

Tests were performed using a load step process. Load was applied at 111 kN (25 kip) intervals up to 445 kN (100 kip). Additional load was then applied using 222 kN (50 kip) load steps. After each load was reached, the load was reduced by 111 kN (25 kip) and cracks were identified and photographs were taken. Once the cracks were marked, the load was removed before loading the specimen to the next higher load step.

For the precrack loading phase, after 890 kN (200 kip) was reached, the load was removed and the same loading sequence was repeated to obtain baseline behavior of the specimen in the fully cracked condition. This baseline test demonstrated the behavior of a specimen with preexisting cracks but without NSM-CFRP applied. This could then be directly compared to tests results after the NSM-CFRP application within the coincident low load range. After installation and curing of the NSM-CFRP and in some cases additional environmental, fatigue or combined environmental and fatigue exposure, the specimens were loaded to failure using the same loading protocol as described above.

5.8 FATIGUE CYCLING

Specimens IT.7.22.6.FTG and IT.7.22.6.FTG/FT were subjected to high-cycle fatigue loading to simulate the effects of exposure to ambient truck traffic. A fatigue testing protocol was developed in such a way as to rationally induce service life fatigue damage in a reasonable

amount of time in the laboratory setting. Previous research (*Higgins et al. 2007*) identified an equivalent damage for vehicle loading for a 50 year period based on stress ranges measured in situ on vintage bridges. The equivalent stress range was determined from field instrumentation taken from four bridges and measuring the stress ranges experienced by the stirrups at diagonal crack locations in the vintage bridges. The vehicle loading and frequency data collected during monitoring was conservatively projected to apply over the entire life of the bridge. An equivalent stress range, SR_{eqv}, was found to be 98 MPa (13.8 ksi) using Miner's Rule:

$$SR_{eqv} = \sqrt[3]{\sum \frac{n_i}{N_{tot}} SR_i^3} \qquad [5\text{-}7]$$

where SR_i = the i^{th} stress-range, n_i = the number of cycles for the i^{th} stress-range, and N_{tot} = the total number of cycles for all stress ranges (*Miner 1945*). Using Equation 5-7, the fatigue loading was developed to produce 50 years of equivalent damage at an accelerated rate. Specimen IT.7.22.6.FTG was subjected to an internal steel stirrup stress range of 120 MPa (17.4 ksi), which was equal to 34.3% of the yield stress, and application of 1,000,000 load cycles, which produced the equivalent damage of 50 years of service life. Because a smaller actuator was available for specimen IT.7.22.6.FTG/FT, the stress range was 89.5 MPa (13.0 ksi), equal to 25.6% of the yield stress, and required 2,400,000 load cycles to produce the equivalent damage. The maximum loading rates were 0.6 Hz and 2.5 Hz for specimens IT.7.22.6.FTG and IT.7.22.6.FTG/FT, respectively. A sinusoidal loading function was used for both specimens. In order to track the behavior and stiffness of these specimens, strain and deflection data were collected before any fatigue cycles were applied and then at intervals during fatigue testing. For specimen IT.7.22.6.FTG the interval was every 100,000 cycles; for specimen IT.7.22.6 FTG/FT, the interval was 100,000 cycles for the first 1,400,000 cycles and every 250,000 cycles thereafter. Data were collected for the full load range for ten cycles at a very slow loading rate of 0.1 Hz. Ten cycles of full load range were applied before collecting data to ensure the sensors were well seated. After data were collected, a visual inspection was made to check for cracking, signs of debonding, or other deterioration. The fatigue loading programs for the fatigue specimens are shown in Table 5.11. The loading protocols varied for each specimen due to the different stress ranges. The stress ranges from the embedded steel stirrups were below the threshold for metal fatigue of reinforcing steel (considered to be 20 ksi by ACI 215) as observed in previous research by Higgins et al. (*2005*).

Table 5.11: Fatigue loading test conditions for specimens

Specimen	Cycles	Measured Stress Range (MPa) [ksi]	Fatigue Test Applied Mean Load (kN) [kip]	Fatigue Test Applied Load Range (kN) [kip]	Interval Test Maximum Applied Load (kN) [kip]
IT.7.22.6.FTG	1,000,000	120 [17.4]	431 [97]	329 [74]	574 [129]
IT.7.22.6.FT/FTG	2,400,000	89.5 [13.0]	378 [85]	222 [50]	467 [105]

Fatigue loading for specimen IT.7.22.6.FTG was applied using the same setup as that used to test the specimens to failure. Specimen IT.7.22.6.FTG/FT was fatigued while the specimen was simultaneously being subject to freeze-thaw conditions. The large environmental test setup is illustrated schematically in Figure 5.19. The setup consisted of a 489 kN (110 kip) fatigue rated hydraulic actuator in three-point bending. The load cell for the fatigue actuator had a capacity of 667 kN (150 kip). The shear span for fatigue loading was extended from 2997 mm (118 in.) to 3353 mm (132 in.) in an effort to avoid freeze-thaw damage at the support locations when tested to failure. Increasing the shear span in turn increased the flexural stresses. Due to shear-flexural interaction, the stresses in the steel stirrups increased as well. Therefore, the fatigue loading program for Specimen IT.7.22.6.FT/FTG was conservative, and the equivalent damage was expected to be greater than 50 years.

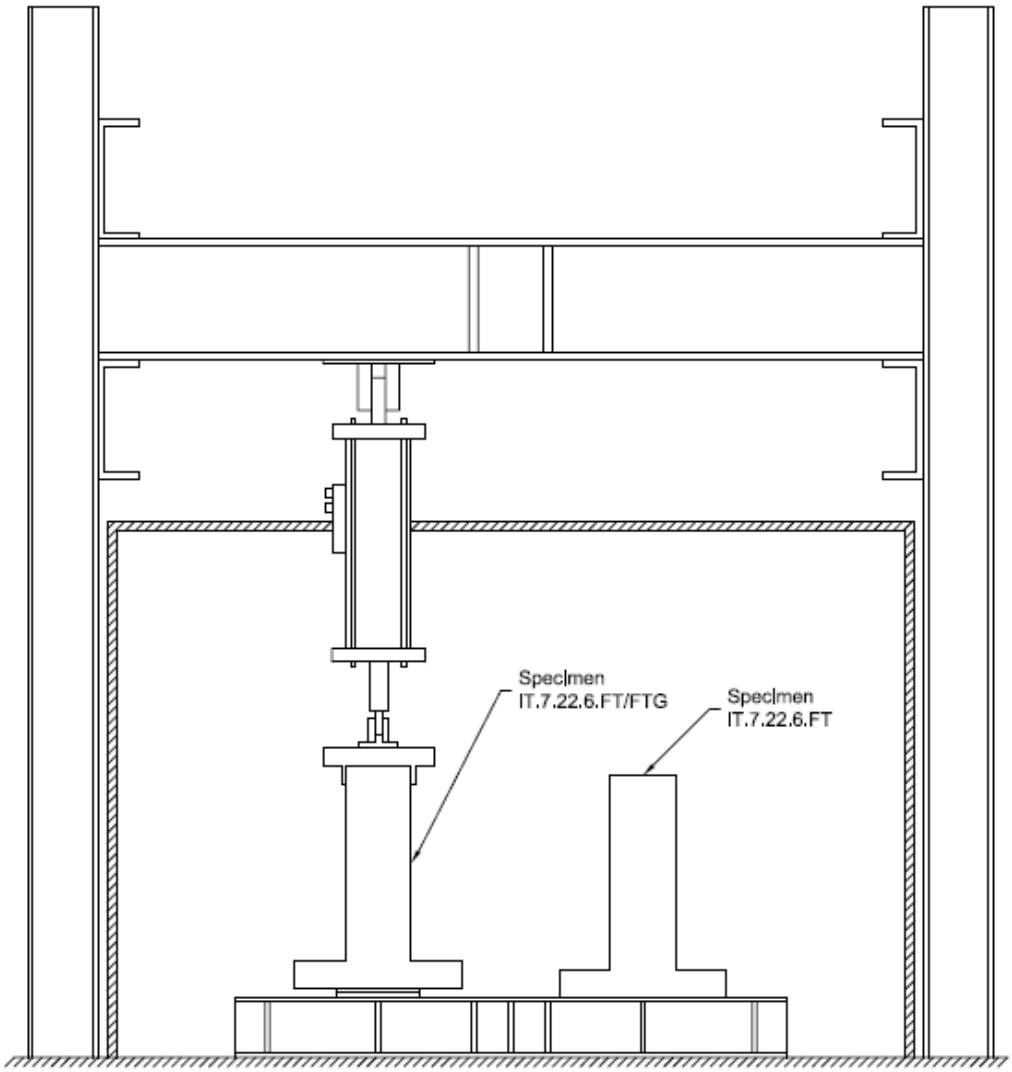

Figure 5.19: Freezer and fatigue setup

5.9 ENVIRONMENTAL EXPOSURE

In addition to fatigue loading, specimen IT.7.22.6.FT/FTG was subjected to 400 cycles of freeze-thaw. Ambient air temperatures of the freeze-thaw cycles ranged between -20 °C (-4.0 °F) and 16 °C (60.8 °F) with ramp times of 30 minutes and soak times of 1 hour. Type T thermocouples were used to monitor the temperature of the specimen. Thermal couples were attached to the surface of the specimen at each end. Additional thermal couples were attached at midspan on the surface of the specimen and at depths of 12.7 mm (0.5 in.), 25.4 mm (1.0 in.), and 44.5 mm (1.75 in.) to ensure freezing of the entire depth of the NSM-CFRP system for each cycle. The thermocouple layout is shown in Figure 5.20. Example freeze-thaw temperatures on the surfaces and internally on the specimen are shown in Figure 5.21.

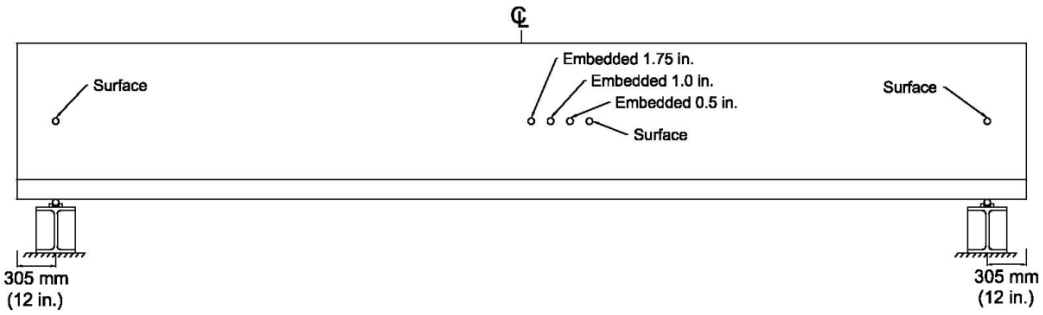

Figure 5.20: Thermocouple location on specimen IT.7.22.6.FT

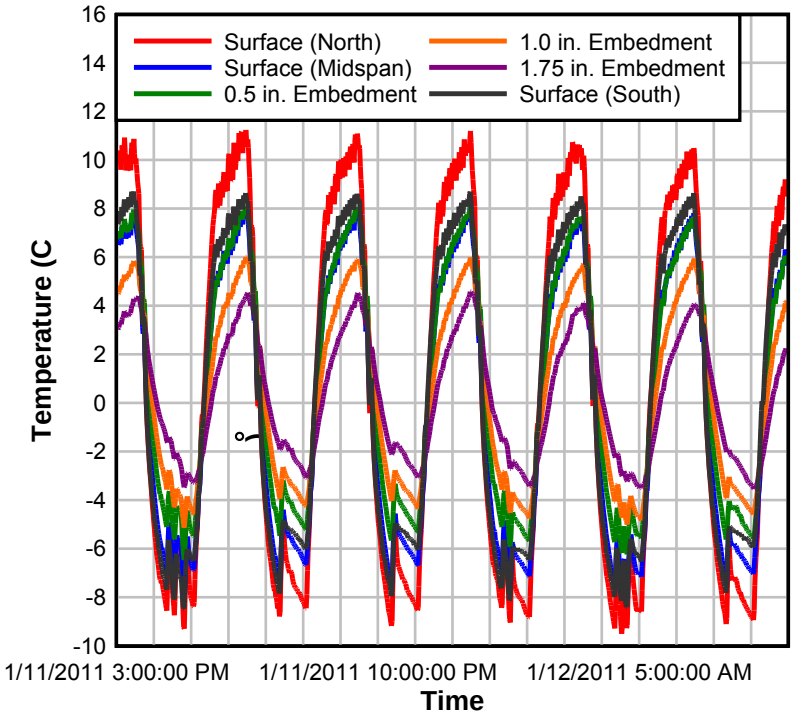

Figure 5.21: Typical temperature measurement data from thermocouples in and on specimen

The number of freeze-thaw cycles was established based on climate data from across Oregon and ASTM standards. Oregon has various climate regions that each experience a different number of freeze-thaw cycles every year. Extreme climates in the eastern part of the state may yield many freeze-thaw cycles yearly while fairly moderate conditions along the coast produce far fewer freeze-thaw cycles. ASTM C 666 prescribes 300 cycles to characterize the freeze-thaw durability of concrete under fully wet freezing and thawing. In order for concrete to be affected by freeze-thaw conditions, water must be available in the concrete to expand. Expanding water present in the voids of a concrete matrix is responsible for freeze-thaw deterioration (*Mehta et al. 2006*). While ASTM C 666 prescribes fully wet thaw cycles, these conditions are not representative of in-situ bridge girders. Under normal conditions, bridge girders will not be submerged in water; they will only be surface saturated. Furthermore, it would not be practical to attempt to submerge a full-size specimen in a laboratory for each thaw cycle within an environmental chamber. As a result, it was decided that the specimen would be surface saturated every eight cycles (once per day) by spraying it with water during a thaw cycle. This method provides free water to penetrate into cracks and promote accelerated deterioration.

Heat transfer analysis was completed on a typical girder stem width of 356 mm (14 in.) during previous research at Oregon State University (*Higgins et al. 2008*). Conduction and convection were considered in the analysis while solar absorption and grey-body irradiation were not considered, because the stem of the girder will typically be shaded by the bridge deck. Climate data was collected from four locations around Oregon that represent high-desert central regions (Tumalo Ridge), the Willamette Valley (Stayton), coast regions (Tillamook), and eastern regions (Sage-Hen). Temperature data was taken from these regions and used as the air temperature surrounding the surface of the girder. In this way, the continuous air temperature records could be converted into a number of freeze-thaw cycles occurring in the girders (considering only freezing at the surface). Typical girder surface and air temperature response for the Stayton site are shown in Figure 5.22 for a year. 5.12 shows the average number of freeze-thaw cycles per year for each region considered as well as the number of years represented by 400 cycles. The Tumalo Ridge and Sage-Hen site experience significantly more freeze-thaw cycles each year. However, these regions are in dry climates, and moisture present when freeze-thaw cycles occur produce more deterioration. Thus the 400 cycle duration considered in this study would most likely be much longer and may represent more equivalent years of exposure in drier climates.

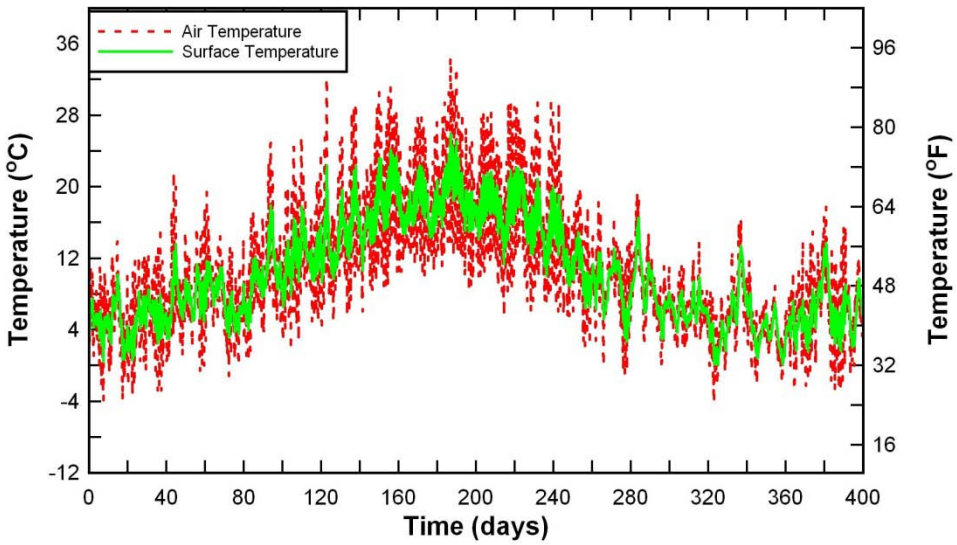

Figure 5.22: Typical surface and air temperature response for Stayton site

Table 5.12: Freeze-thaw cycles for the four regions representative of Oregon *(Higgins et al. 2008)*

Location	Freeze-Thaw Cycles	Period of Temperature Record (Years)	Freeze-Thaw Frequency (Cycles/Year)	400 Cycle Duration (Years)
Tillamook (Coast)	8	11	0.73	548
Stayton (Valley)	45	12	3.75	107
Tumalo Ridge (Central)	243	6	40.5	9.88
Sage Hen (Eastern)	868	22	39.5	10.1

5.10 MOISTURE EXPOSURE PROCESS

After installation of the NSM-CFRP, specimen IT.7.18.6.M was subjected to moisture exposure. To do this, a large tank was constructed outside the laboratory to hold the full-scale specimens for an extended period of time. It was built with wooden walls and a wooden floor and had a rubber liner to make it water tight. The specimen was lifted into the tank with a crane and set on two rubber pads to allow water to flow beneath the specimen. Steel rods were placed to hold the walls together above the level of the specimen and then the tank was filled with municipal water until the specimen was completely submerged as seen in Figure 5.23. The specimen remained in the tank for six months before being removed to test. This time period was chosen to represent a bridge girder during a full wet season in Oregon.

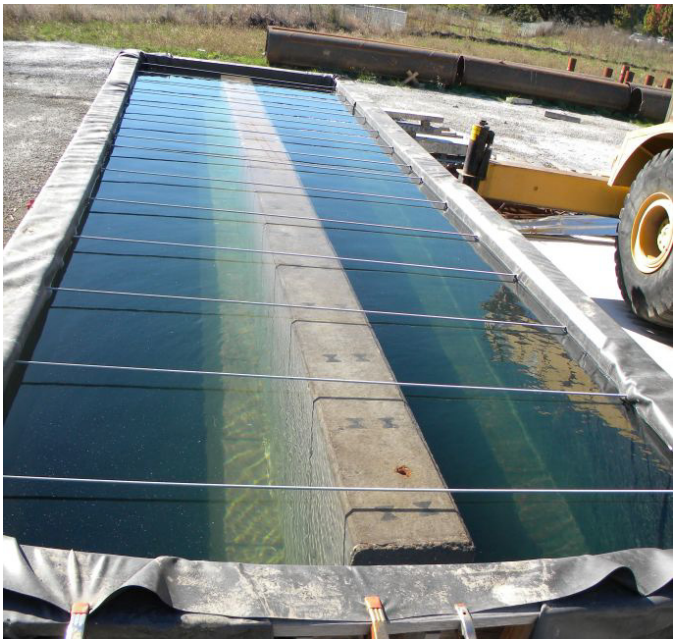

Figure 5.23: Specimen IT.7.18.6.M fully submerged in water tank

6.0 EXPERIMENTAL RESULTS

After precracking the girder specimens, installing the NSM-CFRP and for some specimens, applying fatigue loading, the specimens were tested to failure on the strong floor. The experimental results for each specimen as well as comparisons between specimens are reported in this section. The shear from dead load, V_{DL}, applied shear, V_{App}, and midspan deflections are contained in Table 6.1. The combination of the force applied by the hydraulic actuator and the dead load of the specimen make up the total experimental shear force (V_{EXP}) acting on a specimen at failure. The dead load for each specimen was calculated as the self-weight of the concrete acting on the failure plane assuming the unit weight of reinforced concrete is 23.6 kN/m^3 (150 lb/ft^3). Images of the failed specimens are shown in Figures 6.1 to 6.10. Full data sets for all specimens are contained in Appendix B and crack maps for all specimens are shown in Appendix C. Comparisons of pre-strengthening and post-strengthening midspan displacements are shown in Figures 6.11a to 6.11j. As seen in these figures, no significant global stiffness changes were found between cracked unstrengthened behavior and post-installation of NSM-CFRP. This was expected, because much of the midspan displacement comes from flexural strains that are not significantly impacted by increasing the transverse reinforcement. Descriptions of the specimen responses for each of the tests follow below.

Table 6.1: Key results from strength tests

Specimen	VDL (kN) [kip]	VApp (kN) [kip]	VEXP (kN) [kip]	Midspan Displacement (mm) [in]
T.6.18.6.S	17 [3.9]	992 [223.0]	1009 [226.9]	23.1 [0.91]
T.6.18.12.S	17 [3.9]	1027 [230.6]	1044 [234.5]	19.8 [0.78]
IT.7.18.6.S	18 [4.1]	1192 [267.7]	1210 [271.8]	21.8 [0.86]
IT.7.18.12.S	22 [4.9]	1001 [224.8]	1023 [229.7]	23.6 [0.93]
IT.5.22.12*.S	20 [4.4]	992 [222.9]	1012 [227.3]	24.1 [0.95]
IT.7.22.6.S	21 [4.8]	1143 [257.2]	1164 [262.0]	23.4 [0.92]
IT.7.22.6.FTG	22 [5.0]	1228 [276.1]	1250 [281.1]	24.4 [0.96]
IT.7.22.6.FT/FTG	20 [4.6]	1331 [299.2]	1352 [303.8]	24.9 [0.98]
IT.7.22.6.M	20 [4.4]	1148 [258.1]	1168 [262.5]	24.1 [0.95]
IT.7.22.6.FT	18 [4.0]	1107 [248.9]	1125 [252.9]	22.1 [0.87]

Figure 6.1: Specimen T.6.18.6.S at failure (flexural)

Figure 6.2: Specimen T.6.18.6.S at failure (flexural)

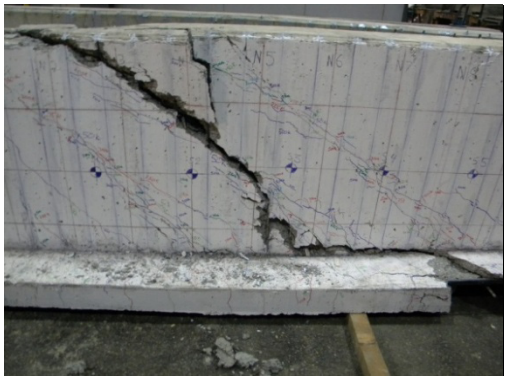

Figure 6.3: Specimen IT.7.18.6.S at failure

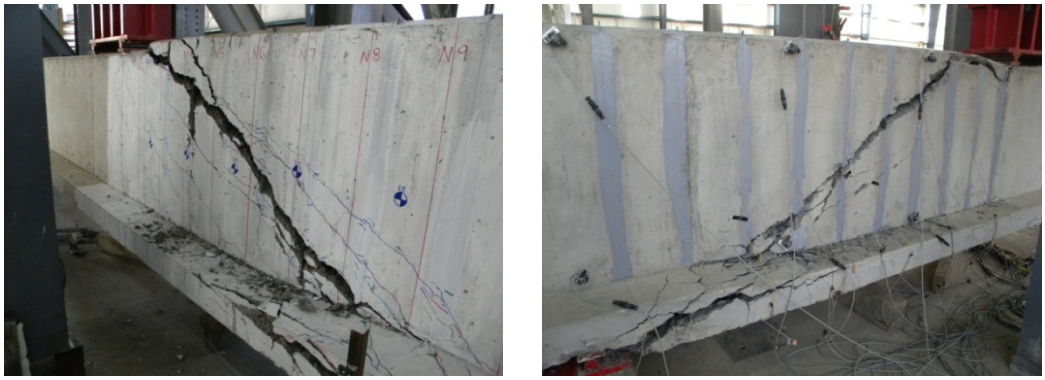

Figure 6.4: Specimen IT.7.18.12.S at failure

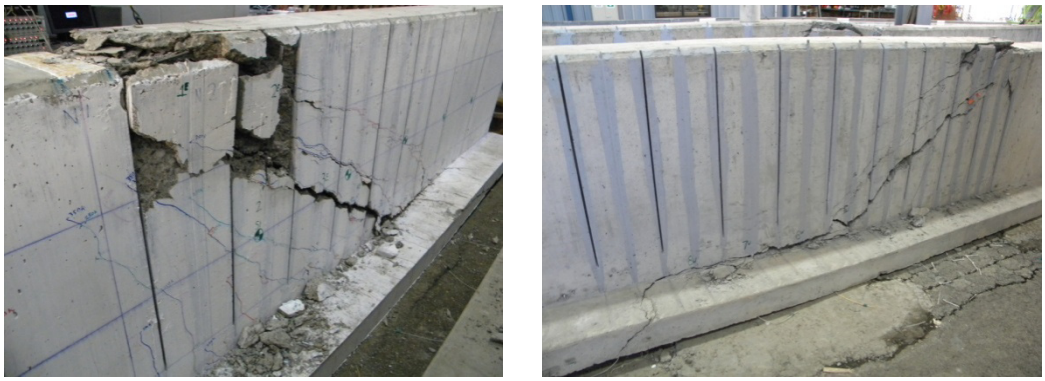

Figure 6.5: Specimen IT.5.22.12*.S at failure

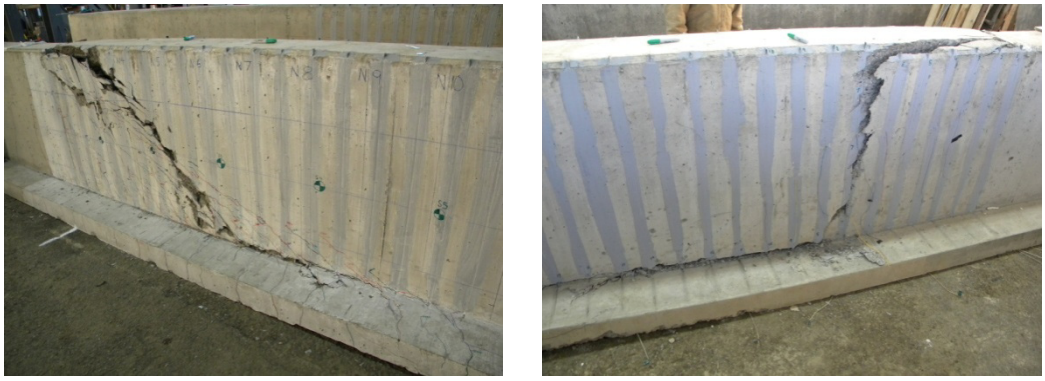

Figure 6.6: Specimen IT.7.22.6.S at failure

Figure 6.7: Specimen IT.7.22.6.FTG at failure

Figure 6.8: Specimen IT.7.22.6.FT/FTG at failure

Figure 6.9: Specimen IT.7.18.6.M failure

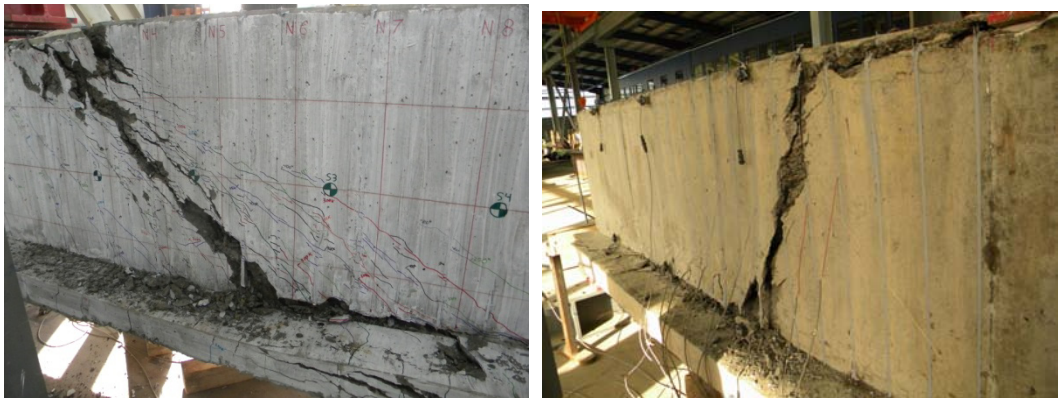

Figure 6.10: Specimen IT.7.22.6.FT failure

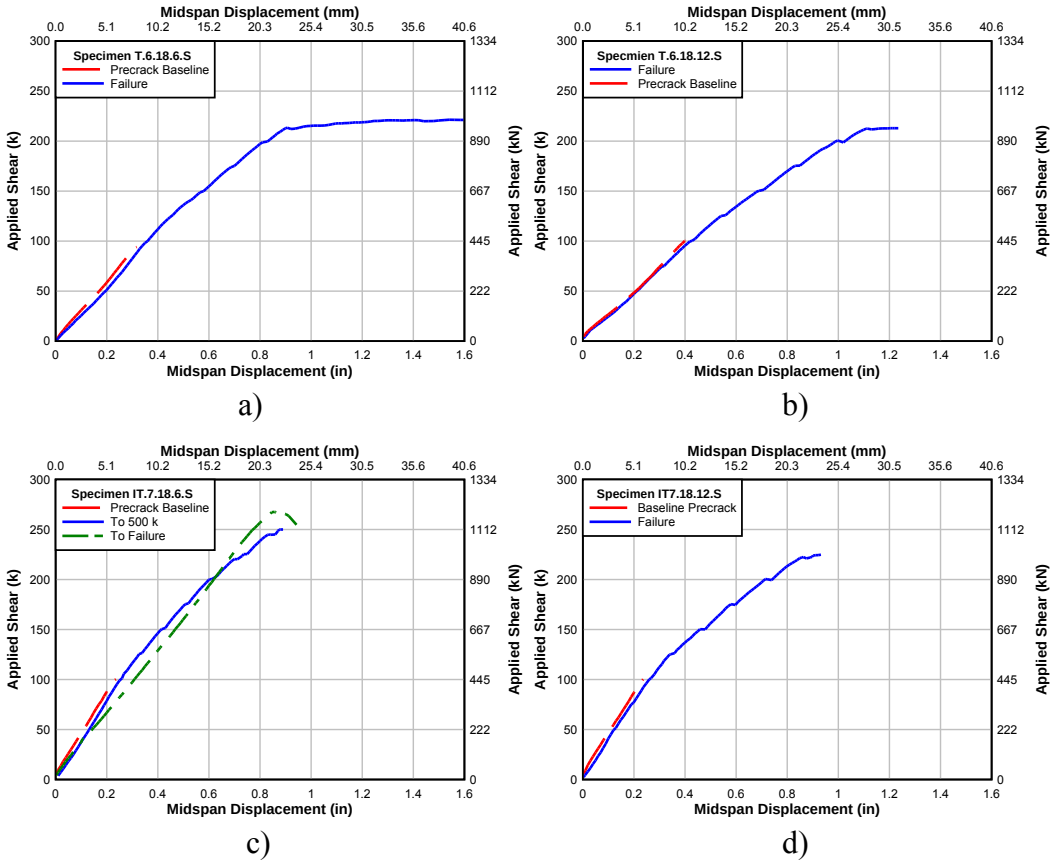

Figure 6.11: Applied shear-midspan displacement response of specimens

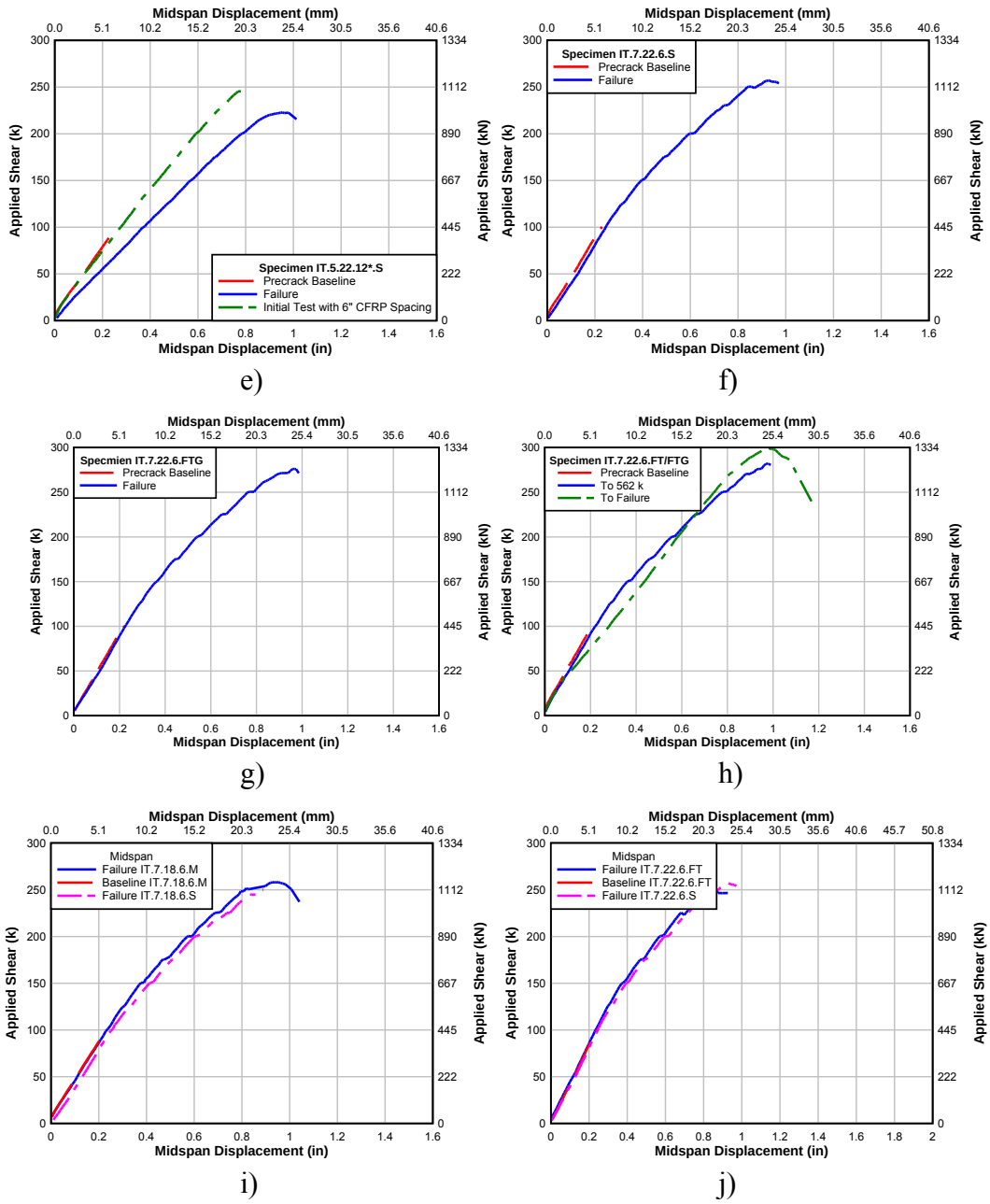

Figure 6.11 (continued): Applied shear-midspan displacement backbone responses of specimens

6.1 SPECIMEN T.6.18.6.S

Specimen T.6.18.6.S failed at an applied load of 1984 kN (446 k). The midspan deflection at the onset of plastic deformation was 23.1 mm (0.91 in.). The specimen then continued to deflect while maintaining load until failure at a deflection of 55.4 mm (2.18 in.). The failure mode was flexure as crushing of the compression block occurred as can be seen in Figure 6.1. Failure occurred before further measures were taken to attempt to induce a shear failure. Later results from specimen T.6.18.12.S clearly demonstrated that a shear failure in specimen T.6.18.6.S was not possible. The flexural failure occurred due to under estimation of the CFRP contribution to

shear strength of the girder specimen that was based on previous research on small size specimens and described in Section 5.2. Specimen designs were made to fail in shear before the flexural capacity of the specimen was reached. However, because the CFRP contribution was under predicted, flexural failures were not always avoided. The actual contribution of the NSM-CFRP for shear strength for specimen T.6.18.6.S could not be determined; however, a minimum contribution was reported.

6.2 SPECIMEN T.6.18.12.S

Similarly to specimen T.6.18.6.S, specimen T.6.18.12.S began to fail in flexure at 1895 kN (426 k). Before the compression zone crushed, the test was stopped and the shear span was reduced to 2997 mm (118 in.). Doing this reduced the moment arm of the test setup allowing additional shear to be applied while reducing the moment applied to the specimen. However, the specimen again began to fail in flexure and the supports were then moved to the location of the most prominent shear crack. Even then, a shear failure was not obtained and the specimen failed in flexure at a load of 2051 kN (461 k). The deflections were 19.8 mm (0.78 in.) at the onset of plastic behavior and 32.8 mm (1.29 in.) at failure. Failure of Specimen T.6.18.12.S is shown in Figure 6.2.

6.3 SPECIMEN IT.7.18.6.S

Specimen IT.7.18.6.S was loaded to 2224kN (500k) before the working pressure of the hydraulic power unit was reached. The pressure was increased and a shear-compression failure was reached at a load of 2380 kN (535 k). In an effort to avoid having to operate the power unit at higher line pressures in future tests, the internal steel stirrup spacing of specimens that had not yet been constructed was increased from 457 mm (18 in.) to 559 mm (22 in.). The east face of the beam exhibited a diagonal crack originating near the load point and continuing to the top of the flange at an angle of approximately 45° measured from the top of the specimen. The crack then continued along the top of the flange for approximately 914 mm (36 in.) before cracking through the flange. The west side of the specimen experienced peeling of the cover concrete outside of the reinforcing steel cage for approximately the first 914 mm (36 in.) from the load point in the upper third of the specimen. A steeper crack angle of approximately 60° was observed on the east side of the specimen. Once the crack reached the top of the flange, it continued along the top of the flange for approximately 762 mm (30 in.) before breaking through the flange. Images of the east and west faces of specimen IT.7.18.6.S are shown in Figure 6.3. Debonding of the NSM-CFRP from the epoxy was observed at several locations namely at the top and bottom of the CFRP strips and at crack locations as shown in Figure 6.12. This type of behavior was typical for most specimens.

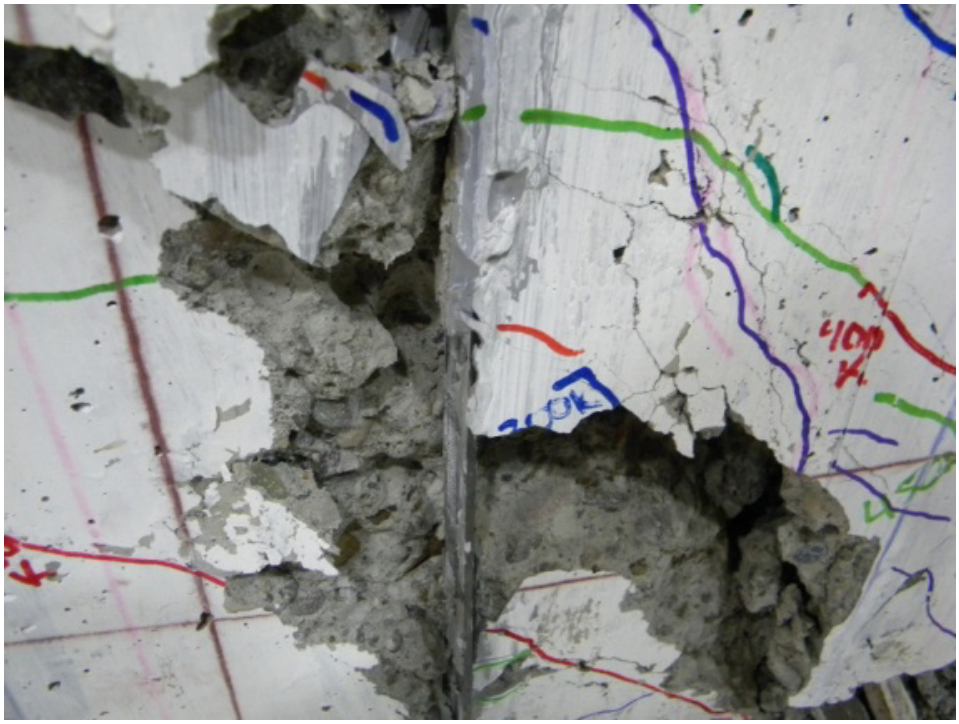

Figure 6.12: Example of debonding of NSM-CFRP

6.4 SPECIMEN IT.7.18.12.S

Specimen IT.7.18.12.S failed in shear-compression at a load of 1979 kN (445 k). A diagonal crack originated on both sides of the specimen approximately 305 mm (12 in.) from the load point and continued to the support at an approximate angle of 28°. The concrete cover above the compression steel appeared to buckle near the load point as shown in Figure 6.13. The CFRP slipped and debonded from the epoxy at the top of the strips around grid lines N3, N4, and N5 and at the bottom of the strips around grid lines N7 and N8. The grid lines are red chalk lines snapped on the specimen that are spaced 304 mm (12 in.) apart. The grid lines are numbered from N1 at the load point to N11 near the support. Debonding was also present at the failure crack. Images of the east and west faces of specimen IT.7.18.12.S are shown in Figure 6.4.

Figure 6.13: Specimen IT.7.18.12.S detachment of concrete cover between grid lines N1 and N3

6.5 SPECIMEN IT.5.18.12*.S

Specimen IT.5.18.12*.S was originally strengthened with CFRP using a 152 mm (6 in.) spacing. When tested, the specimen began to fail in flexure at a load of 2002 kN (450 k). Again, the supports were moved closer in an attempt to achieve a shear failure by reducing the moment. The shear span was reduced by 610 mm (24 in.) and a load of 2184 kN (491 k) was reached before the specimen began to exhibit flexural failure. The supports were moved again to the location of the most prominent shear crack in an effort to induce the most shear force. However, shear failure was not achieved. The decision was then made to remove half of the NSM-CFRP to create a specimen with 305 mm (12 in.) CFRP spacing. The supports were moved back to their original positions and when tested, a shear-compresssion failure was achieved at a load of 1984 kN (446 k). The failing diagonal crack began at the load point and continued to the top of the flange at an approximate angle of 35°. Once the crack reached the flange, the flange appeared to be pulled away from the stem of the specimen beginning at grid line N6 and continuing to grid line N9 where the shear crack continued through the flange. The concrete cover at the top of the stem appeared to be peeled away from the reinforcing cage between the load point and grid line N3. Debonding was present at crack locations as well as at the top and bottoms of CFRP strips. Images of the east and west faces of specimen IT.5.18.12*.S are shown in Figure 6.5.

6.6 SPECIMEN IT.7.22.6.S

Specimen IT.7.22.6.S failed at a load of 2286 kN (514 k) in shear-compression. Each side of the specimen appeared to experience a different failure mode. Similar to other specimens, the east side of the specimen failed along a diagonal crack. Peeling of the cover was observed in the top

305 mm (12 in.) between grid lines N1 and N3. The diagonal crack originated around grid line N3 and continued at an angle of approximately 46° to the top of the flange at grid line N7. The crack then ran along the top of the flange until grid line N9 where it broke through the flange. Debonding was present at crack locations and at the top and bottom of some of the CFRP strips, in particular, the top of the strips between grid lines N4 and N5 where the CFRP was no longer visible at the top of the stem. The east side of the specimen is shown in Figure 6.6. The west side of the specimen failed in a different mode than the east side: predominately through peeling. This failure is shown by an additional green failure crack on the crack map in Figure C-16 (Appendix C). A nearly vertical crack was present at grid line N4 between the top and bottom peeling regions. The concrete cover containing the NSM-CFRP of the top half of the specimen began peeling from the load point and continued until it reached the crack at grid line N4. The bottom half of the concrete cover of the specimen began peeling starting at grid line N4 and continued along the top of the flange until grid line N9. The west side of the specimen is shown in Figure 6.6. The only debonding observed on the west side of the specimen occurred at the CFRP strip near grid line N4 where the vertical crack propagated.

6.7 SPECIMEN IT.7.22.6.FTG

Specimen IT.7.22.6.FTG experienced little change during fatigue cycling. No significant change in midspan or diagonal displacements was observed. The same was true of the flexural reinforcing and stirrup strain ranges. The CFRP reinforcement experienced an increase in strain range over the first 100,000 cycles before leveling off and remaining relatively constant for the remainder of the fatigue cycling. Efflorescence, shown in Figure 6.14, was apparent below the diagonal cracks of the specimen as water was forced out of the cracks during fatigue unloading cycles.

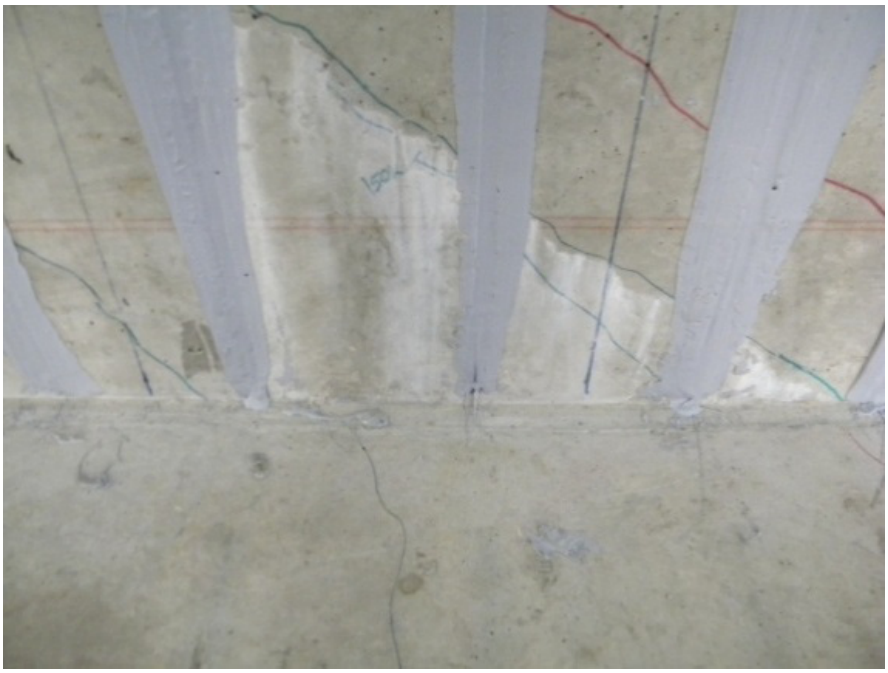

Figure 6.14: Specimen IT.7.22.6.FTG typical efflorescence

The specimen failed at a load of 2500 kN (562 k) and exhibited a shear-compression failure mode. The diagonal failure crack propagated near the loading point between grid lines N1 and N2 and continued to grid line N6 at an approximate angle of 35°. The crack then continued along the top of the flange through grid line N10. Images of the east and west faces of specimen IT.7.22.6.FTG are shown in Figure6.7. Peeling of the concrete cover was observed above the failure crack between grid lines N1 and N3 on both faces of the specimen. Debonding and slippage were observed at failure crack locations as well as at the top and bottom of several CFRP strips. Diagonal cracks crossing the CFRP reinforcing exhibited significant feathering indicating localized stress transfer between the CFRP strips, epoxy, and concrete substrate at the crack locations. Example of crack feathering is shown in Figure 6.15. While some degree of feathering was seen on all specimens, significantly more feathering was observed in Specimen IT.7.22.6.FTG.

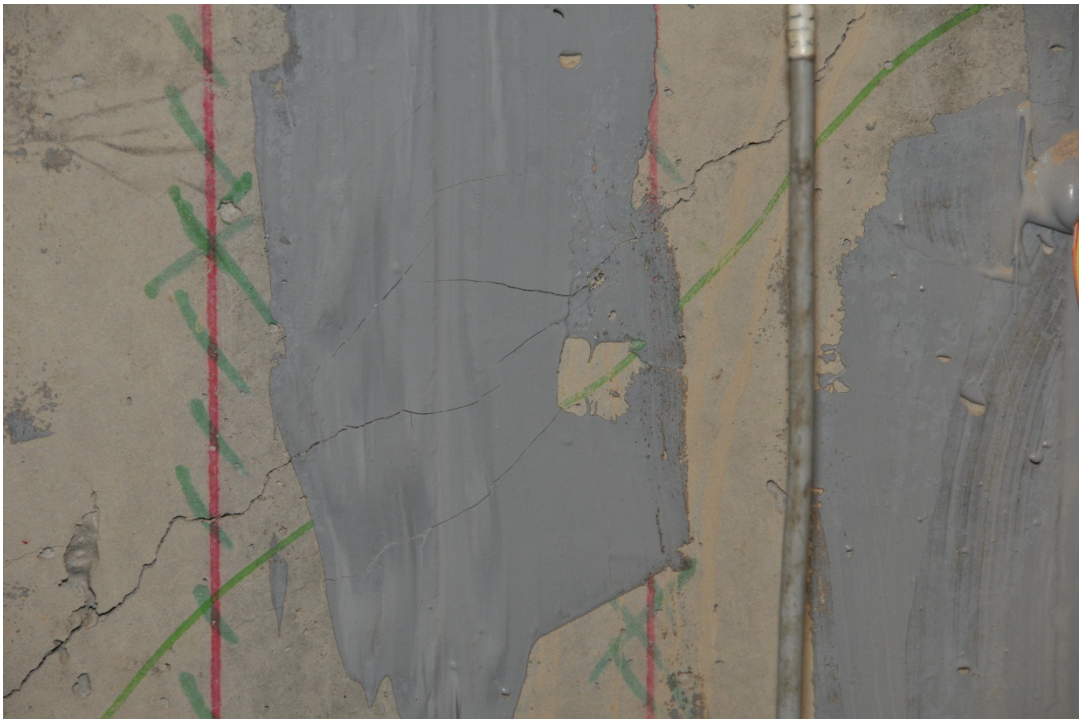

Figure 6.15: Example of crack feathering at NSM locations

6.8 SPECIMEN IT.7.22.6.FT/FTG

Due to the extremely harsh environmental conditions of IT.7.22.6.FT/FTG during fatigue cycling, the quality of the fatigue data was not as good as that obtained in the other tests. In some testing intervals, useful data were obtained. Midspan deflections exhibited a declining trend for the first 800,000 cycles and remained relatively consistent thereafter. No significant change was observed in diagonal displacements. No useful data regarding flexural and stirrup reinforcing was able to be obtained during fatigue cycling as water was believed to have shorted the electrical connections to the sensors and wire contacts. CFRP strain ranges trended

downward for the first 400,000 cycles before remaining relatively constant for the remainder of the fatigue cycling. This decline in strain range can in part be attributed to raveling of the concrete at crack locations due to the effects of freeze-thaw. When exposed to freeze-thaw conditions, the concrete around crack locations began to break down and flake off. This concrete debris fell into the diagonal cracks and prevented the cracks from completely closing when the load was removed. As a result, the CFRP did not experience the full strain range on unloading that would be present without raveling. Typical raveling along a crack is shown in Figure 6.16.

Figure 6.16: Specimen IT.7.22.6.FT/FTG typical raveling along a diagonal crack, scaling of concrete on flange soffit, and associated debris

During failure testing, Specimen IT.7.22.6.FT/FTG was loaded to 2509 kN (564 k) at which point the pump reached its maximum capacity. In an effort to apply additional load, a 1334 kN (300 kip) capacity hollow core cylinder jack with a 890 kN (200 kip) capacity load cell was added to the test setup. Load was applied using a 68.9 MPa (10,000 psi) hand pump.

The specimen failed at an applied shear load of 1351 kN (304 k). Peeling of the concrete skin was observed at the top of the stem between grid lines N1 and N3. The diagonal failure crack began propagating just south of grid line N3 and continued to grid line N5 at an approximate angle of 58°. The failure crack then continued along the top of the flange through grid line N9. Peeling of the concrete cover was also observed along the top of the flange at the failure crack. Typical debonding was present at crack locations and at the top and bottom of CFRP strips.

A single CFRP strip was ruptured at the failure crack near grid line N3 on the west face of the specimen. The CFRP rupture is shown in Figure 6.17. Images of the east and west faces of specimen T.7.22.6.FT/FTG are shown in Figure 6.8.

Figure 6.17: IT.7.22.6.FT/FTG CFRP rupture

6.9 IT.7.18.6.M

This specimen was the same as IT.7.18.6.S except it was submerged in water for six months before it was tested for shear capacity. The only visible effect of the moisture exposure was some rust spots on the flange and on the top of the stem where the exposed steel reinforcing chairs had formed rust. As the specimen was tested, damp areas formed on the specimen's surface as water was squeezed out from the induced stress. The specimen failed in shear similar to the other specimens at a load of 2295 kN (516 kips). Images of the east and west faces of specimen T.7.18.6M are shown in Figure 6.9. At the 2224 kN (500 kip) load step, just prior to the specimen's failure, two areas of debonded concrete were visible at the bottom of the stem. An example of this is shown in Figure 6.18. These debonding regions are the beginning of the peeling failure mode observed in most of these specimens. The failure crack ran from the load point behind the CFRP for about 61 cm (24 in.) on both sides of the specimen and then cracked at a steep 60° angle down to the top of the flange. The failure plane then ran along the stem and flange junction to the support. At the top and bottom of the diagonal crack it appears the outer shell of NSM reinforced concrete peeled away from the inner core of concrete. Some of the ends of the CFRP strips had also visibly debonded from the specimen during the failure. The ends of these strips had regions with epoxy still bonded and regions of bare carbon fiber; this implied debonding occurred both by CFRP strips pulling out of the epoxy and from the concrete breaking around the NSM epoxy. The broken concrete was visibly darker than other specimens due to its moisture saturation.

Figure 6.18: Specimen IT.7.18.6.M initial peeling and saturated concrete vs. dry concrete

6.10 IT.7.22.6.FT

The specimen was subjected to 400 freeze-thaw cycles before being tested for shear capacity. The most obvious freeze-thaw damage was scaling of concrete on the specimen flange. This was primarily where water was sitting and would not have occurred if the specimen was in the T-orientation. There were also two small areas of debonded surface concrete on the web. Examples of freeze-thaw damage are shown in Figure 6.19.

Figure 6.19: Specimen IT.7.22.6.FT effects from freeze-thaw exposure

This specimen was constructed with the same details as IT.7.22.6.S, which was the control for this specimen. It failed in shear at 2211 kN (497 kips) of load. Images of the east and west faces of specimen T.7.18.6FT are shown in Figure 6.10. The east side of the specimen failed diagonally from the edge of the load plate to the top of the flange at an angle of 45°. It then cracked horizontally along the stem junction for 54 cm (25 in.) and diagonally through the flange. The west side broke behind the NSM retrofit for the 51 cm (24 in.) next to the load plate. It then cracked at a steeper 70° angle down to the flange and then horizontally along the flange and stem junction. Slippage of the top of the CFRP strips was observed in the 3rd, 4th, and 5th strips from the load point on the east side of the specimen. On the west side, only the 5th CFRP

strip showed signs of slippage. The bottom of one strip on each side exhibited debonding of the concrete around the epoxy. Additionally, one strip on the west side appeared to have ruptured in tension as seen in Figure 6.20. There was a clean fracture with no signs of slippage at either end of the CFRP that would have caused bending, and this was the only example of such a rupture in the program.

Figure 6.20: Rupture of CFRP strip without slip relative to surrounding epoxy or concrete

6.11 SPECIMEN STIFFNESS

In order to determine the serviceability performance of girders strengthened with NSM-CFRP, the stiffness behavior of the specimens was investigated. Local shear stiffness changes were also of interest in this study. Local shear stiffnesses were determined by computing average vertical strains in the specimens calculated from the diagonal displacement sensors. Diagonal displacements were converted to vertical strain using Mohr's circle for strain following the procedure described by Dawson (*2008*). The specimens were separated into three panels with panel 1 located nearest the support, panel 2 in the middle of the shear span, and panel 3 nearest the load point. Panel 1 is not shown as relatively minimal diagonal cracking occurred in this panel due to its proximity to the support. After specimens experienced initial cracking, a certain amount of load was needed to be applied before the diagonal cracks in the specimen would open. This decompression loading remained relatively constant over each loading cycle. Decompression loads varied for each specimen with precrack baseline and failure decompression loads ranging from 17.8 kN (4 k) to 605 kN (136 k) and 17.8 kN (4 k) to 739 kN (116 k) respectively. Pre-strengthening and post-strengthening vertical strain behavior for panels 2 and 3 are shown in Figures 6.21a to 6.21j and 6.22a to 6.22j.

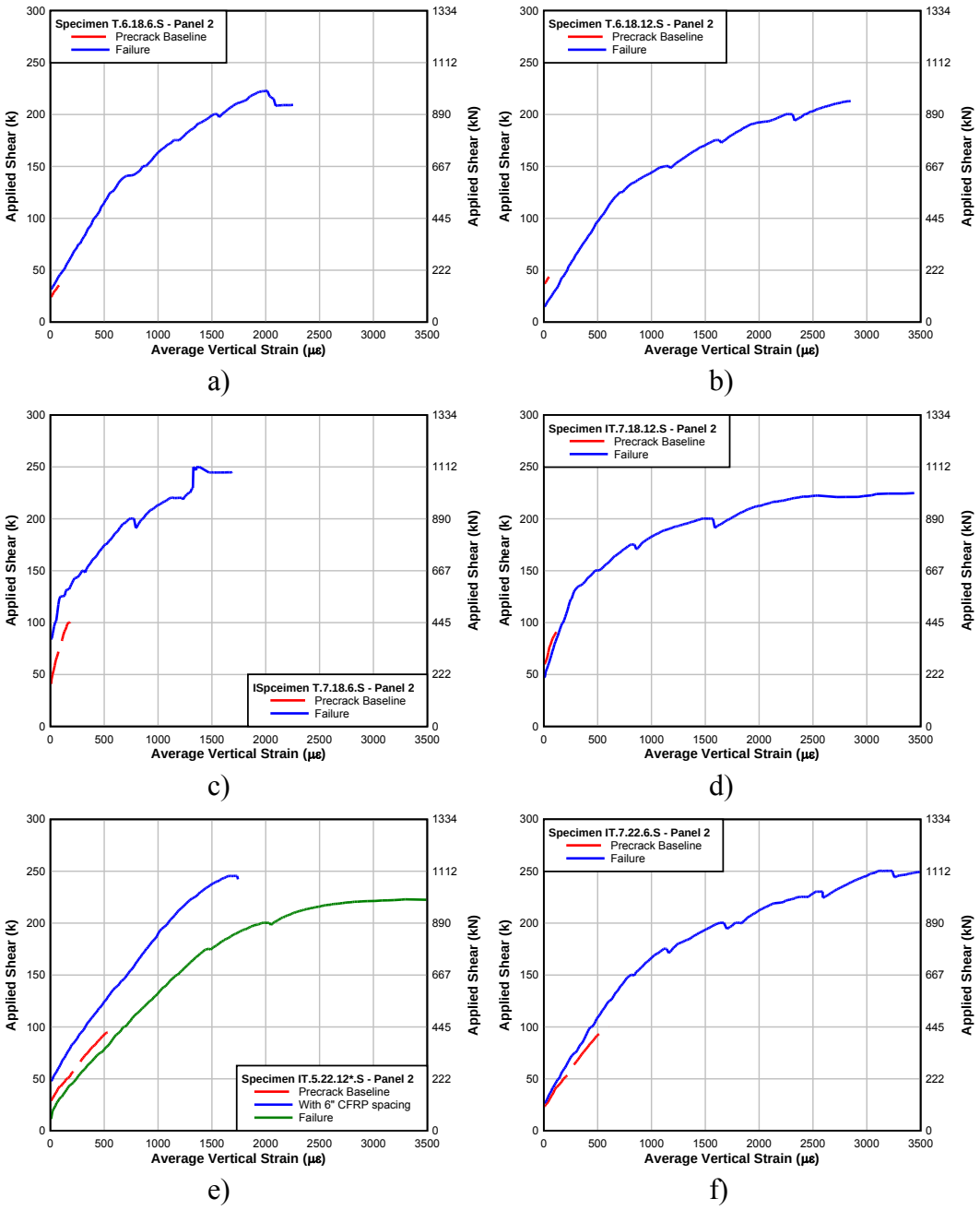

Figure 6.21: Shear panel 2 stiffness comparison of strength specimens

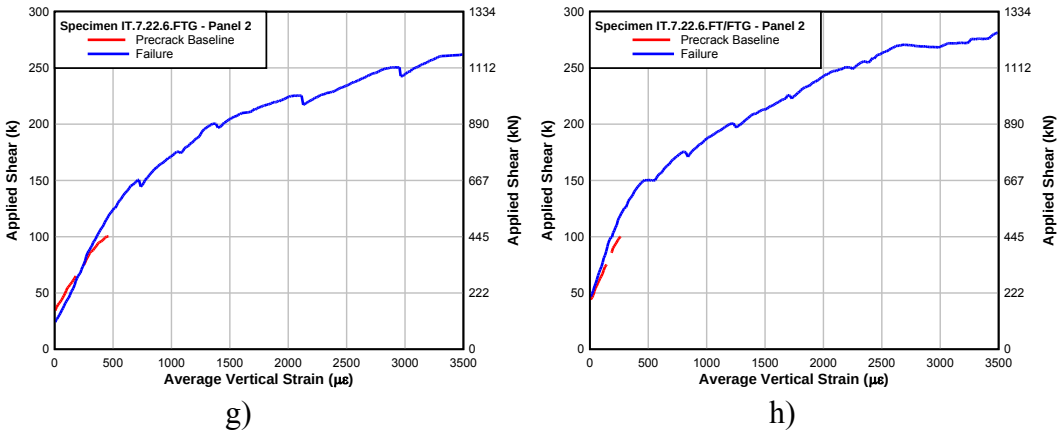

g)

h)

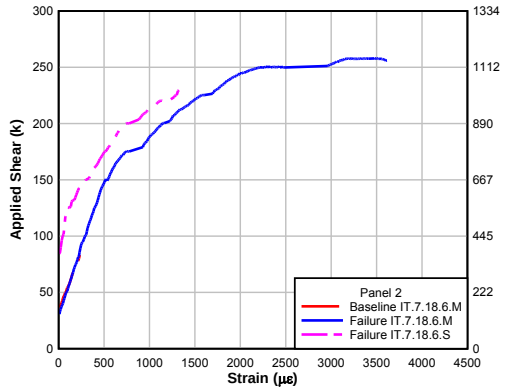

i)

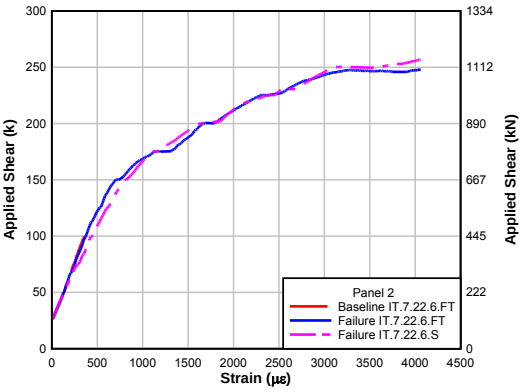

j)

Figure 6.21 (continued): Backbone shear panel 2 stiffness of specimens

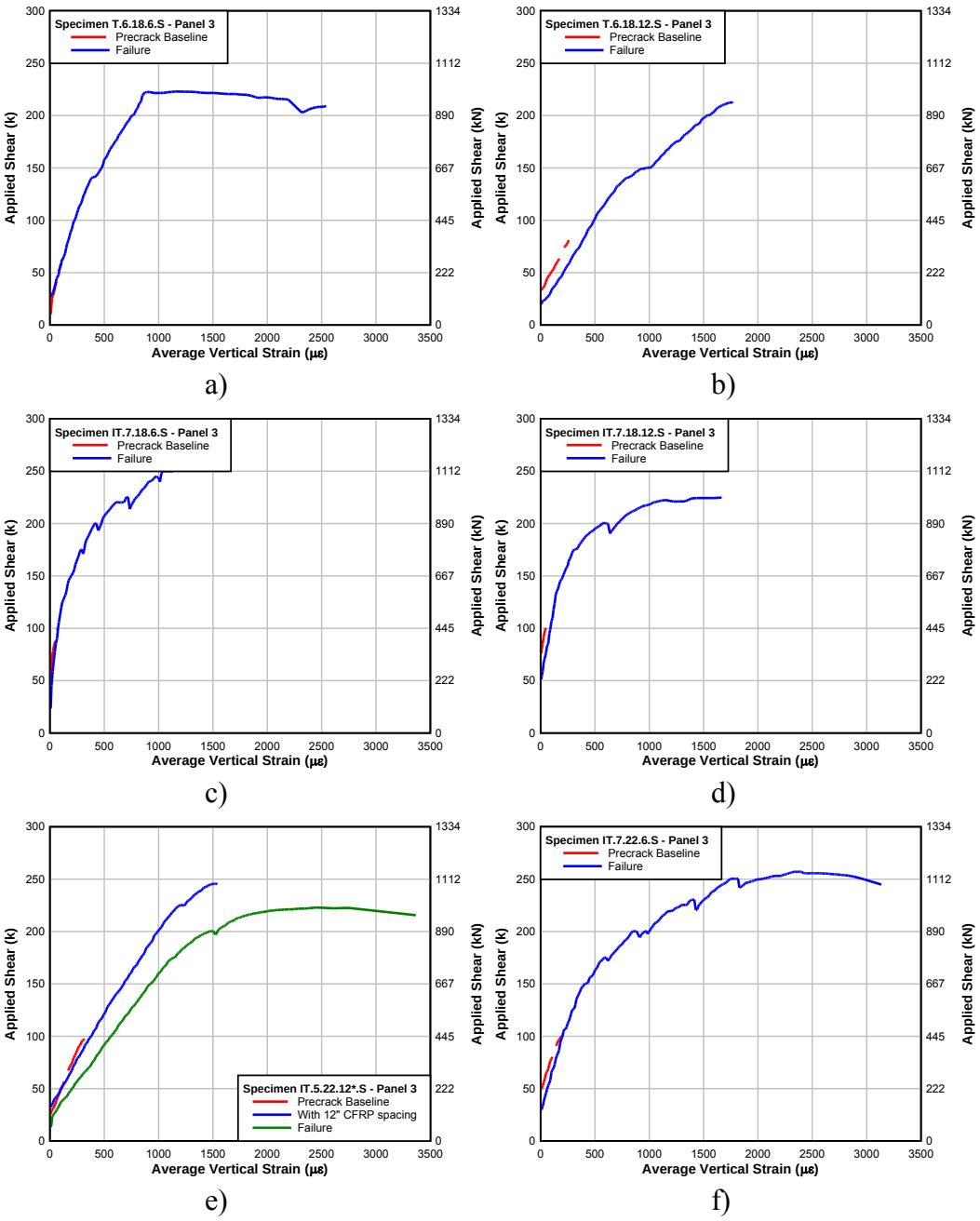

Figure 6.22: Backbone shear panel 3 stiffness of specimens

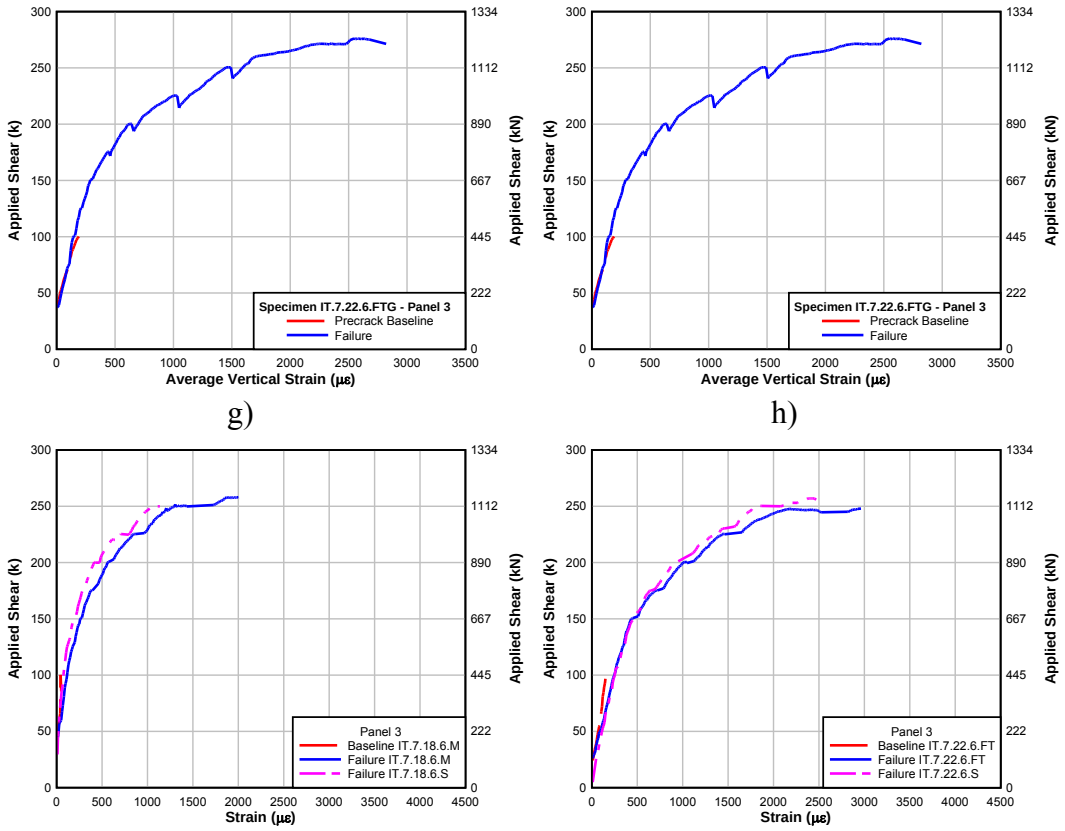

Figure 6.22 (continued): Backbone shear panel 3 stiffness of specimens

6.12 STIRRUP STRAINS

Application of NSM-CFRP was expected to reduce stresses in the underlying steel stirrups at similar load levels for the base specimen without NSM-CFRP. Stresses were established from measured strains on the steel stirrups. These were examined to see if application of NSM-CFRP reduced the stress range in the steel stirrups. The stirrup strain range produced during loading up to 890 kN (200 kip) from the baseline data was compared to the same stirrup strain range up to 890 kN (200 kip) load after application of NSM-CFRP. The steel stirrup strain gages were placed at midheight. Consequently, they did not always provide useful data because they were not always near a diagonal crack. All the steel stirrups were examined, but only the stirrups reading a strain range of over 500 microstrain during the baseline test were considered. The strain ranges for the stirrups being compared are shown in Figure 6.23. For all of the internal steel stirrups examined, they displayed a reduction in strain after NSM-CFRP application.

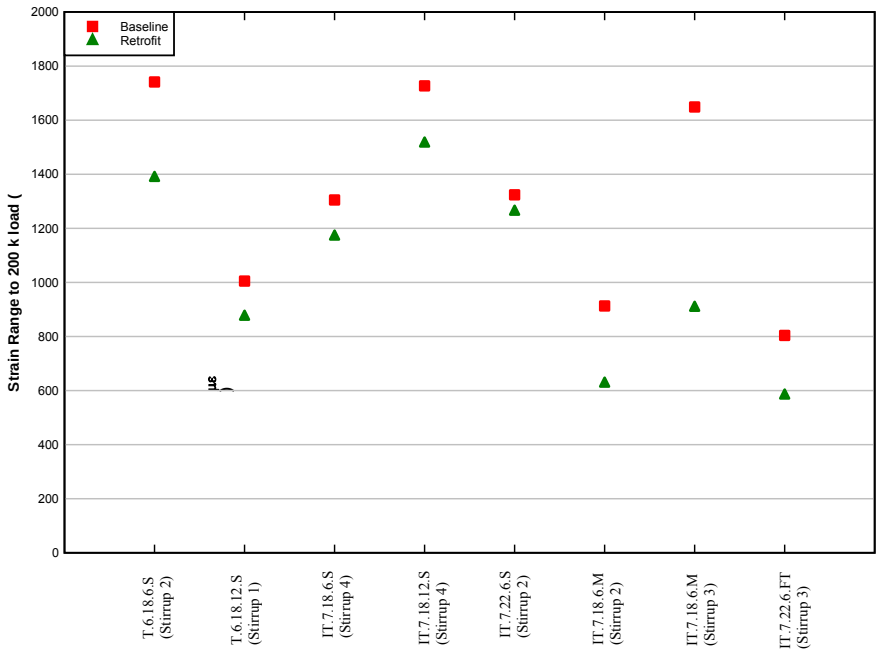

Figure 6.23: Pre-strengthened stirrup strain range vs. retrofitted stirrup strain range

6.13 EFFECTS OF ENVIRONMENTAL EXPOSURE

The measured shear strengths of the reference and environmentally exposed specimens are shown in Table 6.2. Comparing the environmentally exposed specimens to their respective control specimens showed small and insignificant reduction in shear capacity. Both the moisture and freeze-thaw exposed specimens showed a decrease in shear capacity of 3.4%. This was likely in the range of material and behavioral variability.

Table 6.2: Shear capacities after environmental exposure compared to controls

Specimen	VEXP	
	[kN]	[kips]
IT.7.18.6.S	1209	271.8
IT.7.18.6.M	1168	262.5
IT. 7.22.6.S	1165	262.0
IT.7.22.6.FT	1125	252.9

Changes in the stiffness of the environmentally exposed specimens were examined in order to identify the impact of freeze-thaw effects on performance. The global stiffness of the member was considered at midspan as shown in Figures 6.24a and b and along the three diagonally instrumented shear panels. The diagonal deformations were converted to average vertical strains based on Mohr's circle and the specimen responses are shown below in Figures 6.24c-6.24f. The stiffness of the retrofit failure curves are compared to their baseline curves and to the failure curves of the control specimens. No significant changes in stiffness are noticeable from the comparisons. This is reasonable because there were no apparent increases in stiffness due to the

NSM retrofitting and thus any degradation of the NSM reinforcing due to environmental exposure would not impact the stiffness.

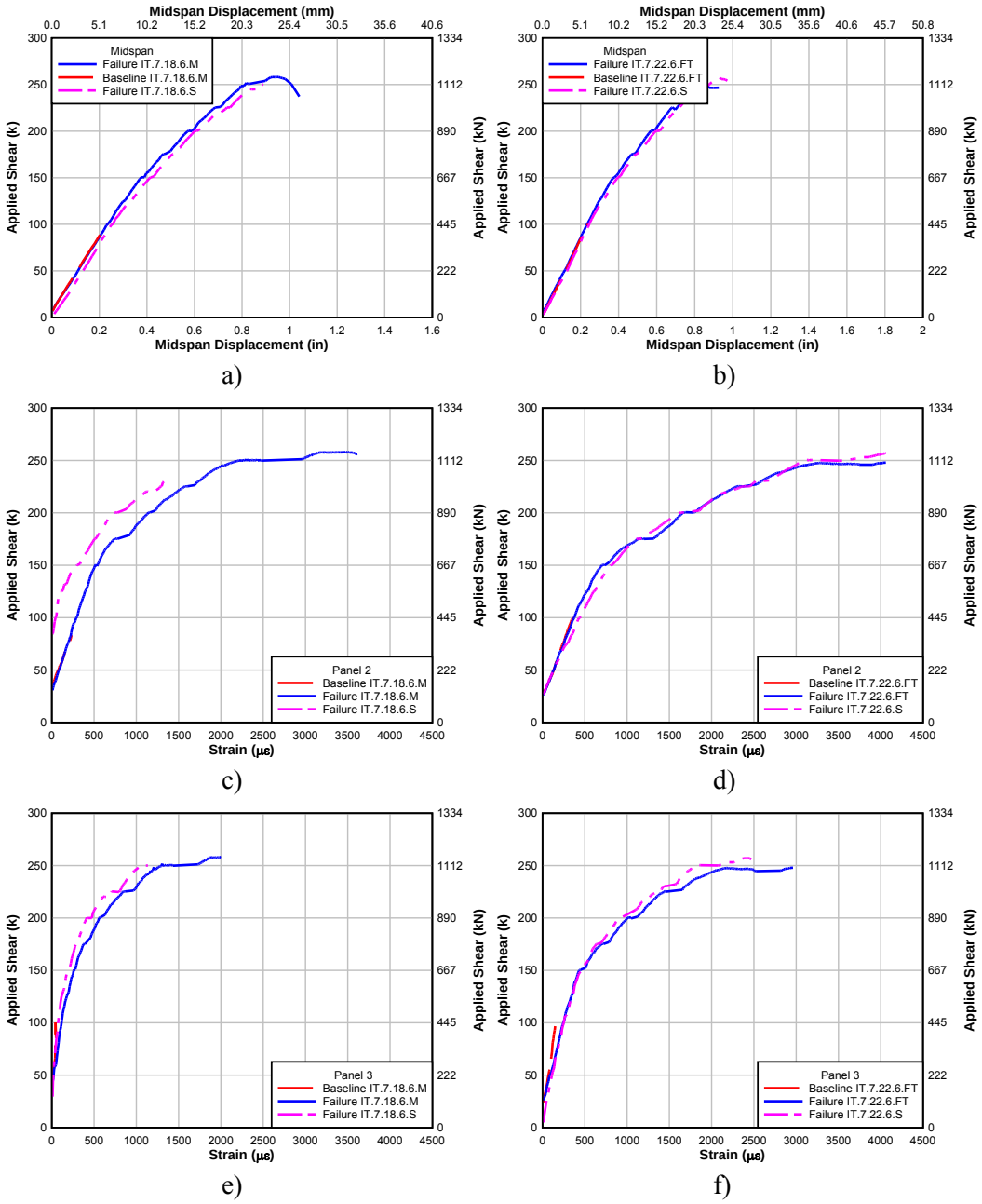

Figure 6.24: Overall and local stiffnesses of environmentally exposed specimens with comparable unexposed control specimens

6.14 EFFECTS OF FATIGUE CYCLING

Changes in behavior between control and fatigue specimens were studied to determine the effects of fatigue and combined fatigue and freeze-thaw on the long-term performance of NSM-CFRP. Because previous research (*Higgins et al. 2007*) has indicated that there is insignificant change in stirrup behavior or ultimate shear capacity within the range of fatigue loading considered for this experiment, changes in behavior between control and fatigue specimens would be a result of degradation in the NSM-CFRP bond. Results indicated no loss in shear capacity as a result of fatigue or combined fatigue and freeze-thaw effects. The shear capacities of the specimens exposed to fatigue loading were actually higher than the control specimen. This was partly attributed to a higher concrete strength at test day. Due to the length of the fatigue and freeze-thaw exposure, specimens IT.7.22.6.FTG and IT.7.22.6.FT/FTG were tested 169 and 181 days after casting respectively compared to only 56 days for Specimen IT.7.22.6.S. Because a primary failure mode of these specimens was peeling failures through the concrete, the concrete strength at failure can greatly influence the shear strength of the specimens and may be responsible for the apparent increase in strength in the fatigued specimens. Midspan displacements and vertical strains were compared to detect any global or local stiffness changes between specimens as shown in Figures 6.25 and 6.26, respectively. Results indicated no significant changes in global or local stiffness after fatigue and combined fatigue and freeze-thaw effects.

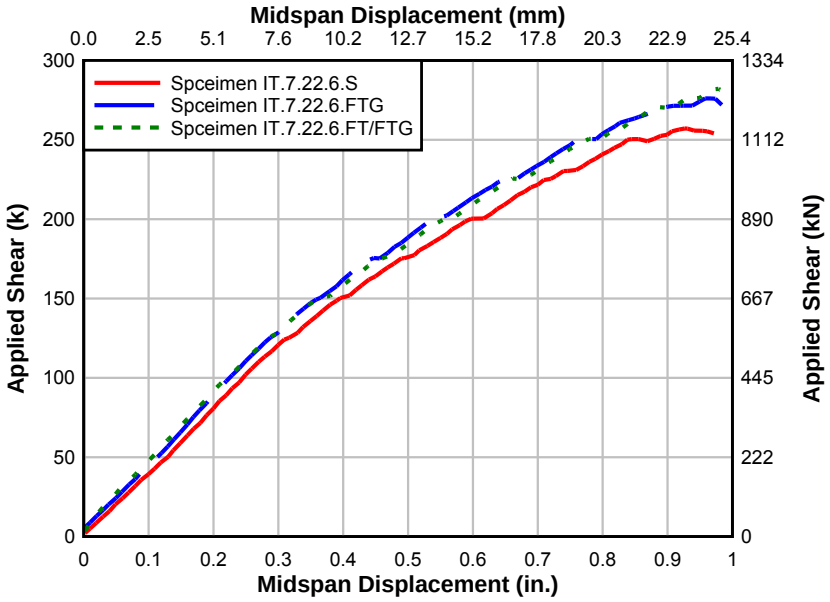

Figure 6.25: Strength and fatigue specimen global stiffness

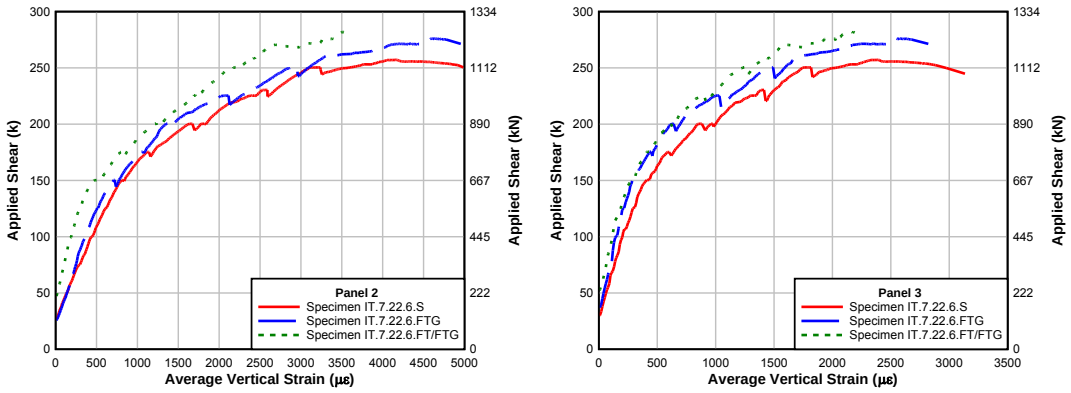

a) b)

Figure 6.26: Strength and fatigue specimen panel stiffness

Data were also collected during fatigue loading in an effort to monitor specimen behavior. The extremely harsh environmental conditions for Specimen IT.7.22.6.FT/FTG adversely affected the sensors for this specimen. As a result, useful data were not obtained for some sensors during the combined freeze-thaw and fatigue loading. Also, raveling of cracks was observed in the combined freeze-thaw and fatigue specimen. As a result of raveling and the associated debris falling into the cracks, diagonal cracks were not able to fully close when load was removed from the specimens. Raveling may have led to unrealistic displacement readings as cracks did not begin to open until after much larger load was applied to overcome the decompression force generated by raveling. The behavior of the fatigue specimens are shown in Appendix B. Results from the fatigue loading indicated no significant changes in displacement or strains for Specimen IT.7.22.6.FTG. Specimen IT.22.6.FT/FTG showed reduction in midspan displacement and CFRP strain range over the first 800,000 and 500,000 cycles respectively. This could in part be attributed to the material falling into the diagonal cracks.

The strains of the highest strained CFRP strip for each fatigue specimen were compared to the control specimen to determine if fatigue or combined freeze-thaw and fatigue loading conditions affected the stiffness of the CFRP/epoxy system. As shown in Figure 6.27, the strains were smaller in the fatigue and combined fatigue with freeze-thaw specimens. The vertical portion of the line representing Specimen IT.7.22.6 FT/FTG (exposed to combined fatigue and freeze-thaw) highlights the effects of raveling and debris entering the diagonal cracks and thereby requiring a larger applied force prior to decompression of the crack faces before the development of additional strains or deflections.

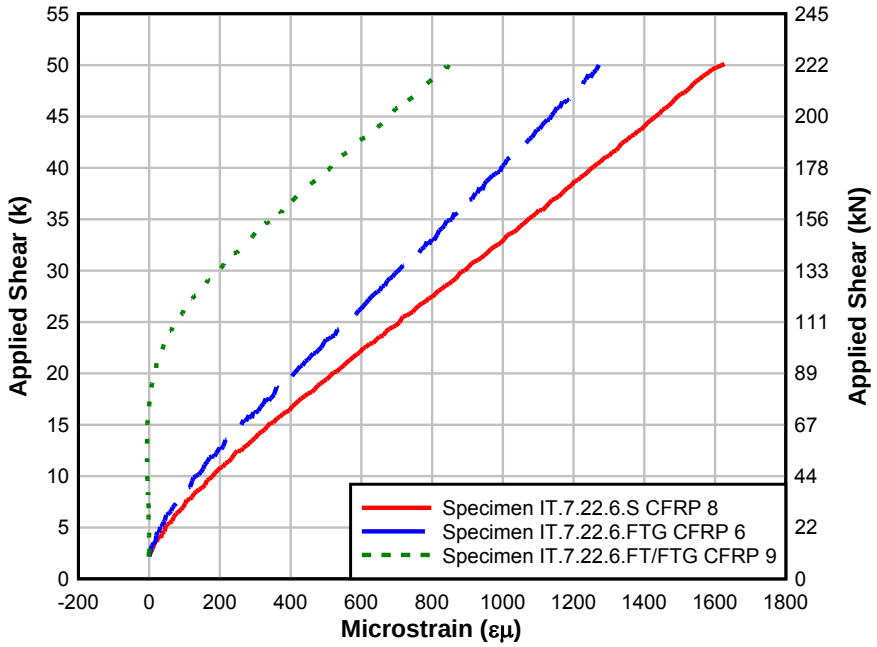

Figure 6.27: CFRP strain comparisons

6.15 EFFECTS OF FLEXURAL STEEL ON TRANSVERSE RESPONSES

Modified Compression Field Theory (MCFT), which was one of the principal methods used in this study for analytical comparisons, includes the influence of the flexural reinforcing on shear capacity. The ACI approach to shear design does not incorporate flexural reinforcing details into shear capacity. The actual effects of flexural reinforcing can be investigated by comparing specimen IT.7.22.6.S to IT.5.22.12.S. It is important to remember that specimen IT.5.22.12.S started as IT.5.22.6.S, and the responses of this initial test will be referred to as IT.5.22.6.S. The responses of these two specimens can be directly compared because concrete strength and flexural steel are the only differences.

6.15.1 Diagonal Deformation Comparisons

For a similar increase in shear, MCFT would predict higher transverse stress and strain in the specimen with less flexural reinforcing. The diagonal displacements provided a representation for the average strain in a shear panel. It was reasonable to compare the diagonal displacements of the two specimens because the crack patterns were similar. As shown in the diagonal displacements in Figure 6.28, specimen IT.5.22.6.S displayed larger strains throughout the loading process, even as the transverse reinforcing details were the same.

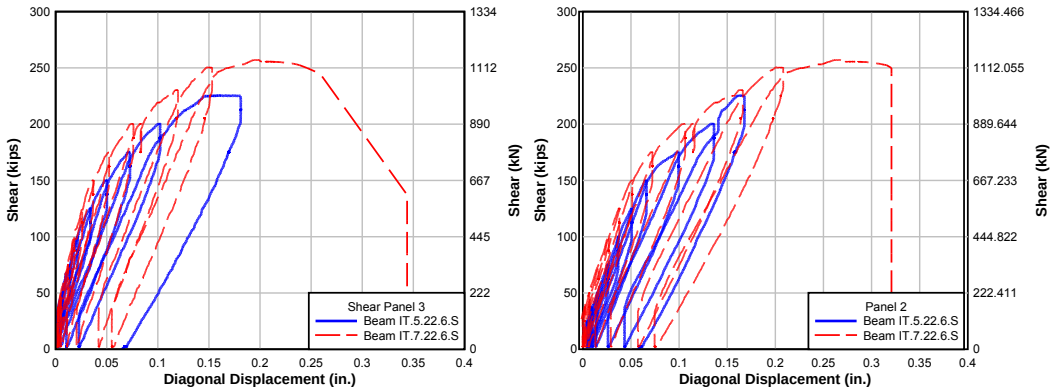

Figure 6.28: Diagonal displacements of IT.7.22.6.S vs. IT.5.22.6.S

To examine this further, the ratio of displacement values from these graphs are reported in Table 6.3 for corresponding applied shear loads. Two R2k models were created to represent the specimens. Additional steel stirrups were added to the models to represent the additional NSM-CFRP. These R2k models were analyzed and the transverse strain was integrated over the cross section at the same shear loads for both specimens. The ratio of the R2k predicted transverse strains are also shown in Table 6.3. It is noticeable that the ratio from R2k is slightly larger than the experimental data. This is reasonable because the specimen with less flexural reinforcing should experience more flexural displacements, and some of these are acquired by the diagonal displacement sensors.

Table 6.3: R2k estimated vs. diagonal displacements data of IT.7.22.6.S/IT.5.22.6.S

Shear Load		Panel 2 Data	Panel 3 Data	R2k value
[kN]	[kips]	IT.7.22.6.S/ IT.5.22.6.S	IT.7.22.6.S/ IT.5.22.6.S	IT.7.22.6.S/ IT.5.22.6.S
556	125	0.78	0.77	0.84
667	150	0.81	0.74	0.86
778	175	0.74	0.74	0.87

6.15.2 CFRP Strain Comparison

The same phenomenon of higher transverse strains in the specimen with less flexural reinforcing can also be examined in the CFRP strips. This is difficult to do because the sensors on the strips are point specific and sensitive to the proximity and motions of the crossing diagonal cracks. To make a meaningful comparison, the CFRP sensors need to be at the same location in both specimens. By overlaying the specimen crack maps (Figures 6.29 and 6.30), it was determined that sensors C4, C6, and C7 in IT.7.22.6.S were located in approximately the same locations as sensors C4, C8, and C9 in specimen IT.5.22.6.S, respectively. Strains are reported in the CFRP strips for corresponding applied shear forces at similar locations in Table 6.4. Comparing the data in the two specimens showed that the CFRP strains in specimen IT.5.22.6.S were consistently higher in two of the sensor locations and approximately the same in the third.

Table 6.4: Strain comparison between CFRP strips in similar locations

Shear Load		CFRP Strain		CFRP Strain		CFRP Strain	
[kN]	[kips]	IT.7.22.6.S CFRP (4)	IT.5.22.6.S CFRP (4)	IT.7.22.6.S CFRP (6)	IT.5.22.6.S CFRP (8)	IT.7.22.6.S CFRP (7)	IT.5.22.6.S CFRP (9)
222	50	401	1447	1245	2201	1678	1628
334	75	874	2334	1938	3437	2798	2619
445	100	1457	3381	2957	4459	3764	3525
556	125	1928	4458	3835	*	4528	4674
667	150	2434	*	4583	*	*	*
778	175	3009	*	*	*	*	*

- Out of sensor range

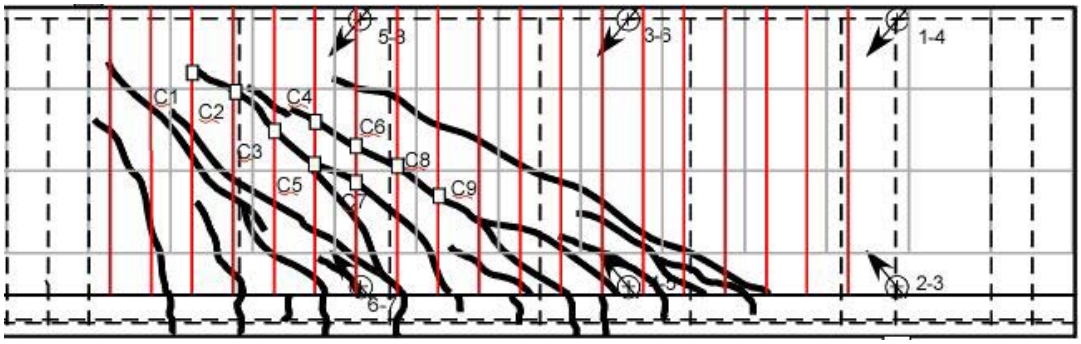

Figure 6.29: Specimen IT.5.22.6.S

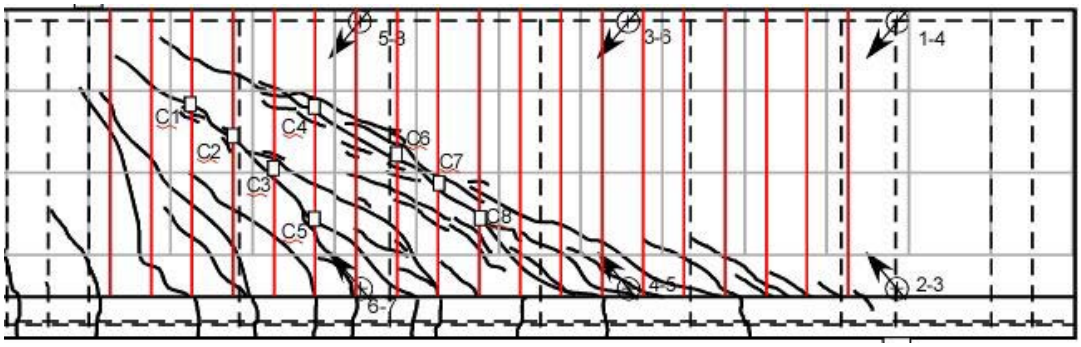

Figure 6.30: Specimen IT.7.22.6.S

6.16 SPECIMEN ORIENTATION

One of the goals of this research was to examine the behavior of T-shaped specimens compared to IT-shaped specimens, which would represent retrofitting in the positive and negative moment regions of a bridge girder, respectively. All the IT specimens failed in shear, but the T specimens both failed in flexure. As a result, the strength gains could not be compared directly because the gains exhibited by the T specimens were not attributed to shear strength.

The shear capacities for the specimens in this research were predicted to be less than the flexural capacities, but the achieved shear strength gains were higher than anticipated and caused more

demand in the flexural reinforcing. The flexural failures only occurred in the T specimens because the baseline strength of the T specimens were higher up on the R2k curve, which placed them closer to the flexurally dominated region.

Another possibility is that the NSM reinforcing was better anchored in the T specimens because it could extend below the flexural reinforcing and lead to higher shear strength gains. The NSM reinforcing in the IT specimens was blocked from reaching the bottom of the specimens by the presence of the deck.

The results of the T specimen tests demonstrated the importance of the base specimen location on the MCFT curve. If a bridge girder is weak in flexural reinforcing, the anticipated shear strength gain may not be achieved and the failure mode may be dominated by flexure, which would be a useful and predictable upper bound response.

7.0 COMPARATIVE ANALYSIS

Comparisons were made to determine how well predicted values found using R2k and ACI design guides correlated with experimental data. While the main focus remained on specimens tested in this experiment, the specimens discussed in the literature review were used as additional data to determine the efficacy of using R2k as a design aid for NSM-CFRP.

Performance of NSM-CFRP in relation to ACI 440.2R-08: Guide for the Design and Construction of Externally Bonded FRP Systems for Strengthening Concrete Structures and ACI 318-08: Building Code Requirements for Structural Concrete (*American Concrete Institute 2008b)* are of particular interest to this study. R2k was used to determine a base shear capacity for the tested specimens and shear increases were determined using experimental results as described previously in Section 5.2. Alternatively, using ACI provisions, the base capacities of the specimens were determined using ACI 318-08 and the shear contribution of the NSM-CFRP was found using ACI 440.2R-08.

7.1 CONTRIBUTION OF NSM-CFRP TO SHEAR STRENGTH

The increase in shear capacity due to application of NSM-CFRP strips is an important issue for this research. To determine the contribution of the NSM-CFRP to shear capacity, it was necessary to have a base shear capacity for each specimen without NSM reinforcing. R2k was used to estimate the base capacity of each specimen with the measured material properties as described previously in Section 5.2. Each specimen needed a separate R2k model because of different concrete material properties. Using the unstrengthened specimen capacities from R2k, V_{R2k_B}, an estimate of the shear capacity increase due to the NSM-CFRP, $(V_{FRP})_{R2k}$, was determined as:

$$(V_{FRP})_{R2k} = V_{EXP} - V_{R2k\_B} \qquad [7\text{-}1]$$

where V_{EXP} is the experimentally measured shear capacity including self-weight at the failure diagonal crack and V_{R2k_B} is the predicted average base strength of the specimens without CFRP using the individual specimen material properties. The predicted average base strength included the analysis bias of 0.98 based on the work of Higgins *et al*. [2004]. The difference in these two shear values was attributed to the NSM reinforcing. The predicted shear contributions from the NSM-CFRP are reported in Table 7.1. It should be noted that the T specimens failed in flexure rather than shear and thus the values reported are minimum shear strength contributions from the NSM-CFRP.

Table 7.1: Estimated contribution of NSM-CFRP to shear strength using R2k

Specimen	VEXP		VR2k_B		VEXP - VR2k_B	
	[kN]	[kips]	[kN]	[kips]	[kN]	[kips]
T.6.18.6.S*	1011	227	721	162	291	65
T.6.18.12.S*	1043	235	752	169	291	65
IT.7.18.6.S	1209	272	796	179	413	93
IT.7.18.12.S	1022	230	795	179	227	51
IT.5.22.12.S	1011	227	681	153	330	74
IT. 7.22.6.S	1165	262	674	151	492	111
IT.7.22.6.FTG	1250	281	641	144	609	137
IT.7.22.6.FT/FTG	1351	304	671	151	680	153
IT.7.18.6.M	1168	263	749	169	418	94
IT.7.22.6.FT	1125	253	700	157	425	96

*Minimum values due to flexural failure

Another method of determining the base shear capacity is described by the American Concrete Institute. ACI 318-08 determines the base shear capacity by superimposing the concrete shear capacity and steel shear capacity according to the equations below.

$$V_{318-Base} = V_c + V_s \qquad \text{[7-2 – ACI 318 (11-2)]}$$

$$V_c = 2\lambda\sqrt{f'_c}\,b_w d \qquad \text{[7-3 – ACI 318 (11-3)]}$$

$$V_s = \frac{A_v f_y d}{s} \qquad \text{[7-4 – ACI 318 (11-15)]}$$

The numerical values of the specimen's base shear capacity according to ACI 318, $V_{318\text{-base}}$, and the difference from the measured retrofit shear capacity are reported in Table 7.2. Once again, the difference can be attributed to the NSM-CFRP retrofitting. The ACI values, and all other ACI calculated values in this paper, were multiplied by a 1.05 bias (*Turan et al. 2008*). This is to adjust the ACI values to better fit average experimental data based on the analysis method.

Table 7.2: ACI 318 base shear capacity vs. experimental shear capacity

Specimen	VEXP		V318-Base		VEXP- V318-Base	
	[kN]	[kips]	[kN]	[kips]	[kN]	[kips]
T.6.18.6.S*	1011	227	578	130	461	98
T.6.18.12.S*	1043	235	601	135	471	100
IT.7.18.6.S	1209	272	636	143	603	130
IT.7.18.12.S	1022	230	635	143	417	87
IT.5.22.12.S	1011	227	586	132	453	96
IT. 7.22.6.S	1165	262	567	128	625	135
IT.7.22.6.FTG	1250	281	601	135	649	146
IT.7.22.6.FT/FTG	1351	304	627	141	724	163
IT.7.18.6.M	1168	263	608	137	588.7	126
IT.7.22.6.FT	1125	253	586	132	566.6	121

*Minimum values due to flexural failure

Comparison of Table 7.1 and 7.2 shows that the base shear capacities calculated with ACI were consistently lower than the base capacities calculated according to R2k. Due to this, if an ACI approach is used, higher shear strength contributions are attributed to the NSM-CFRP as compared to those in Table 7.1 using R2k.

The individual graphs with unique material properties are shown in Figures 7.1a to 7.1j. These graphs show where the R2k and ACI base shear values and where the experimental shear capacities correspond with the R2k and ACI curves. The graph for specimen IT.5.22.12.S also shows the difference from strain hardening the flexural steel during the initial loading with 152 mm (6 in.) spaced NSM-CFRP. Due to strain hardening, the curve remained linear until a higher shear value, and thus a smaller effective stress in the NSM-CFRP was determined. Figure 7.2 shows all the specimens plotted on the same graphs, but they have been normalized with respect to the concrete compressive strength. R2k curves for each specimen type have been plotted using an average concrete compressive strength of 29 MPa (4200 psi). These normalized curves allow the strength gains for each specimen to be compared along the R2k curves.

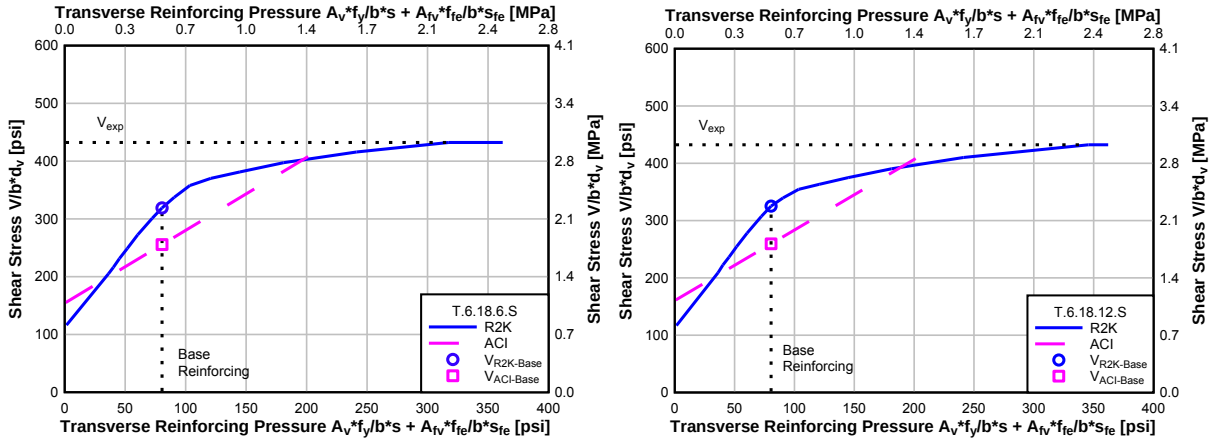

Figure 7.1: R2k and ACI shear strength-transverse reinforcement interaction

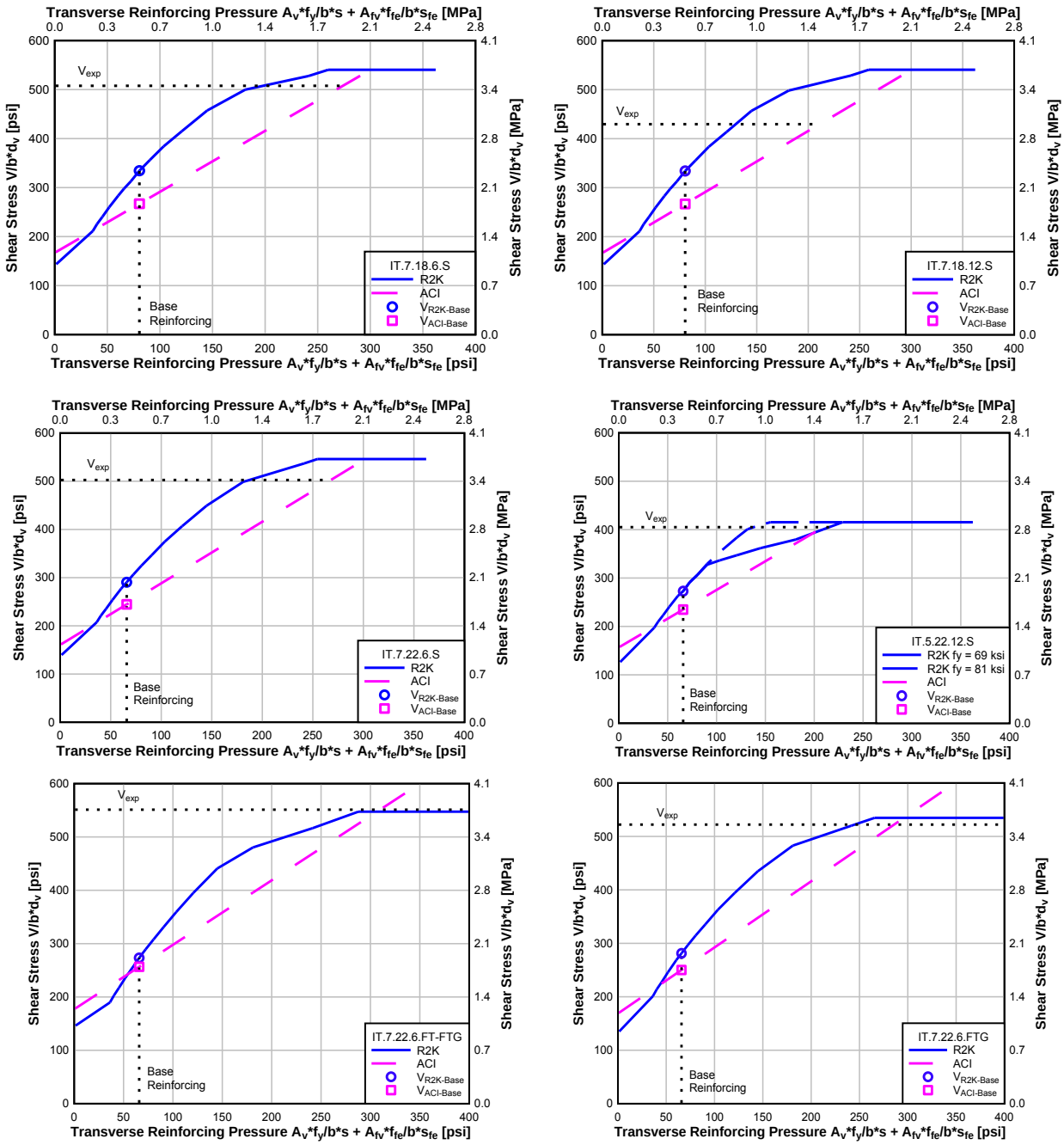

Figure 7.1 (continued): R2k and ACI shear strength-transverse reinforcement interaction

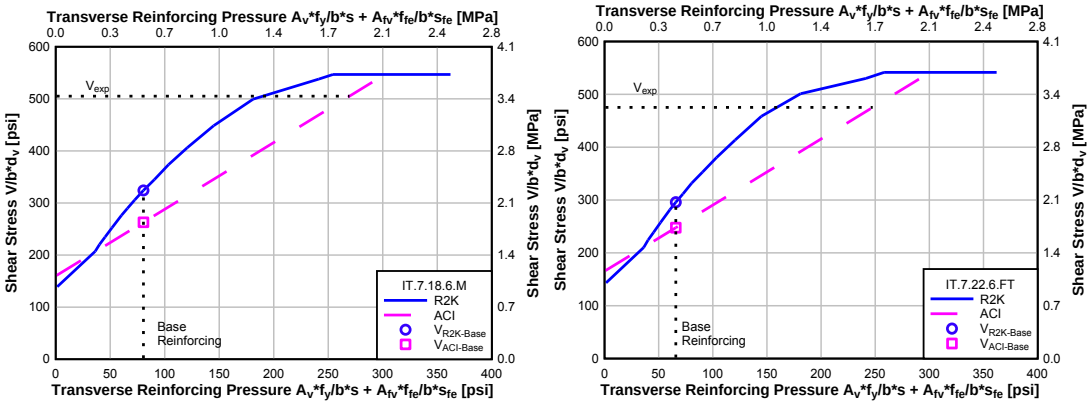

Figure 7.1 (continued): R2k and ACI shear strength-transverse reinforcement interaction

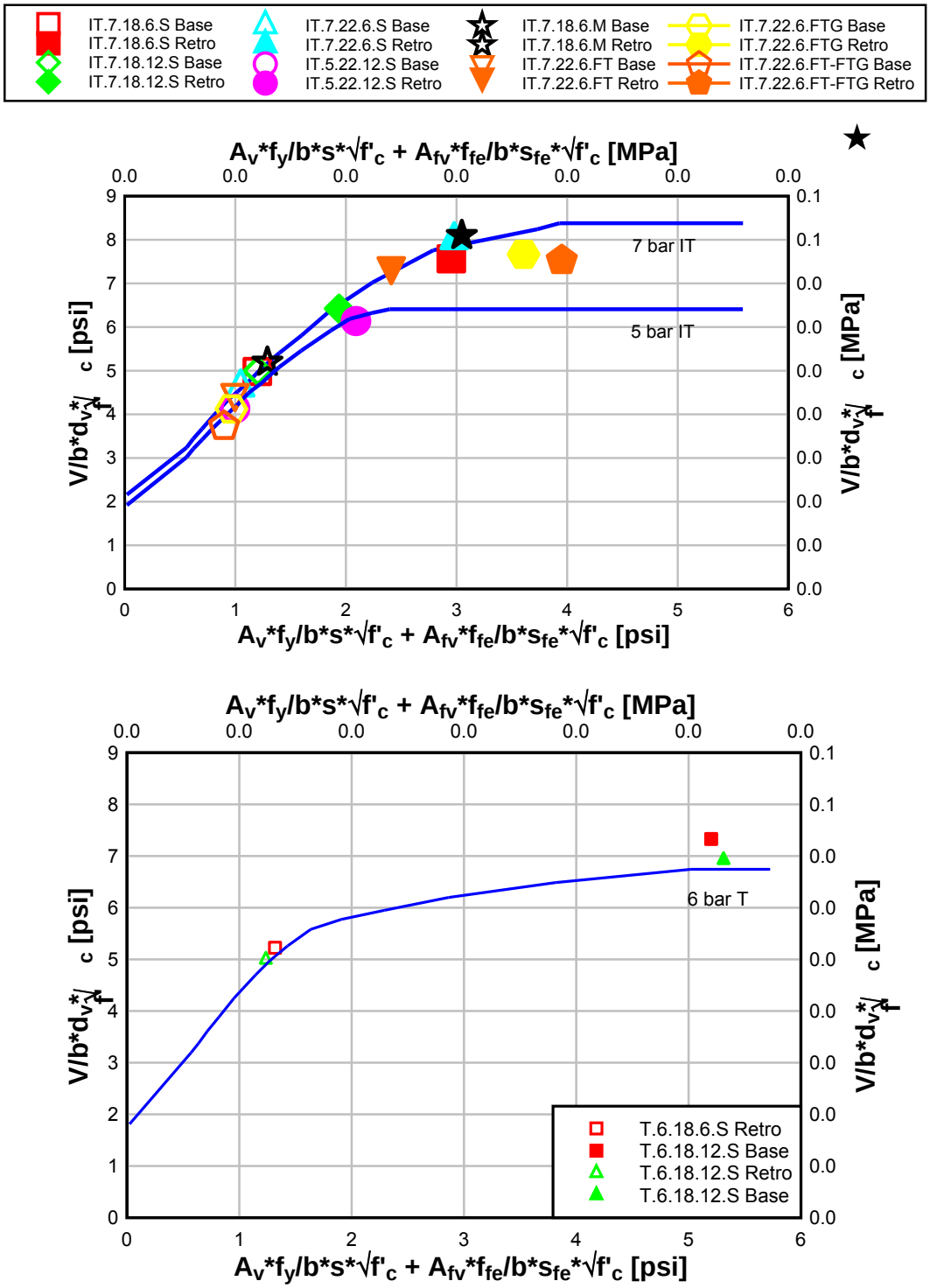

Figure 7.2: Normalized specimens plotted on representative specimen-type curves

7.2 DETERMINING CFRP EFFECTIVE STRESS

Based on the observed experimental specimen strength increases over the R2k predicted base specimen capacity (without NSM-CFRP), an effective CFRP stress was calculated. This was done using Equation 5-3 and the same method as described in Section 5.2. A curve was created for each test specimen using R2k to establish the relationship between the amount of transverse reinforcing and the average ultimate shear stress in the web. Then a transverse reinforcing pressure associated with the NSM-CFRP was taken from the x-axis based on the experimental shear capacity. This is demonstrated in Figure 7.3.

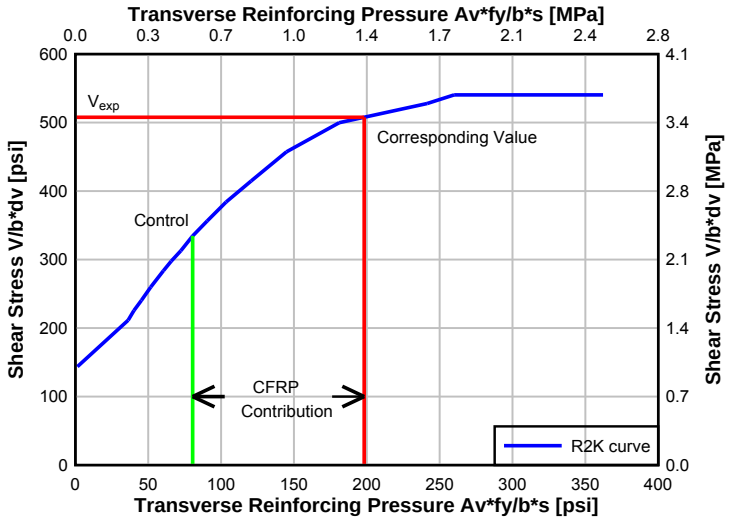

Figure 7.3: Example CFRP contribution based on R2k

An effective CFRP stress can also be calculated based on the strength increase compared to the ACI base capacities. This was done in the same way as that described previously for the R2k method except the base capacity values were calculated using ACI 318 (in the ACI calculation, d_v was used instead of d) and the ACI 318 assumed shear strength increase with transverse reinforcing (linearly increasing) were used. A separate curve was created for each specimen using specific material properties. As shown in Figure 7.4, the effective transverse reinforcing pressure was determined for each specimen.

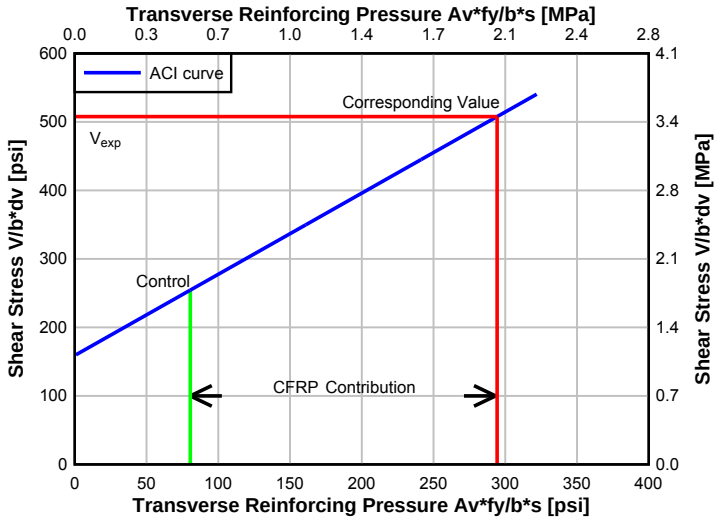

Figure 7.4: Example CFRP contribution based on ACI approach

The stress in the CFRP strips, generally called f_{fe}, was calculated using both R2k and ACI methods. The numerical values from R2k (using Equations 5-2 and 5-3), $f_{fe\text{-}R2k}$, and ACI, $f_{fe\text{-}ACI}$, are listed in Table 7.3. The NSM-CFRP stress values of specimens T.6.18.6.S, T.6.18.12.S, IT.5.22.12.S, IT.7.22.6.FTG, and IT.7.22.6.FT/FTG were much larger than the other stresses from R2k. These specimens either failed in flexure or very near flexural failure. Looking at the interaction between shear strength and transverse reinforcing pressure in Figure 7.1, near the shear stress that corresponds to flexural failure, the R2k curve is nearly flat and shows large increases in transverse reinforcing pressure produce small gains in shear strength. For the other specimens that were not flexurally dominated, the ACI approach predicted a larger effective stress from the NSM-CFRP when compared to the R2k method. This is because the strength gains occur in the steeper region of the R2k curves, thus R2k does not attribute as much NSM-CFRP stress as ACI to achieve the observed strength gains. The average effective NSM-CFRP strains are also shown in Table 7.3 for all specimens and for the set of six specimens that did not fail near the nominal moment capacity.

Table 7.3: Effective CFRP stress based on experimentally measured shear strength and different analysis methods

Specimen	ffe-R2k		ffe-ACI	
	[MPa]	[ksi]	[MPa]	[ksi]
T.6.18.6.S	1367	198	678	98
T.6.18.12.S	3069	445	1622	235
IT.7.18.6.S	695	101	1118	162
IT.7.18.12.S	568	82	1506	218
IT.5.22.12.S	834	121	1668	242
IT. 7.22.6.S	712	103	1181	171
IT.7.22.6.FTG	1042	151	1280	186
IT.7.22.6.FT/FTG	1291	187	1419	206
IT.7.18.6.M	631	92	1100	160
IT.7.22.6.FT	550	80	1054	153
Average of all	1076	156	1263	183
Avg. without flex.	665	97	1271	184

7.2.1 Comparison of ACI 440 Predicted Capacity to Experimental Capacity

ACI 440 describes a method to predict the retrofit capacity of a specimen by determining the shear strength contribution of the CFRP. The method is primarily based on the externally surface bonded technique, but was adapted here for NSM applications. The retrofitted shear strength is a superposition of the concrete and steel contributions from ACI 318 with the CFRP contribution as:

$$V_{440} = V_{318-Base} + V_f \qquad [7\text{-}5]$$

where V_f is the shear contribution of the CFRP taken as:

$$V_f = \frac{A_{fv} f_{fe} (\sin\alpha + \cos\alpha) d_{fv}}{s_f} \qquad [7\text{-}6 – \text{ACI } 440 \text{ (11-3)}]$$

In this equation, A_{fv} is the area of CFRP, f_{fe} is the effective stress of the CFRP, α is the orientation of the CFRP, d_{fv} is the effective depth of CFRP reinforcement, and s_f is the spacing of the CFRP. For the specimens in this research, A_{fv} = 65 mm^2 (0.1 in^2), α = 90°, d_{fv} = 1067 mm (42.0 in.) for IT-specimens and 932 mm (37.6 in.) for T-specimens, s_f = 152 or 305 mm (6 or 12 in.). The effective stress f_{fe} is calculated as:

$$f_{fe} = \varepsilon_{fe} E_f \qquad [7\text{-}7 – \text{ACI } 440 \text{ (11-5)}]$$

where E_f is the CFRP tensile modulus of elasticity (for this research it was taken as 138 GPa (20,082 ksi) based on material tests done by Howell (*2009*)) and ε_{fe} is the effective strain of the CFRP computed assuming the face ply configuration of NSM is similar to two sides bonded with external CFRP. ε_{fe} is calculated as:

$$\varepsilon_{fe} = \kappa_v \varepsilon_{fu} \le 0.004 \qquad [7\text{-}8 – \text{ACI } 440 \text{ (11-6b)}]$$

where ε_{fu} is the ultimate strain of the CFRP (ε_{fu} was calculated by dividing the average tensile stress from material tests by the modulus of elasticity for a strain value of 0.017) and a bond reduction coefficient, k_v, calculated as:

$$\kappa_v = \frac{k_1 k_2 L_e}{468\varepsilon_{fu}} \text{ in US units} \qquad [7\text{-}9 – \text{ACI } 440 \text{ (11-7)}]$$

L_e, k_1, and k_2 are defined as follows:

$$L_e = \frac{2500}{(nt_f E_f)^{0.58}} \text{ in US units} \qquad \text{[7-10 – ACI (11-8)]}$$

$$k_1 = \left(\frac{f'c}{4000}\right)^{2/3} \text{ in US units} \qquad \text{[7-11 – ACI (11-9)]}$$

$$k_2 = \frac{d_{fv} - 2L_e}{d_{fv}} \qquad \text{[7-12 – ACI (11-10)]}$$

For the above equations, L_e is the active bond length, n is the number of plies of CFRP reinforcement, and t_f is the nominal thickness of the CFRP. The NSM technique bonds CFRP strips on three sides in a groove, but the ACI 440 formulation is designed for EBR reinforcing that is bonded on only one face. This was approximated by making $n = 2$ and t_f = half the strip thickness, to account for the two largest sides of the CFRP bonded surfaces. The small edge dimension was ignored. The predicted nominal shear capacities using the ACI 440 approach (adapted here for NSM) are shown in Table 7.4 and compared with the experimentally determined values. As seen here, ACI 440 conservatively predicted the shear capacities of the specimens in all cases. The average experiment-to-predicted capacity was 1.59.

Table 7.4: Predicted retrofitted capacity based on ACI 440 vs. experimental capacity

Specimen	V440*Bias		VEXP –		VEXP/V440
	[kN	[kips	[kN]	[kips]	
T.6.18.6.S	685	154.1	326	73.3	1.48
T.6.18.12.S	659	148.2	384	86.3	1.58
IT.7.18.6.S	774	173.9	435	97.9	1.56
IT.7.18.12.S	703	158.0	319	71.7	1.45
IT.5.22.12.S	653	146.8	358	80.5	1.55
IT. 7.22.6.S	693	155.8	472	106.2	1.68
IT.7.22.6.FTG	738	165.9	512	115.1	1.69
IT.7.22.6.FT/FTG	785	176.4	568	127.6	1.72
IT.7.18.6.M	732	164.6	435	97.9	1.59
IT.7.22.6.FT	721	162.0	404	90.9	1.56

7.2.2 Comparison of Nanni, et al. (*2004*) Capacity to Experimental Capacity

Nanni et. al. (*2004*) presents a method of calculating the shear capacity of NSM-CFRP retrofit concrete similar to the ACI 440 method. This method is suggested on the Hughes Brothers website for design of NSM-CFRP for retrofit of reinforced concrete structures. The approach is still based on the superposition of the concrete, steel, and CFRP shear contributions. The difference is that the CFRP contribution, V_{fn}, is determined as:

$$V_{Nanni} = V_c + V_s + V_{fn} \quad [7\text{-}13]$$

$$V_{fn} = 4(a+b)\tau_b L_{tot} \quad [7\text{-}14]$$

The equation is for rectangular bars with cross sectional dimensions of a and b. The average bond stress, τ_b, is suggested to be taken as 6.9 MPa (1.0 ksi) based on previous research. L_i shown below represents the length of each NSM bar extending beyond a diagonal crack and L_{tot}, is the summation of those attributing lengths.

$$L_i = \begin{cases} \dfrac{s}{\cos\alpha + \sin\alpha} \; i \le l_{0.004} & \text{for i = 1…n/2} \\ l_{net} - \dfrac{s}{\cos\alpha + \sin\alpha} \; i \le l_{0.004} & \text{for i = n/2+1…n} \end{cases} \quad [7\text{-}15]$$

The limitation $l_{0.004}$ is based on the integrity of the concrete. In the present calculations, this length was determined as 71 mm (2.8 in.) and controlled for every NSM strip. The value n below must be rounded down to the nearest integer to represent a number of strips.

$$l_{net} = l_b - \frac{2c}{\sin\alpha} \quad [7\text{-}16]$$

$$n = \frac{l_{eff}(1+\cot\alpha)}{s} \quad [7\text{-}17]$$

$$l_{eff} = l_b \sin\alpha - 2c \quad [7\text{-}18]$$

$$l_{0.004} = 0.002\frac{ab}{a+b}\frac{E_f}{\tau_b} \quad [7\text{-}19]$$

$$L_{tot} = \sum L_i \quad [7\text{-}20]$$

Following the prescribed approach, conservative shear strengths were determined for all the specimens and are reported in Table 7.5. In this table, the V_c and V_s contributions include the analysis bias of 1.05, but a bias of 1.0 was applied to the V_{fn} contribution. The predicted strengths are compared to the experimental values and the results are seen to be conservative.

The average experiment-to-predicted capacity was 1.45 and was slightly less conservative than the ACI 440 procedure.

Table 7.5: Predicted retrofitted capacity based on Nanni, et al. (*2004*) vs. experimental capacity

Specimen	VNanni		VEXP – VNanni		VEXP/VNanni
	[kN]	[kips]	[kN]	[kips]	
T.6.18.6.S	791	177.8	220	49.6	1.28
T.6.18.12.S	707	159.0	336	75.5	1.47
IT.7.18.6.S	849	191.0	360	80.8	1.42
IT.7.18.12.S	741	166.7	281	63.0	1.38
IT.5.22.12.S	693	155.7	318	71.6	1.46
IT. 7.22.6.S	781	175.5	385	86.5	1.49
IT.7.22.6.FTG	811	182.4	439	98.6	1.54
IT.7.22.6.FT/FTG	844	189.8	508	114.3	1.60
IT.7.18.6.M	821	184.6	347	77.9	1.42
IT.7.22.6.FT	800	179.8	325	73.1	1.41

7.3 CAPACITIES OF SPECIMENS REPORTED IN THE LITERATURE

In an effort to determine if R2k can effectively predict the NSM-CFRP contribution of a specimen, 14 specimens from the literature review were reanalyzed. CFRP bars were input into R2k models as an additional shear reinforcing layer with material properties and a cross-section that matched those reported by the authors. V_{EXP} is the experimental shear capacity, V_{R2k_B} is the predicted baseline capacity using R2k, $(V_{FRP})_{R2k}$ is the apparent increase in shear capacity above the R2k baseline capacity taken as V_{EXP} - V_{R2k_B}. The apparent increase in shear capacity was attributed to the CFRP which, given the spacing and area of the bars in the archival literature, the average effective stress $f_{fe\text{-}R2k}$ was calculated previously in Section 5.3 as 441 MPa (64 ksi), The shear capacity of the retrofitted specimen with NSM-CFRP modeled in R2k with an average effective stress of 441 MPa (64 ksi), is defined as V_{R2k_R}. Results from this analysis indicated an average over-prediction in shear strength of 10.1% with a coefficient of variation of 12.3%. The results of this analysis are shown in Table 7.6. Comparing the average effective stress used based on the archival results (64 ksi) with the average effective stress found from tests of the large size specimens in this research (Table 7.3 considering only shear dominant failures =97 ksi), the prediction of large size members with NSM-CFRP would be expected to be conservative.

Table 7.6: R2k capacity predictions of literature review specimens

Specimen	VEXP (kN) [kips]	VR2k_B (kN) [kips]	(VFRP)R2k (kN) [kips]	ffe-R2k (MPa) [ksi]	VR2k_R (kN) [kips]	VR2k_R / VEXP
De Lorenzis 2001 (BS90-7A)	207 [46.5]	157.6 [35.4]	49.4 [11.1]	596 [86.5]	201 [45.1]	0.97
Dias 2007 (2S-7LV)	164 [36.9]	115.5 [26.0]	48.7 [10.9]	378 [54.9]	192 [43.2]	1.17
Dias 2007 (4S-7LV)	189 [42.5]	158.0 [35.5]	31.1 [7.0]	333 [48.3]	216 [48.5]	1.14
Dias 2008 (2S-3LV)	189 [42.6]	135.5 [30.5]	53.5 [12.1]	804 [117]	164 [36.9]	0.87
Dias 2008 (2S-5LV)	214 [48.2]	135.5 [30.5]	78.7 [17.7]	719 [104]	200 [44.9]	0.93
Dias 2008 (2S-8LV)	238 [53.4]	135.5 [30.5]	102.1 [22.9]	595 [86.2]	246 [55.2]	1.03
Rizzo 2009 (NB90-73-a)	176 [39.6]	105.2 [23.7]	70.8 [16.0]	N/A N/A	184 [41.4]	1.04
Rizzo 2009 (NB90-73-b)	149 [33.5]	105.2 [23.7]	43.8 [9.9]	228 [33.1]	184 [41.4]	1.23
Rizzo 2009 (NB90-45-b)	151 [33.9]	105.2 [23.7]	45.8 [10.3]	151 [21.8]	185 [41.6]	1.23
Rizzo 2009 (NS90-73-a)	173 [38.9]	105.2 [23.7]	67.8 [15.3]	N/A N/A	166 [37.4]	0.96
Howell 2009 (B.IT.NC.NS)	740 [166]	734.0 [165.0]	6.0 [1.0]	13 [1.9]	833 [187]	1.13
Dias 2010 (2S-4LV)	202 [45.5]	141.4 [31.8]	61.0 [13.7]	558 [81.0]	235 [52.8]	1.16
Dias 2010 (2S-7LV)	225 [50.5]	141.4 [31.8]	83.1 [18.7]	500 [72.5]	274 [61.6]	1.22
Dias 2010 (2S-10LV)	239 [53.6]	141.4 [31.8]	97.1 [21.8]	417 [60.5]	316 [71.1]	1.33
Mean				441 [64.0]		1.101
COV (%)				53.1		12.3

7.4 PREDICTION OF SPECIMEN SHEAR STRENGTH USING R2K

The test specimens were modeled using R2k to predict the shear strengths and compare them with the experimentally observed results. The NSM-CFRP was modeled as a T-headed single leg stirrup with an area equal to twice that of the CFRP strip to account for application of the materials on both sides of the stem. An average effective CFRP stress of 669 MPa (97 ksi) was used for the NSM-CFRP stirrup (considering only those specimens that did not fail near the flexural capacity) and the material was considered elastic until failure. An estimation for the modulus of elasticity for the NSM-CFRP stirrup in epoxy was taken as 43,554 MPa (6317 ksi) based on results from the bond specimens described in Appendix D. An example R2k model is shown in Figure 7.5. The retrofitted shear capacity using R2k, V_{R2k_R}, for each specimen was computed and results are shown in Table 7.7. The results show that using average effective NSM-CFRP stress as the input material property, R2k conservatively estimated the specimens with a bias of 1.15 and a COV of 6.6%.

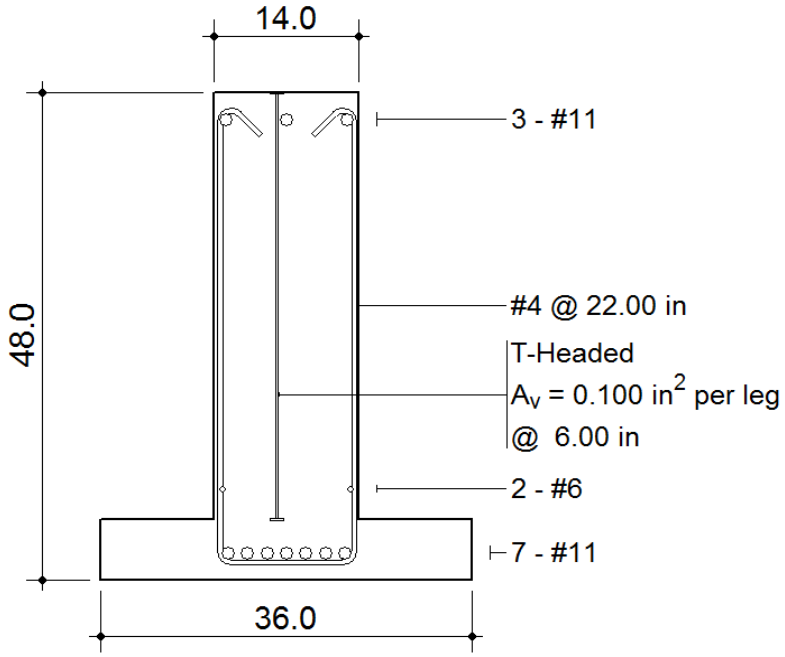

Figure 7.5: Example R2k model with NSM-CFRP

Table 7.7: Specimens with NSM-CFRP modeled in R2k using experimental average effective NSM-CFRP stress

Specimen	VEXP (kN) [kip]	VR2k_R (kN) [kip]	VEXP /VR2k_R
T.6.18.6.S	1011 [227]	874 [196]	1.15
T.6.18.12.S	1043 [235]	854 [192]	1.22
IT.7.18.6.S	1209 [272]	1132 [255]	1.06
IT.7.18.12.S	1022 [230]	978 [220]	1.04
IT.5.22.12*.S	1011 [227]	826 [186]	1.22
IT.7.22.6.S	1165 [262]	1042 [234]	1.12
IT.7.22.6.FTG	1250 [281]	1050 [236]	1.19
IT.7.22.6.FT/FTG	1351 [304]	1056 [237]	1.28
IT.7.18.6.M	1168 [263]	1063 [239]	1.10
IT.7.22.6.FT	1125 [253]	1029 [231]	1.10
Mean			1.15
COV (%)			6.7

8.0 DESIGN RECOMMENDATIONS

8.1 CONTRIBUTION OF NSM-CFRP TO SHEAR STRENGTHENING

Based on the results of the full-scale test specimens, it is desirable to develop a design method that can be used to determine the safe contribution of transverse NSM-CFRP reinforcing to shear strength. A traditional approach allows a designer to select a CFRP strip spacing, similar to stirrup spacing, to achieve the desired shear strength based on the capacity that can be provided by the CFRP. To implement this approach, an effective CFRP stress for design is required. In design provisions this is limited based on bond stresses or a limiting strain value for the CFRP. For the present research, an effective CFRP stress, f_{fe}, was used based on experiments found in the archival literature and combined with values developed for the specimens in this research. As shown previously, the effective NSM-CFRP stress can be calculated based on R2k or ACI predicted shear strength-transverse reinforcing interaction curves, but the R2k effective stress values are used here because R2k reasonably includes the moment shear interactions and provides more accurate predictions of member shear capacity (*Higgins et al. 2004*).

All the specimens from this research and from the literature review were considered, but only those archival specimens that used CFRP strips instead of bars, internal steel stirrups, and a flexural reinforcing ratio less than 3% were considered. The T-specimens from this research were not used because they failed in flexure, and the fatigue specimens were also not used as these failed very close to the theoretical flexural capacity. The specimens that were used and the corresponding effective CFRP stresses are shown in Table 8.1. The average effective CFRP stress from the experiments was 669 MPa (97 ksi). For simplicity, 670 MPa (95 ksi) was selected as the value of f_{fe} for convenience in NSM-CFRP design. Considering the measured modulus of elasticity of the CFRP strips used in this study (~20,000 ksi), this corresponds to an effective average strain of approximately 0.0048 in/in.

Table 8.1: Effective CFRP stress used for design

Specimen	ffe	
	[MPa]	[ksi]
IT.7.18.6.S	682	99
IT.7.18.12.S	635	92
IT. 7.22.6.S	569	83
IT.5.22.12.S	834	121
IT.7.18.6.M	703	102
IT.7.22.6.FT	541	78
IT.7.22.6.FT-FTG	1434	208
IT.7.22.6.FTG	1041	151
Dias 07 2S-7LV	378	55
Dias 07 4S-7LV	333	48
Dias 08 2S-3LV	804	117
Dias 08 2S-5LV	719	104
Dias 08 2S-8LV	595	86
Dias 10 2S-4LV	558	81
Dias 10 2S-7LV	500	73
Dias 10 2S-10LV	417	61
Rounded Average	670	95

There are three possible design methods to choose from: R2k, AASHTO-MCFT, and ACI. It was determined that each design method should apply a strength reduction factor, ϕ, to the overall shear capacity and an NSM strength reduction factor, Ψ, to the CFRP effective stress. The goal of using these two reduction factors was to achieve a 1/10,000 chance that the actual member shear capacity will be below the design shear capacity. AASHTO and ACI already have established ϕ factors of 0.9 and 0.75, respectively. It was determined that R2k should also have a ϕ factor and that the AASHTO factor was appropriate because this factor represented accuracy in the design method and was a simplified approximation for modified compression field theory (MCFT). To calibrate the design approach, a graph of each of the listed specimens was created with curves generated using R2k, AASHTO, and ACI as illustrated in Figure 8.1. Analysis bias was not used for these curves in order to achieve the desired design reliability without needing to correct for analysis bias individually.

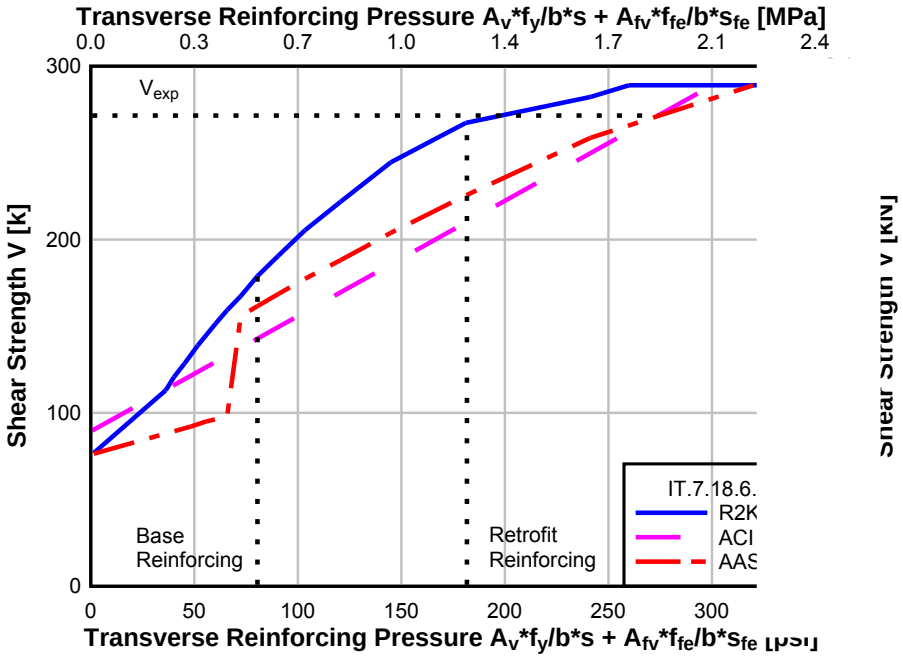

Figure 8.1: Example shear strength curves and retrofit capacity with average f_{fe}

The shear strength for each specimen was determined from these curves. The shear values for each design approach were multiplied by the appropriate strength reduction factor to provide design shear strength curves. Then a stress reduction factor, Ψ, was multiplied by the CFRP effective stress and the transverse reinforcing pressure was calculated. The value where this transverse reinforcing pressure intersects the corresponding design shear curve is the design shear strength. An example of this is shown in Figure 8.2

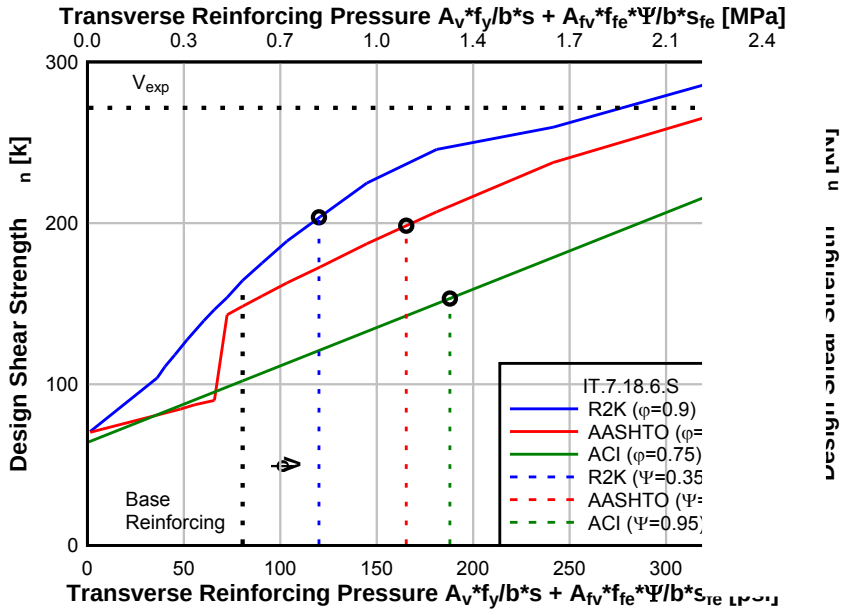

Figure 8.2: Example design shear curves and NSM-CFRP transverse reinforcing pressure

The design shear strength was determined for each of the specimens in Table 8.1 and then compared to the experimental shear strength. A ratio of the experimentally observed strength to the design strength was defined for each specimen ($V_{EXP}/\phi V_{design}$). If this ratio was less than one, it meant the observed strength was less than the design strength. Statistics were used to determine how many standard deviations the average ratio of $V_{EXP}/\phi V_{design}$ was removed from unity. This value, β, needed to be just above 3.5 to represent a 1/10,000 probability that the actual member shear capacity was below the design shear capacity. The values for the specimens and the statistics are shown in Table 8.2. Calibrating ϕ and Ψ values for each design method was performed iteratively. As mentioned before, the ϕ factors were already established in the relevant specifications and were retained as the recommended values for each method. Thus, a Ψ was chosen to establish the target β value for the group of specimens. The Ψ value was adjusted until β was above 3.5 for each method. From the iterations, the factors in Table 8.3 are suggested.

Table 8.2: Design shears values and corresponding probability of failure

Specimen	VEXP [kips]	φVR2k [kips]	VEXP/ φVR2k	φVAASHTO [kips]	VEXP/ φVAASHTO	φVACI [kips]	VEXP/ φVACI
IT.7.18.6.S	271.8	203.0	1.34	198.4	1.37	153.2	1.77
IT.7.18.12.S	229.7	184.0	1.25	174.1	1.32	127.5	1.80
IT. 7.22.6.S	262.0	181.0	1.45	185.0	1.42	142.2	1.84
IT.5.22.12.S	227.0	164.0	1.38	154.8	1.47	119.7	1.90
IT.7.18.6.M	262.5	194.0	1.35	192.6	1.36	148.7	1.77
IT.7.22.6.FT	252.9	187.0	1.35	188.7	1.34	145.2	1.74
IT.7.22.6.FT-FTG	303.8	184.1	1.65	197.7	1.54	152.1	2.00
IT.7.22.6.FTG	281.1	181.1	1.55	192.3	1.46	147.3	1.91
Dias 07 2S-7LV	36.9	26.5	1.39	31.2	1.18	23.2	1.59
Dias 07 4S-7LV	42.5	31.0	1.37	36.1	1.18	27.3	1.56
Dias 08 2S-3LV	42.6	27.5	1.55	29.9	1.42	20.0	2.13
Dias 08 2S-5LV	48.2	28.9	1.67	33.1	1.46	22.6	2.13
Dias 08 2S-8LV	53.4	31.1	1.71	36.8	1.45	26.5	2.01
Dias 10 2S-4LV	45.5	30.4	1.50	34.2	1.33	23.5	1.94
Dias 10 2S-7LV	50.5	32.3	1.56	37.6	1.34	26.9	1.88
Dias 10 2S-10LV	53.6	34.5	1.55	41.3	1.30	30.9	1.74
Mean			1.48		1.37		1.86
Stdev			0.14		0.10		0.17
Mean – 1.0			0.48		0.37		0.86
Beta			3.51		3.75		5.15

Table 8.3: Suggested reduction factors for NSM-CFRP shear design

Method	Φ	Ψ
R2k	0.9	0.35
AASHTO	0.9	0.75
ACI	0.75	0.95

As seen in Table 8.3, R2k and AASHTO have larger NSM-CFRP effective stress reduction factors than ACI. This is because R2k and AASHTO provide more accurate predictions of shear strength and thus have smaller strength reduction factors. Thus, to achieve the same reliability, the Ψ factor must be smaller.

To design the NSM-CFRP shear reinforcing for a reinforced concrete girder with a known cross-section and material properties, the process consists of the following steps:

- Select design approach: R2k, AASHTO, or ACI
- Use appropriate ϕ and create design shear curve for section (this is done by varying the transverse reinforcing pressure and computing the shear capacity of the section for many values of transverse reinforcing pressure)
- Choose a NSM-CFRP spacing
- Use appropriate Ψf_{fe} and calculate transverse reinforcing pressure
- Determine the design shear capacity by selecting the corresponding value from the design shear curve
- Check that design shear capacity is above the required shear demand

8.2 EXAMPLE SHEAR DESIGN IMPLEMENTATION

This section presents an example NSM-CFRP shear design for an existing bridge girder in an actual 1950's vintage RCDG bridge that follows the recommended design approach. The sample bridge girder is representative of the Springfield Bridge over the Willamette River and has the dimensions and properties listed in Table 8.4 and shown in Figure 8.3. It has hypothetically been determined that the girder needs to be strengthened in shear to handle a factored demand of 756 kN (170 kips) at a location 3.0 m (10 ft.) away from the support where the steel stirrup spacing is 381 mm (15 in.), and the moment demand is positive. This section is checked as an example, but an actual design would consider multiple sections including the location d_v away from the support where the shear demand is larger, and the stirrup spacing is smaller.

Table 8.4: Example girder properties

Property	SI	US
beff	221 cm	87 in
M/V	6.0	6.0
bw	33 cm	13 in
h	122 cm	48 in
cc	51 mm	2 in
dv	107 cm	42 in
Fy	276 MPa	40 ksi
Fyv	276 MPa	40 ksi
As	90.6 cm2	14.04 in2
Av	2.6 cm2	0.4 in2
s	381 mm	15 in
ffe	670 MPa	95 ksi

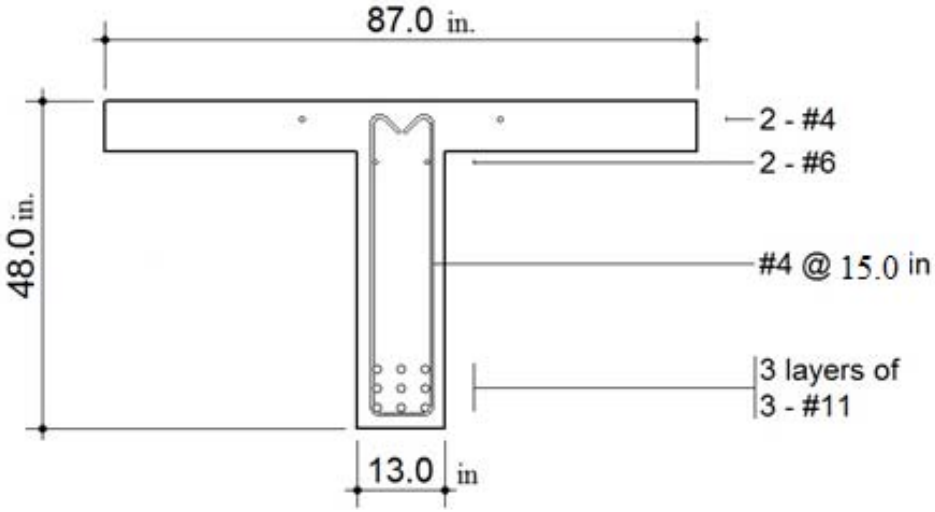

Figure 8.3: Cross-section of example girder 3.0 m (10 ft.) away from support

The first step is to create design shear strength curves for the girder using the recommended shear strength reduction factors. Curves for all three design methods are demonstrated in Figure 8.4. Biases are not applied to these curves.

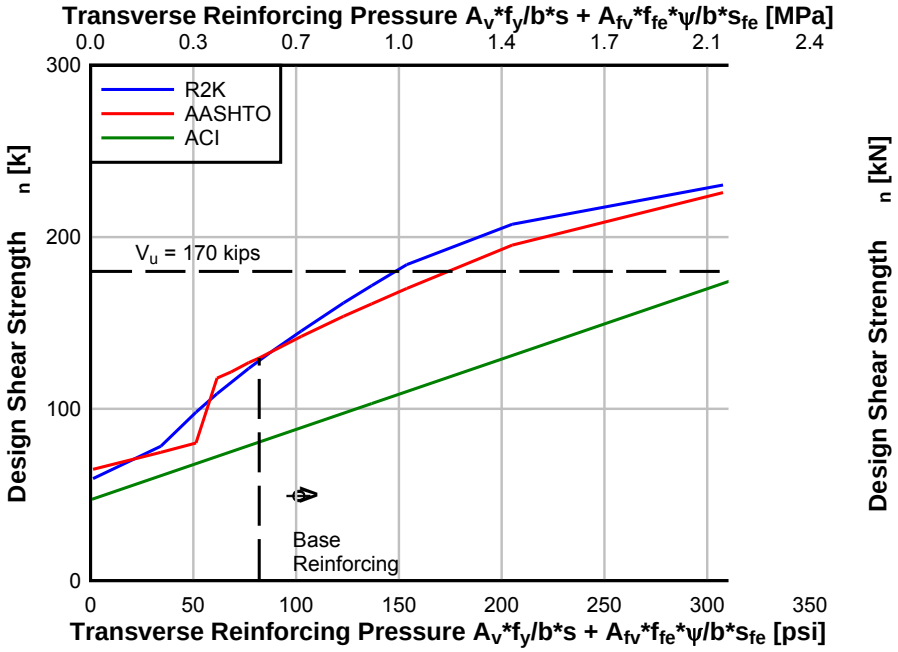

Figure 8.4: Design curves with base reinforcing and shear demand

The base transverse reinforcing pressure is determined from the internal stirrup spacing using the following equation:

$$Base = \frac{A_v * fy}{b * s} = \frac{0.4in^2 * 40,000\,psi}{13in * 15in} = 82\,psi \qquad [8\text{-}1]$$

It is clear that the design strength with the current base reinforcing falls below the shear demand. The next step is to calculate a CFRP spacing that will provide a design shear capacity above the demand. This is done by adding a CFRP contribution to the base reinforcing transverse pressure using Equation 8-2 and the recommended effective NSM-CFRP stress reduction factors.

$$CFRP = \frac{A_{fv} * f_{fe} * \psi}{b * s_f} \qquad [8\text{-}2]$$

$$\text{Re}trofit = Base + CFRP \qquad [8\text{-}3]$$

The design is completed by selecting the CFRP spacing and finding the corresponding design strength on the curve. The widest possible spacing that would achieve at least the factored shear demand is chosen. Table 8.5 shows the values in the calculations, and for comparison it lists the expected shear capacities (average expected shear capacity) for each method and NSM-CFRP spacing with no reduction factors applied. Figure 8.5 shows the shear curves with CFRP retrofitting values. AASHTO suggests a NSM-CFRP strip spacing of 178 mm (7.0 in.) is sufficient. R2k method suggests a more conservative spacing of 127 mm (5.0 in.). The ACI design method requires a spacing of 76 mm (3.0 in.), which is in the realm of unrealistic and is

due to the overly conservative nature of the ACI approach. This is particularly due to the calibration process used here that retained the strength reduction factor established for shear in ACI 318 (0.75) producing a much higher reliability (β over 5) than the R2k or AASHTO-MCFT methods. It is recommended in this design to use the more conservative value for spacing suggested by AASHTO or R2k and therefore implement a 127 mm (5.0 in.) NSM-CFRP spacing.

Table 8.5: Calculated CFRP spacings and shear design capacities for example girder

Method	Retrofit Pressure (Av*ffe*Ψ/b*s)		CFRP spacing		φVn#		Vexpected	
	[MPa]	[psi]	[mm]	[in]	[kN]	[kips]	[kN]	[kips]
R2k	0.92	134	127	5.0	770	170	1050	236
AASHTO	1.10	160	178	7.0	774	174	921	207
ACI	2.16	313	76	3.0	783	176	1072	241

this includes the base reinforcing contribution from the original steel stirrups plus the NSM contribution

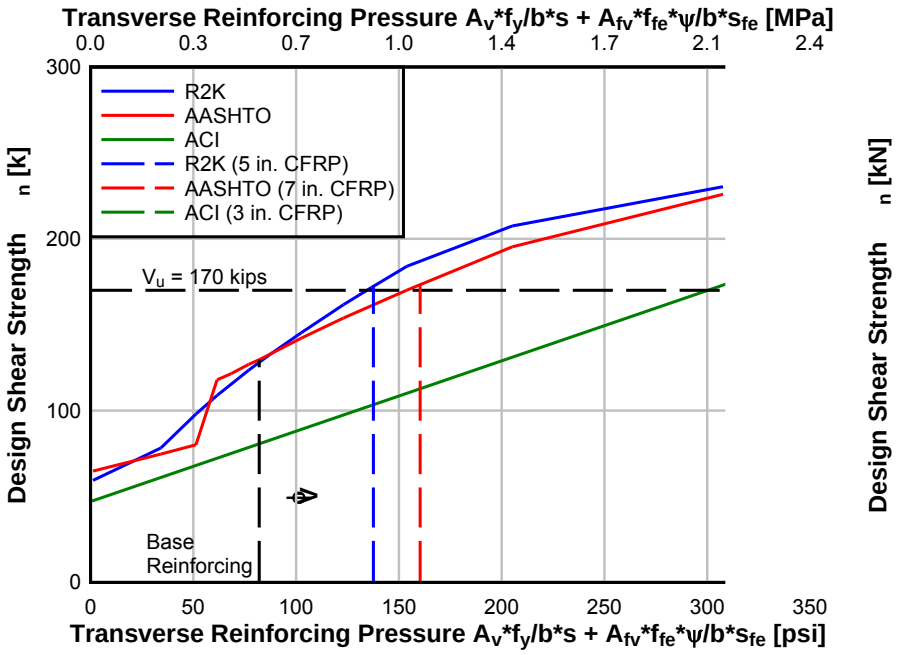

Figure 8.5: Example shear design curves with retrofit transverse pressures

8.3 DISCUSSION

It would be expected that all three design methods should give similar results due to the calibrated reduction factors. One reason for the difference between R2k and AASHTO is that the factors were calibrated to a small population of specimens with specific M/V ratios and amounts of flexural reinforcing. If more data were available, more precise design values could be achieved over a wider range of input parameters.

Furthermore, the ACI method gave a NSM-CFRP spacing which was more conservative than the other two methods. This is partially because a ϕ factor of 0.75 was maintained for ACI in the calibration process and resulted in a higher reliability than the other two methods. If ϕ were changed to produce similar reliability levels with the other methods, then a wider NSM-CFRP spacing would be expected. Table 8.6 shows the ACI calibration values for a strength reduction factor ϕ of 0.95. This provides a reliability similar to that of the R2k and AASHTO-MCFT with β= 3.54. Figure 8.6 demonstrates the same design example with this ACI strength reduction factor. As expected, ACI now produces a NSM-CFRP spacing of 127 mm (5.0 in.) which is the same as that based on the R2k calibration.

Table 8.6: ACI design shear values with ϕ of 0.95.

Specimen	VEXP [kips]	φVACI [kips]	VEXP/ φVACI
IT.7.18.6.S	271.8	194.1	1.40
IT.7.18.12.S	229.7	161.5	1.42
IT. 7.22.6.S	262.0	180.1	1.45
IT.5.22.12.S	227.0	151.6	1.50
IT.7.18.6.M	262.5	188.4	1.39
IT.7.22.6.FT	252.9	184.0	1.37
IT.7.22.6.FT-FTG	303.8	192.7	1.58
IT.7.22.6.FTG	281.1	186.6	1.51
Dias 07 2S-7LV	36.9	29.5	1.25
Dias 07 4S-7LV	42.5	34.6	1.23
Dias 08 2S-3LV	42.6	25.3	1.68
Dias 08 2S-5LV	48.2	28.6	1.68
Dias 08 2S-8LV	53.4	33.6	1.59
Dias 10 2S-4LV	45.5	29.8	1.53
Dias 10 2S-7LV	50.5	34.1	1.48
Dias 10 2S-10LV	53.6	39.1	1.37
Mean			1.47
Stdev			0.13
Mean – 1.0			0.47
Beta			3.54

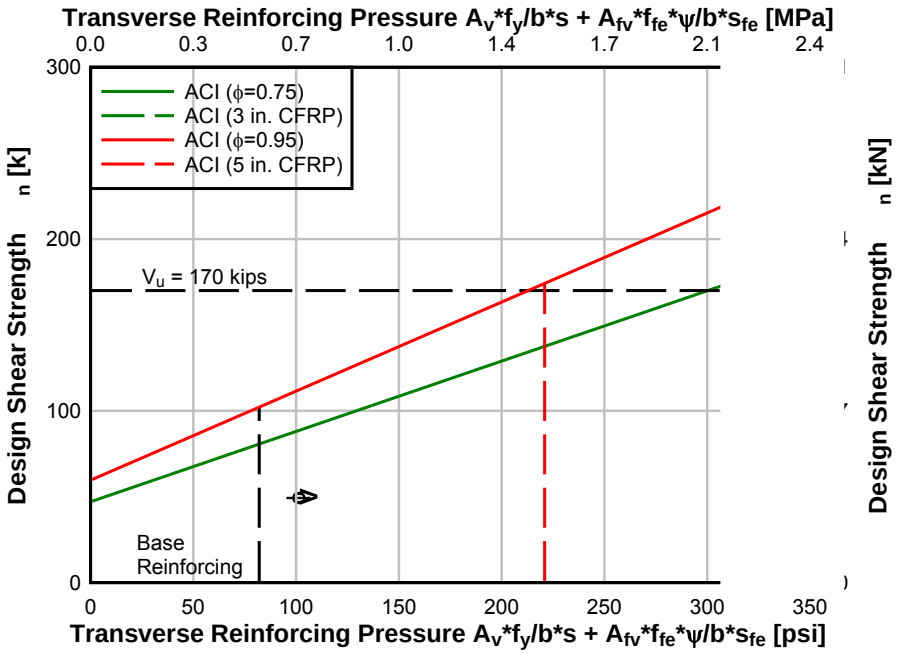

Figure 8.6: Example ACI shear design curves with different strength reduction factors

To complete a design, the flexural capacity must also be checked. Calculating the moment capacity of the sections shows a value of 2160 kN-m (1605 k-ft). Given the shear-moment ratio at the section considered, the corresponding shear at flexural capacity is 1188 kN (267 kips). This is higher than that factored shear demand 756 kN (170 kips) and thus flexure will not control the design. If a designer wanted to shift the failure mode from shear to flexure, for the example girder given the M/V ratio, the transverse pressures and resulting CFRP strip spacings for each design method would take a spacing tighter than 51 mm (2 in.). Such small spacings are not realistic, and it can be seen in Figure 8.5 that the shear to cause flexural failure (1188 kN (267 kips)) would fall above the shear design curves. This means that in practical terms it is not be posssible to shift this member at this section into a flexurally controlled failure mode.

It should be noted that the shear demand decreases away from the support; consequently, a larger CFRP spacing could be used further along the shear span. Another point is that specimens with lighter flexural reinforcing have R2k and AASHTO curves that flatten in the flexurally dominant region. A specimen with heavy flexural reinforcement has a steeper curve, and thus has larger reductions in shear strength for the same CFRP effective stress reduction factor (Ψ). As a result, it is not possible to have the same level of reliability for specimens with different amounts of flexural reinforcing with the present calibration and limited data. With more data, it would be possible to determine a sliding scale for Ψ based on whether the design shear strength falls in the flexurally dominant or shear dominant region of the curve.

8.3.1 Reliability of the R2k-based Method

This section looks at the reliability of the design example using statistics from the R2k models compared to experimental values. Previously, the R2k predicted shear capacity of the specimens was obtained by modeling a supplemental NSM-CFRP stirrup in the cross section. This was repeated here, but with an effective NSM-CFRP stress set to (95 ksi) and no analysis bias. The values for the specimens used in this design recommendation are reported in Table 8.7. The average bias from the experimental capacities for these models was 1.13 with a standard deviation of 0.17.

Table 8.7: NSM-CFRP modeled in R2k compared to experimental values

Strengthened Specimen	VEXP		VR2k		VEXP / VR2k
	[kN]	[kips]	[kN]	[kips]	
Dias 2S-7LV	164	36.9	180	40.5	0.91
Dias 4S-7LV	189	42.5	205	46.2	0.92
Dias 2S-3LV	189	42.6	123	27.6	1.54
Dias 2S-5LV	214	48.2	154	34.7	1.39
Dias 2S-8LV	238	53.4	193	43.3	1.23
Dias 2S-4LV	202	45.5	194	43.6	1.04
Dias 2S-7LV	225	50.5	215	48.4	1.04
Dias 2S-10LV	239	53.6	239	53.7	1.00
IT.7.18.6.S	1209	271.8	1089	244.8	1.11
IT.7.18.12.S	1022	229.7	911	204.9	1.12
IT. 7.22.6.S	1165	262.0	1040	233.7	1.12
IT.5.22.12.S	1011	227.3	809	181.9	1.25
IT.7.18.6.M	1168	262.5	1064	239.1	1.10
IT.7.22.6.FT	1125	252.9	1029	231.4	1.09
Average:					1.13
Stdev:					0.17
Lower bound (3.5 σ)					0.60

A curve representing shear strength versus transverse pressure was plotted using R2k. The curve was then adjusted with the bias from the population of experiments to achieve an expected R2k curve. Then a lower bound curve was produced (3.5 standard deviations from the mean) to represent approximately 1/10,000 chance of member understrength. At the transverse pressure for the base specimen, a bias of 1.05 and standard deviation of 0.12 were applied based on work from Bentz (*2000*) because the base specimen does not have NSM-CFRP. The lower bound curve has a horizontal portion because the NSM-CFRP strengthened member cannot have a lower capacity than that possible with the base specimen (without NSM-CFRP). These curves are shown in Figure 8.7. At the transverse pressures, for spacings of 76 mm, 127 mm, and 178 mm (3 in., 5 in., and 7 in.), the shear demand of 756 kN (170 kips) is located above the lower R2k bound. This means that the chance of failure of a single girder is above 1/10,000 for the example girder and all transverse pressures. The reason for this is because the calibrated

reliability was based on CFRP effective stress instead of shear strength. However, considering that a single girder is one part of a bridge system which has multiple girders acting together, if a hypothetical bridge with four girders is considered, then truck loading on the bridge is shared over multiple girders. Thus the system reliability will be better than any single girder and can achieve the desired reliability.

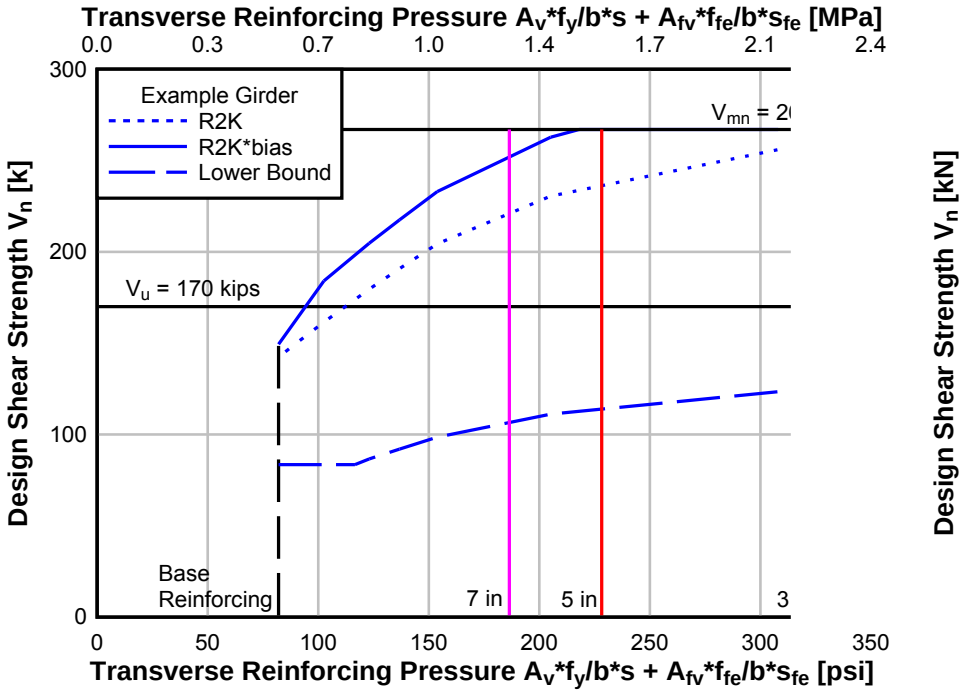

Figure 8.7: Example R2k curves with lower reliability bound

9.0 CONCLUSIONS

Laboratory tests were performed on ten full-size conventionally reinforced concrete bridge deck girders built with dimensions, materials, and details representative of 1950's vintage bridges. All specimens were precracked, strengthened with NSM-CFRP, and tested to failure. Two specimens were subjected to fatigue loading before failure testing. One of the fatigue specimens was simultaneously exposed to 400 cycles of freeze-thaw conditions. One specimen was submerged in water for a period of six months and another subjected to 400 cycles of repeated freezing and thawing. Other variables considered in the present research included NSM-CFRP spacing, quantity of flexural reinforcement, and positive and negative moment bending regions. Tests were also performed on 106 bond specimens and are reported in Appendix D. Based on experimental observations and analytical methods, the following conclusions are provided:

- NSM-CFRP transverse reinforcing provided a significant increase in the shear strength of the members when compared to similar girders without NSM-CFRP.

- The primary failure mode for specimens that failed in shear was debonding of the NSM-CFRP and peeling of the concrete cover for the tightly spaced strips.

- Global stiffness of specimens after installation of the NSM-CFRP was not significantly altered. Some specimens showed reduced diagonal deformations indicating that the NSM-CFRP was able to constrain diagonal crack opening.

- Steel stirrup strains near similarly instrumented NSM-CFRP strips exhibited reduced strains at similar levels of applied shear compared to steel stirrup strains before installation of the NSM-CFRP indicating redistribution of load induced stresses.

- Data collected from diagonal displacement sensors and CFRP strain gages showed that members with less flexural reinforcement had higher shear strains when compared to specimens with more flexural reinforcement at similar load levels.

- Specimen IT.5.22.6.S initiated a flexural failure during testing. Half the CFRP strips were removed by saw-cutting to create specimen IT.5.22.12.S which failed in shear. The cumulative effects of saw-cutting, significant prior load history, and cracking on specimen IT.5.22.12.S are not fully known, and thus comparisons should be made with caution. However, higher NSM-CFRP strains and shear panel deflections were measured in specimen IT.5.22.12.S when it had 152 mm (6 in.) CFRP spacing compared to specimen IT.7.22.6.S. The ratio of these strains is similar to the ratio of transverse strain predicted by Response-2000.

- Moisture exposure did not significantly affect shear capacity or stiffness compared to a similar control specimen.

- Freeze-thaw exposure did not significantly affect shear capacity or stiffness compared to a similar control specimen.

- No significant changes were observed in strains or displacements for the specimen subjected to fatigue loading only.

- Fatigue and combined fatigue and freeze-thaw exposure produced no detrimental effects on strength when compared to similar control specimens.

- The specimen subjected to a combined fatigue and freeze-thaw exposure exhibited a slightly reduced stiffness.

- NSM-CFRP strengthening for shear appeared to be more effective for the positive moment regions than negative moment regions due to anchorage past the level of the flexural tension steel.

- ACI 440.2R-08 very conservatively under-predicted the shear contribution of NSM-CFRP materials when compared to experimental results.

- The method for calculating NSM-CFRP shear contribution proposed by Nanni et al. (*2004*) produced higher values than ACI 440.2R-08 but still significantly underestimated the shear contributions when compared to experimental results.

- Effective CFRP stresses were calculated based on Response-2000 curves and experimental shear capacities. The effective NSM-CFRP stresses were much smaller than the tensile strength of the CFRP strips but larger than current design provisions would allow.

- Response-2000 slightly under-predicted the shear capacity of RC members retrofitted with NSM-CFRP when an average effective NSM-CFRP stress of 669 MPa (97 ksi) was used.

- Modeling the CFRP as a supplemental stirrup in Response-2000 provided reasonable estimates of the experimental shear capacities using an empirical average NSM-CFRP effective stress based on the experimental results.

- A design approach is presented for NSM-CFRP application using three design methods (Response-2000, AASHTO-MCFT, and ACI).

9.1 ADDITIONAL RESEARCH

The experiments performed were able to show the efficacy of NSM-CFRP for shear strengthening RC girders. Effects of fatigue and combined freeze-thaw and fatigue loading showed no significant detrimental effects on specimen strength and overall performance. While the strength increase was established for the IT specimens, additional research is required to determine the strength increase from NSM-CFRP retrofitting in T specimens. Because Specimen IT.5.22.12*.S was loaded nearly to flexural failure before removing half of the NSM-

CFRP retrofitting, the observed behavior may not be representative of a specimen not tested in such a manner. An additional specimen with five flexural reinforcing bars should be tested to verify the results of Specimen IT.5.22.12*.S. Finally, additional specimens could be tested to provide additional data for more refined calibration of the analysis and design methods.

10.0 REFERENCES

American Concrete Institute. *ACI 440.2R-08: Guide for the Design and Construction of Externally Bonded FRP Systems for Strengthening Concrete Structures.* ACI Manual of Concrete Practice, Farmington Hills, Michigan, 2008a.

American Concrete Institute. *ACI 318-08: Building Code Requirements for Structural Concrete and Commentary.* ACI Manual of Concrete Practice, Farmington Hills, Michigan, 2008b.

ASTM D 3039/D 3039M-08. *Standard Test Method for Tensile Properties of Polymer Matrix Composite Materials.* ASTM International, West Conshohocken, PA, 2008.

Barros, J.A.O., and S.J.E. Dias. Near Surface Mounted CFRP Laminates for Shear Strengthening of Concrete Beams. *Journal Cement and Concrete Composites*, Vol. 28, No. 3, 2006, pp. 276-292.

Barros, J.A.O., V. Bianco, and G. Monti. NSM CFRP Strips for Shear Strengthening of RC Beams: Tests and Mechanical Model. *The Open Construction and Building Technology Journal*, V. 3, 2009, pp. 12-32.

Bentz, E.C. *Response-2000: Reinforced Concrete Sectional Analysis using Modified Compression Field Theory.* (Version 1.0.5) [Computer software] University of Toronto, 2000.

Bianco, V., J.A.O. Barros, and G. Monti. Bond Model of NSM-FRP Strips in the Context of the Shear Strengthening of RC Beams. *Journal of Structural Engineering*, Vol. 135, No. 6, 2009, pp. 619-631.

Brena, S.F., M.A. Benouaich, M.E. Kreger, and S.L. Wood. Fatigue Tests of Reinforced Concrete Beams Strengthened Using Carbon Fiber-Reinforced Polymer Composites. *ACI Structural Journal*, Vol. 102, No. 2, 2005.

Dawson, M. *Scale Effects on Reinforced Concrete Beams Strengthened for Shear with Discrete Externally Bonded Carbon Fiber-Reinforced Polymer U-Wraps*. Thesis, Oregon State University, 2008.

De Lorenzis, L.A., and A.L.T. Nanni. Shear Strengthening of Reinforced Concrete Beams with near-Surface Mounted Fiber-Reinforced Polymer Rods. *ACI Structural Journal*, Vol. 98, No. 1, 2001.

De Lorenzis, L.A., and A.L.T. Nanni. Bond Between Near-Surface Mounted FRP Rods and Concrete in Structural Strengthening. *ACI Structures Journal*, Vol. 99, No. 2, 2002, pp. 123-133.

Dias, S.J.E., V. Baincco, J.O.A. Barros, and G. Monti. Low strength T-cross section RC beams shear-strengthened by NSM technique. FAELLA, C. [et al.], ed. – Materiali ed approcci innovativi per il progetto in zona sismica e la mitigazione della vulnerabilità delle strutture : atti del Workshop, Fisciano, Itália, 2007. [S.l.]: Polimetrica, ISBN 978-88-7699-065-6, 2007.

Dias, S.J.E., and J.O.A. Barros. Shear Strengthening of T Cross Section Reinforced Concrete Beams by Near-Surface Mounted Technique. *Journal of Composites for Construction*, Vol. 12, No. 3, 2008.

Dias, S.J.E., and J.O.A. Barros. Performance of reinforced concrete T beams strengthened in shear with NSM CFRP laminates. *Engineering Structures*, Vol. 32, 2010, pp. 373-384.

Grace, N.F. Concrete repair with CFRP. *Concrete. International,* Vol. 26, No. 5, 2004, pp. 45–52.

Green, M.F., A.J.S. Dent, and L.A. Bisby. Effect of freeze-thaw cycling on the behaviour of reinforced concrete beams strengthened in flexure with fibre reinforced polymer sheets. *Canadian Journal of Civil Engineering,* Vol. 30, 2003, pp. 1081-1088.

Hassan, T., and S. Rizkalla. Investigation of Bond in Concrete Structures Strengthened with Near Surface Mounted Carbon Fiber Reinforced Polymer Strips. *Journal of Composites for Construction*, Vol. 7, No. 3, 2003, pp. 248-257.

Higgins, C., T.H. Miller, D.V. Rosowsky, S.C. Yim, T. Potisuk, T.K. Daniels, B.S. Nicholas, M.J. Robelo, A. Lee, and R.W. Forrest. *Assessment Methodology for Diagonally Cracked Reinforced Concrete Deck Girder*. Publication SPR 350. Oregon Department of Transportation, 2005.

Higgins, C., A. Lee, T. Potisuk, and T.K. Forrest. High-cycle fatigue of diagonally cracked RC bridge girders: Laboratory tests. *Journal of Bridge Engineering*, Vol. 12, No. 2, 2007, pp. 226-236.

Higgins, C., M.R. Dawson, M.M Mitchell, G. Sopal, and A.E. Senturk. *Environmental Durability of Reinforced Concrete Deck Girders Strengthened for Shear with Surface-Bonded Carbon Fiber-reinforced Polymer*. Publication SPR 652 OTREC-RR-09-09. Oregon Department of Transportation, 2008.

Howell, D. *Shear Repair Methods for Conventionally Reinforced Concrete Girders and Deep Beams*. Dissertation, Oregon State University, 2009.

Islam, AKM. A. Effective Methods of using CFRP Bars in Shear Strengthening of Concrete Girders. *Engineering Structures*, Elsevier, Vol. 31, No. 3, 2009, pp. 709-714.

Karbhari V.M. Response of reinforced polymer confined concrete exposed to freeze and freeze-thaw regimes. *ACI Journal of Composites for Construction,* Vol. 6, No. 1, 2002, pp. 35-40.

Malvar, L.J., N.R. Joshi, J.A. Beran, and T. Novinson. Environmental Effect on the Short-Term Bond of Carbon Fiber-Reinforced Polymer (CFRP) Composites. *Journal of Composites for Construction*, Vol. 7, No. 1, 2003.

Mehta, P.K., and P.J.M. Monteiro. *Concrete Microstructure, Properties, and Materials*, McGraw-Hill, New York, NY, 2006.

Miner, M.A. Cumulative damage in fatigue. *ASME Transportation Journal Applied Mechanics*, Vol. 12, 1945, pp. A159–A164.

Myers, J.J., and M. Ekenel. Effect of Environmental Conditions on Bond Strength between CFRP Laminate and Concrete Substrate. ACI SP-230: 7th International Symposium on Fiber-Reinforced Polymer Reinforcement for Concrete Structures, 2005, pp. 1571-1592.

Nanni, A., M. Di Ludovico, and R. Parretti. Shear Strengthening of a PC Bridge Girder with NSM CFRP Rectangular Bars. *Advances in Structural Engineering*, Vol. 7, No. 4, 2004, pp. 297-309.

Quattlebaum, J.B., K.A. Harries, and M.R. Petrou. Comparison of Three Flexural Retrofit Systems under Monotonic and Fatigue Loads. *Journal of Bridge Engineering*, Vol. 10, No. 6, 2005, pp. 731-740.

Rizzo, A., and L.A. De Lorenzis. Behavior and Capacity of RC beams strengthened in shear with NSM FRP reinforcement. *Construction and Building Materials*, Vol. 23, 2009a, pp. 1555-1567.

Rizzo, A., and L.A. De Lorenzis. Modeling of debonding failure for RC beams strengthened in shear with NSM FRP reinforcement. *Construction and Building Materials*, Vol. 23, 2009b, pp. 1568-1577.

Shahawy, M., and T.E. Beitelman. Static and Fatigue Performance of RC Beams Strengthened with CFRP Laminates. *Journal of Structural Engineering*, Vol. 125, No. 6, 1999, pp. 613-621.

Shield, C., C. French, and E. Milde. The Effect of Adhesive Type on the Bond of NSM Tape to Concrete. ACI SP230: 7th International Symposium on Fiber-Reinforced Polymer (FRP) Reinforcment for Concrete Structures, American Concrete Institute, 2005, pp 355-372.

Soudki K.A., and M.F. Green M. F. Freeze-thaw response of CFRP wrapped concrete. *Concrete International,* Vol. 19, No. 8, 1997, pp. 64-67.

Williams, G., and C. Higgins, C. Fatigue of Diagonally Cracked RC Girders Repaired with CFRP. *Journal of Bridge Engineering*, Vol. 3, No. 1, 2008, pp. 24-33.